VELOCITY OF DECAMETER ELECTROJET IRREGULARITIES UNDER STRONGLY DRIVEN CONDITIONS

A Thesis Submitted to the College of
Graduate Studies and Research
In Partial Fulfillment of the Requirements
For the Degree of Master of Science
In the Department of Physics and Engineering Physics
University of Saskatchewan
Saskatoon

By
James D. Gorin

PERMISSION TO USE

In presenting this thesis in partial fulfillment of the requirements for a Postgraduate degree from the University of Saskatchewan, I agree that the Libraries of this University may make it freely available for inspection. I further agree that permission for copying of this thesis in any manner, in whole or in part, for scholarly purposes may be granted by the professor or professors who supervised my thesis work or, in their absence, by the Head of the Department or the Dean of the College in which my thesis work was done. It is understood that any copying or publication or use of this thesis or parts thereof for financial gain shall not be allowed without my written permission. It is also understood that due recognition shall be given to me and to the University of Saskatchewan in any scholarly use which may be made of any material in my thesis.

Requests for permission to copy or to make other use of material in this thesis in whole or part should be addressed to:

Head of the Department of Physics and Engineering Physics
116 Science Place
University of Saskatchewan
Saskatoon, Saskatchewan
Canada S7N 5E2

ABSTRACT

The Earth ionosphere is a highly inhomogeneous medium containing electron density irregularities of various scales, from hundreds of kilometers to tens of centimeters. Understanding the mechanisms responsible for their formation is an important task for various practical applications such as communication, navigation, and safe satellite operation. Of special interest are the decameter irregularities that are abundant at E-region heights of ~ 100 – 120 km. These are excited when enhanced electric field and plasma drifts are setup in the ionosphere. This thesis is aimed at studying the physics of decameter irregularity formation at E-region heights with a focus on the extreme conditions of very strong electric fields (plasma flows) of > 50 mV/m (1000 m/s) for which the so called Farley-Buneman (FB) plasma instability is the dominating mechanism of irregularity excitation. The relationship between the irregularity velocity and plasma drift is investigated by considering data of the SuperDARN radar located at Stokkseyri, Iclenad. The radar detects echoes from the irregularities and is thus capable of measuring their velocity. The DMSP satellites measure the plasma drifts in situ at heights of ~ 800 km, but these measurements can be projected onto E-region heights at high latitudes. By comparing the radar and satellite data in one direction, we show that irregularity velocity is smaller than the plasma drift by a factor of 2 – 3 with the stronger difference at faster flows. This contrasts with the theoretical expectation for the velocity to be close to 400 m/s, the nominal ion-acoustic speed at electrojet heights. A two-dimensional comparison is performed by considering a subset of the observations for which the HF echo velocity showed a cosine type variation with the radar look direction. This class of echoes is consistent with predictions of recent theories of the Farley-Buneman instability, but the irregularity velocity magnitude was found to be smaller than the ion-acoustic speed with occasional occurrence of velocities as small as 100 m/s. This implies that either recent theories of the Farley-Buneman instability should be modified or that the typical height of HF echoes is typically below 100 km. Various other properties of decameter irregularities are investigated and discussed in view of the existing theories.

ACKNOWLEDGEMENTS

I would like to take this opportunity to thank all those people who made this thesis possible. First and foremost, I thank Dr. A. V. Koustov, my supervisor, for the direction and guidance I have received.

Many thanks go out to all members of the Institute of Space and Atmospheric Studies and the Department of Physics and Engineering Physics for providing the facility, the computer tools, an ideal working environment and all other necessary services, without which, my research would not have been possible. Financial support, for which I greatly appreciate, was provided from the NSERC Team Discovery Grant to Drs. A. V. Koustov and G. J. Sofko, from ISAS scholarships, most notably, the Dr. Theodore R. Hartz Graduate Scholarship in Physics and from my Graduate Teaching Fellowship.

My experience would not have been nearly as enjoyable without the support and friendship of my fellow graduate students, Robyn Drayton-Fiori, Megan Gillies, Robert Gillies, Jeff Pfeifer and Robert Schwab. Finally, I extend my gratitude to my family for their constant support and encouragement.

TABLE OF CONTENTS

LIST OF TABLES

LIST OF FIGURES

LIST OF ABBREVIATION

AACGM	Altitude Adjusted Corrected Geomagnetic Model
ACF	Autocorrelation Function
CSA	Canadian Space Agency
DMSP	Defense Meteorological Satellite Program
EISCAT	European Incoherent Scatter
ePOP	enhanced Polar Outflow Probe
ESA	European Space Agency
FAC	Field-Aligned Currents
FB	Farley-Buneman
FFT	Fast Fourier Transform
FoV	Field-of-View
GD	Gradient-Drift
HF	High Frequency (3 – 30 MHz)
HAIR	High-Aspect Angle Irregularity Region
IDM	Ion Drift Meter
IMF	Interplanetary Magnetic Field
l-o-s	line-of-sight
MLT	Magnetic Local Time
RPA	Retarding Potential Analyzer
SHERPA	Systeme HF d'Etude Radar Polaires et Aurorales
SSIES	Special Sensor for Ions, Electrons, and Scintillations
STARE	Scandinavian Twin Auroral Radar Experiment
SuperDARN	Super Dual Auroral Radar Network
UHF	Ultra High Frequency (0.3 – 3 GHz)
VHF	Very High Frequency (30 – 300 MHz)

CHAPTER 1

INTRODUCTION

The Sun provides the Earth with the heat and light that renders the Earth habitable. Invisible to that life, however, are the particles produced by the Sun and flowing into the surrounding space. Through the interaction with the Earth and its magnetic field, this stream of particles shapes the solar-terrestrial environment and ultimately produces the wondrous displays of aurora, which graces the night sky.

The solar-terrestrial environment is a very complex region of electrodynamical interaction primarily between charged particles, but interactions between charged particles and the neutral upper atmosphere is important. One effect of these interactions is the ionization of neutral particles by incoming energetic particles. This effect, in addition to ionization by solar radiation, leads to the formation of the highly conductive layer called the ionosphere. Various processes in the magnetosphere are related to those in the ionosphere, making it convenient to study the near-Earth environment by looking at the processes in the ionosphere. One such aspect of magnetospheric processes being replicated in the ionosphere is the constant motion of the ionospheric plasma driven by the electric fields established in the magnetosphere. The study of plasma motions in the ionosphere is therefore important for an understanding of the entire solar-terrestrial environment.

1.1 Solar-terrestrial environment

Starting with the general description of the solar-terrestrial environment following largely the books by *Kelley* (1989), *Rees* (1989), *Hargreaves* (1992), *Kivelson and Russell* (1995), *Baumjohann and Treumann* (1997) and *Schunk and Nagy* (2000).

The solar wind is an important factor governing the electrodynamics of the near-Earth environment. The outer most layer of the Sun, the solar corona, is not in hydrostatic equilibrium with the nearby interstellar space; it expands continuously, resulting in the ongoing ejection of particles that become the solar wind. The solar wind plasma is predominantly comprised of electrons and protons with some minor ions, such as doubly ionized helium. Near the Earth's orbit (1 AU ~ 150×10^6 km), the solar wind has a density of a few particles per cubic centimeter and a speed typically ranging from 200 to 800 km/s. The solar wind Alfvén speed is ~ 50 km/s, and therefore the solar wind is supersonic. The solar wind is highly conductive and carries an imbedded magnetic field known as Interplanetary Magnetic Field (IMF), which has typical magnitudes of 1 – 10 nT.

The Earth has its own magnetic field, and a magnetic cavity called the magnetosphere is formed in the near-Earth environment due to its interaction with the solar wind. The pressure exerted on the magnetosphere by the solar wind distorts the dipole magnetic field near the Earth by compressing it on the sunward side and elongating it on the anti-sunward side. The boundary between the regions, where the IMF and the Earth's magnetic field pressures are balanced is the magnetopause and the resulting elongated tear shape of the magnetosphere is at ~ 8 Earth radii (R_E = 6378 km) on the front side of the magnetosphere, extends to 50 – 150 R_E in the tail and is ~ 30 R_E across. The magnetopause converges towards two points known as the polar cusps, and these are the only points where the magnetopause connects directly to the Earth and allows solar wind particles direct access to the innermost regions of the magnetosphere and ionosphere.

On the sunward side of the magnetosphere, the solar wind encounters the Earth's magnetosphere and decelerates to subsonic speeds creating a bow shock, which is located ~ 2 – 3 R_E sunward of the magnetopause. The region between the magnetopause and the bow shock, filled with a turbulent, subsonic solar plasma, is known as the magnetosheath. When the subsonic solar wind reaches the magnetopause with a southward-directed IMF, as depicted in Figure 1.1, the IMF merges with the terrestrial field lines and these field lines merge with those of the solar wind. As the solar wind continues past the magnetosphere these open field lines are dragged along, forming the magnetotail. In the

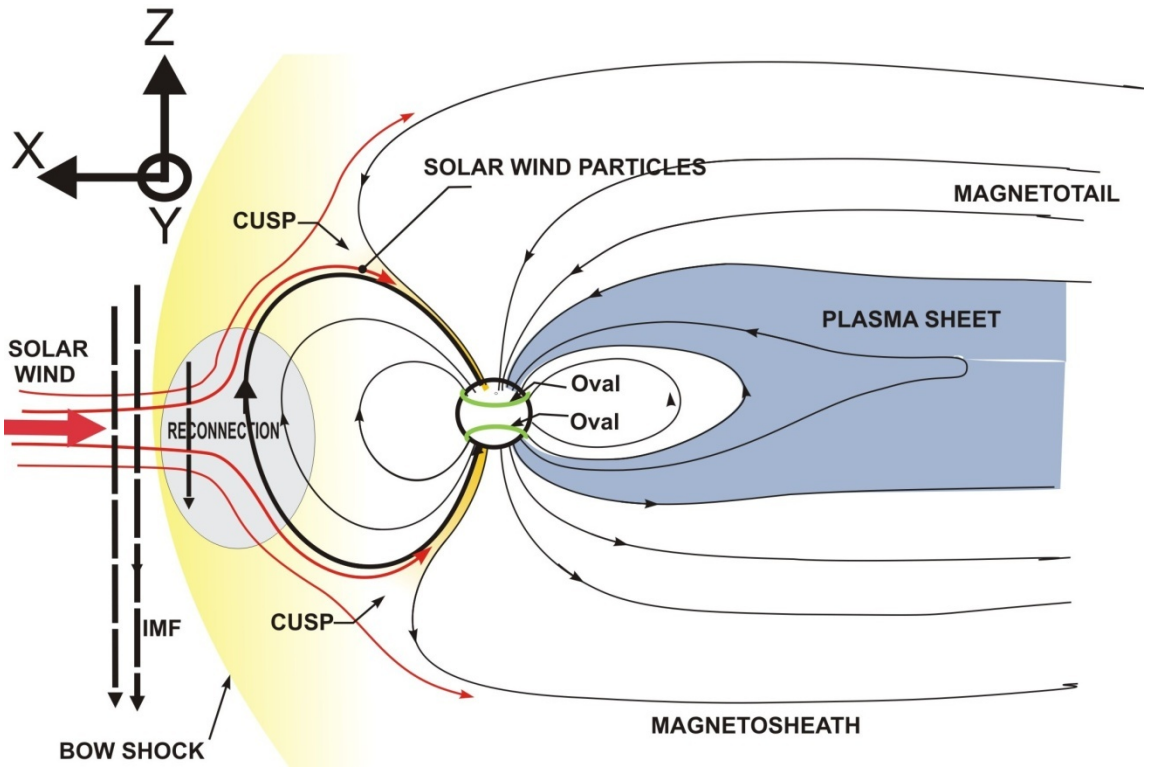

Figure 1.1: Cross section diagram of the Earth's magnetosphere in the North-South plane.

magnetotail, the open field lines reconnect to form closed field lines in the central plasma sheet, which then returns flux tubes Earthward to replace magnetic flux tubes removed from the front side of the magnetosphere.

The central plasma sheet is about 10 R_E thick and is centered in the equatorial plane of the magnetotail separating the oppositely directed magnetic fields of the north and south magnetotail lobes. The particle concentrations increase in the magnetotail lobes towards the central plasma sheet from less than 0.1 cm^{-3} in the lobes to 0.1 – 1 cm^{-3} in the central plasma sheet. The particle energies in the lobes are very low compared to other magnetospheric particles, with few particles above ~ 100 eV. Energies increase rapidly into the plasma sheet from ~ 100 eV on the plasma sheet boundary layer to 5 – 10 keV within the plasma sheet.

Inside ~ 5 R_E is a torus shaped region of plasma, co-rotating with the Earth, known as the plasmasphere. The plasmasphere density ranges from 100 to 1000 cm^{-3} and is comprised of cold electrons and ions of less than ~ 0.1 eV. The plasmasphere terminates with a sharp outer boundary in the magnetosphere where the plasma density

drops to plasma-sheet like values; this is known as the plasmapause. The plasma outside the plasmapause is cold, like the plasmasphere, with densities comparable to that of the plasma sheet; this region is known as the plasma trough. Closer to Earth, the plasmasphere gradually becomes the ionosphere with the increasing concentration of neutral particles.

1.2 Ionosphere

Between the neutral lower atmosphere and the inner magnetosphere lies a transition layer known as the ionosphere. The ionosphere is a quasi-neutral, weakly ionized region stretching from ~ 60 to ~ 1000 km. The ionospheric plasma is in constant motion due to electric fields and neutral winds. Once again, the books by *Kelley* (1989), *Rees* (1989), *Hargreaves* (1992), *Kivelson and Russell* (1995), *Baumjohann and Treumann* (1997) and *Schunk and Nagy* (2000) are used for the discussion in this section.

1.2.1 Regions of the ionosphere and mechanisms of their formation

The ionosphere is conventionally divided into three regions, the D, E and F regions, based on the vertical electron density profile and the nature of the particle motion. Figure 1.2 shows typical electron density profile for the day and night at solar maximum and solar minimum conditions.

The E region forms the middle part of the ionosphere and extends from ~ 90 to 120 km with an electron density peak at an height of ~ 110 km, with values of ~ 10^5 cm^{-3}. At these heights, the most abundant neutral particles are O, O_2 and N_2, with N_2 being the most abundant. The ionized component is formed primarily due to photoionization by solar EUV radiation in the 100 – 150 nm range and X-rays in the 1 – 10 nm range and ionization by precipitating energetic particles from the magnetosphere. All three neutral particles are photoionized with a reaction such as $X + h\nu \rightarrow X^+ + e^-$, where X represents the neutral species. Despite N_2 being the most abundant neutral particle, there is no build up of N_2^+ due to an important series of interchange reactions that occurs between ionized and neutral N_2 and O. The two most frequent reactions are $N_2^+ + O \rightarrow NO^+ + N$ and

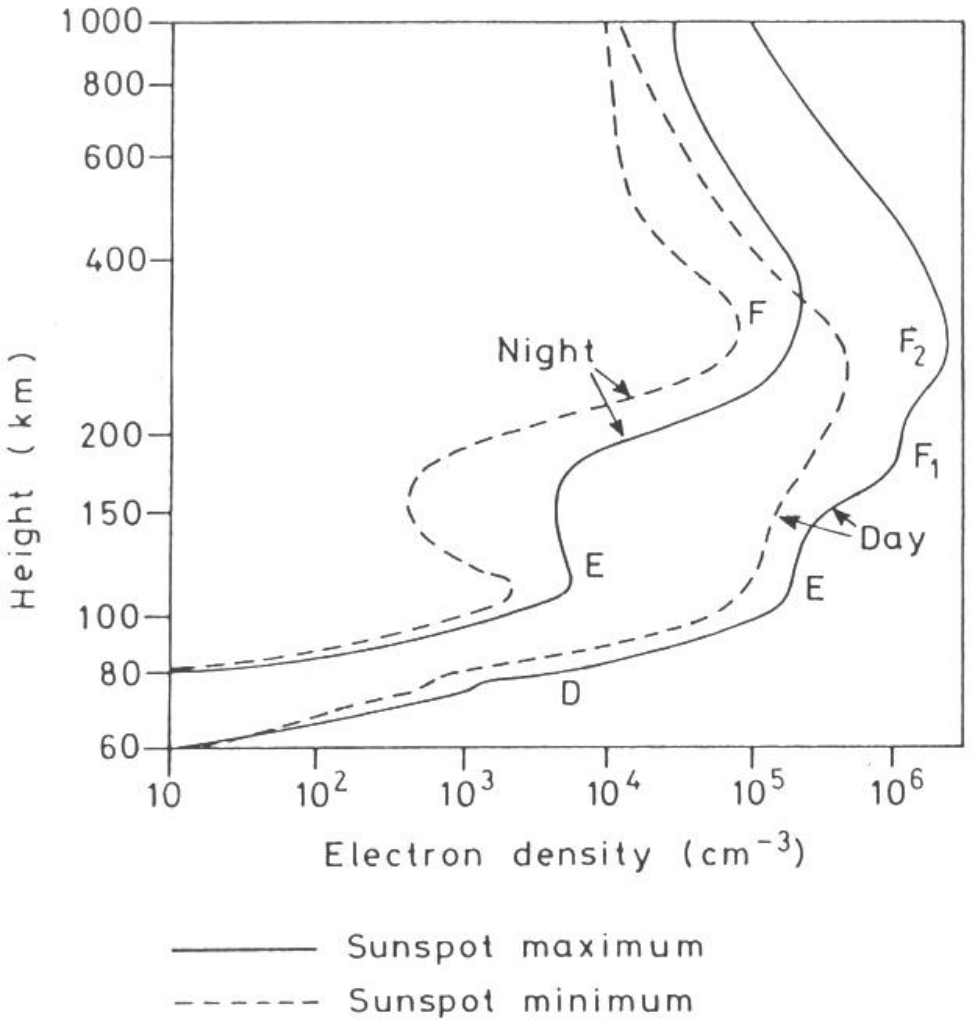

Figure 1.2: Electron density profiles of the Earth's ionosphere for height above the Earth's surface. Profiles for day and night at solar minimum (dashed line) and maximum (solid line) conditions are shown (from *Hargreaves*, 1992).

$O^+ + N_2 \rightarrow NO^+ + N$, this leads to an accumulation of NO^+ instead of N_2^+. Negligible interchange reaction occurs with O_2^+, and this leads to a buildup of O_2^+. Therefore, the most abundant ions in the E region are NO^+ and O_2^+, as shown in Figure 1.3. Low densities of metallic ions such as Fe^+, Mg^+, Ca^+ and Si^+ are also present in the E region due to meteors. In the absence of photoionization at night, recombination results in significant weakening of the E region. In the high-latitude ionosphere, this effect is partially alleviated by particle precipitation that produces some ionization at night.

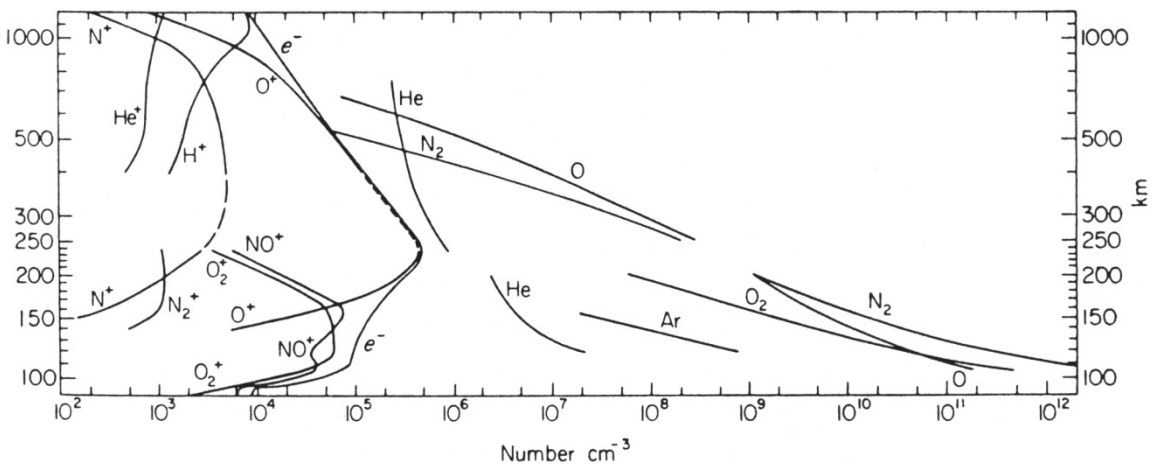

Figure 1.3: Ion, electron and neutral particle density height distributions in the Earth's ionosphere (from *Johnson*, 1969).

The F region forms the uppermost ionospheric region, which extends from ~ 150 to 1000 km, with a peak electron density of ~ 10^6 cm^{-3} for solar maximum and ~ 10^5 cm^{-3} for solar minimum at ~ 300 km. At F-region heights, atomic oxygen is the most abundant neutral particle (Figure 1.3), therefore, photoionization produces an abundance of O^+, and the most abundant ion in the F region is O^+. In the absence of photoionization at night, recombination does result in a depletion of the F-region electron density, but not as pronounced as in the E region. With increasing solar activity, the daytime F region develops a double peak structure known as the F1 and F2 layers at ~ 200 km and ~ 300 km, respectively. The F1 layer is produced in much the same way as the E region, with photoionization by X-rays in the 17 – 91 nm band. The F1 layer does not show up during solar minimum because solar X-ray production is strongly reduced at those periods. The F2 layer, which is also the main peak in the F region, is controlled by both photoionization and vertical transport processes.

The lowest ionospheric region, the D region, extends from about 60 to 90 km and has the lowest electron density of ~ 10^4 cm^{-3}. Like the E region, the D region contains NO^+ and O_2^+, but these ions only dominate the uppermost five kilometers of the D region. The D region also contains numerous other positive and negative ions. Additionally, due to the high neutral density, three body chemical processes are also involved and cluster ions including hydrated protons are present. In many cases, the minor species densities

and chemical reaction rates are not well known and this is partly the reason why the D region is considered separately from the E region, despite the lack of a local peak in the electron density.

Charged particle motion in the ionosphere is strongly controlled by the rate of their collisions with neutral particles (collision frequency) and by the Earth's magnetic field. The effect of the magnetic field on charged particle dynamics is characterized by the gyrofrequency, which is constant to a first approximation for both electrons and ions. The charged particle collision frequency decreases with height dramatically because the density of neutral particles decreases with increasing height exponentially. For this reason, plasma motion due to an external electric field and neutral wind is different at various heights. In the D region below ~ 75 km, the ratio of the collision frequency to the gyrofrequency is more than one for both species, implying that the motions are controlled by collisions of charged particles with neutral particles. In the E and upper D regions, between ~ 95 and 120 km, while the ions are still collision-dominated, the electron collision frequency is smaller than the gyrofrequency and the electrons become magnetized. Above the E region, both the ion and electron collision frequencies are smaller than their respective gyrofrequencies, thus both ions and electrons are magnetized. Quantitative description of the plasma motion in the ionosphere is given later in this chapter.

1.2.2 Electric fields in the ionosphere

As the IMF interacts with the Earth's magnetic field, strong electric fields are excited in the high-latitude ionosphere. In the polar cap, the Earth's magnetic field lines have one end connected to the IMF, i.e., they are open. When the solar wind plasma passes the Earth with an anti-sunward velocity of $\mathbf{V}_{sw}$, this results in a solar wind electric field of $\mathbf{E}_{sw} = -\mathbf{V}_{sw} \times \mathbf{B}_{sw}$. For the southward IMF $\mathbf{B}_{sw}$, the electric field is directed from the dawn to the dusk side on the boundary of the magnetosphere. This solar wind electric field maps down magnetic field lines to ionospheric heights, where it drives anti-sunward plasma flow over the polar cap with a speed of $\mathbf{V}_{pc} = \mathbf{E}_{pc} \times \mathbf{B}/B^2$, where $\mathbf{B}$ and $\mathbf{E}_{pc}$ are the magnetic and electric fields at ionospheric heights, as shown in Figure 1.4.

As the magnetic field lines propagate anti-sunward, they reconnect with terrestrial field lines forming closed field lines in the magnetotail. These newly reconnected field lines are under tension and they drive the plasma back towards the Earth, and a dawn to dusk electric field is setup in the magnetotail. The electric field that maps down near auroral latitudes then has an electric field directed opposite to that in the polar cap, as shown by vectors $\mathbf{E}_a$ in Figure 1.4. The electric field $\mathbf{E}_a$ drives the plasma sunward due to **E** x **B** drift.

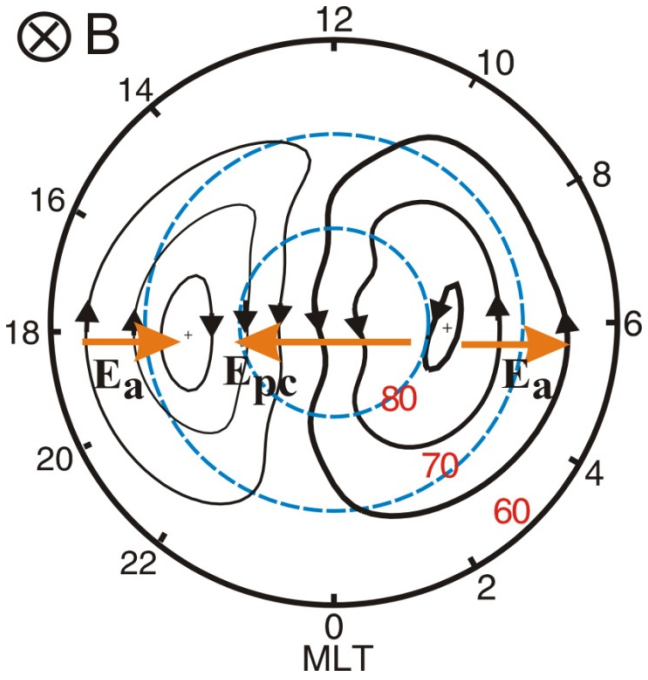

Figure 1.4: Typical orientation of the high-latitude electric field. Latitudes of 70º and 80º are shown by the dashed blue line and stream-lines evening (morning) are shown by the light (heavy) lines.

1.2.3 Neutral winds in the ionosphere

The atmosphere at ionospheric heights is composed of various neutral particles (see Figure 1.3) with densities increasing from 10^9 to 10^{12} cm^{-3}, for F region down to E-region heights, respectively. This means that the neutral density is several orders of magnitude greater than the electron densities for corresponding heights.

The neutral atmosphere is not stationary. Pressure gradients created by solar heating on the dayside result in mostly anti-sunward horizontal winds. Coriolis force due to the rotation of the Earth deflects the flow. Figure 1.5 shows typical neutral wind velocities for quiet conditions at E-region heights of 104 km, 107 km and 110 km, as inferred from observations with the European Incoherent Scatter (EISCAT) radar, located in Tromsø, Norway (*Nozawa and Brekke*, 1999). The neutral winds are anti-sunward in the noon sector and equatorward in the evening sector with typical neutral wind speeds of ~ 100 m/s. In addition, neutral winds are eastward or poleward in the midnight and morning sectors with typical neutral wind speeds of ~ 50 m/s. For active conditions, neutral wind velocities can increase to ~ 200 m/s or greater and *St.-Maurice et al.* (1999) reported neutral wind speeds on the order of 350 m/s at 115 km height.

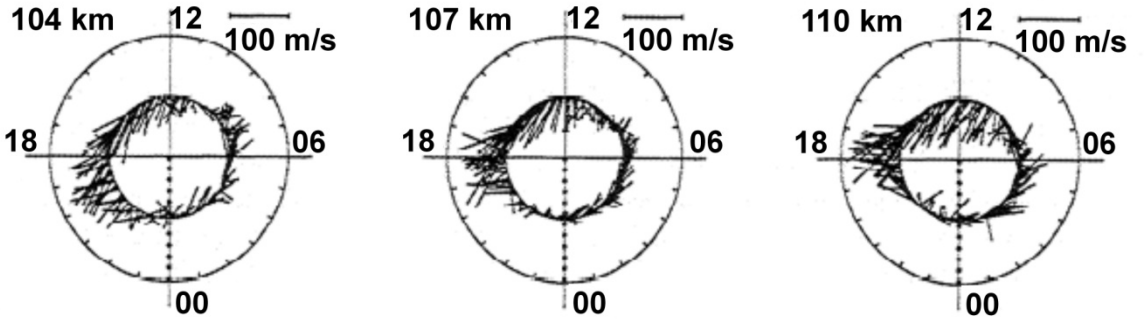

Figure 1.5: Typical horizontal neutral wind velocities for heights of 104, 107 and 110 km (adapted from *Nozawa and Brekke*, 1999).

1.3 Plasma motions in the high-latitude ionosphere

Combined with the magnetic field, the electric field and neutral wind are two major sources of plasma motion in the ionosphere. To illustrate quantitatively their contribution to the velocity of electrons and ions at various heights and their relative importance, we consider a configuration with a vertical magnetic field, oriented in the negative z direction, and an electric field and neutral wind directed in the x and y directions, as shown in Figure 1.6.

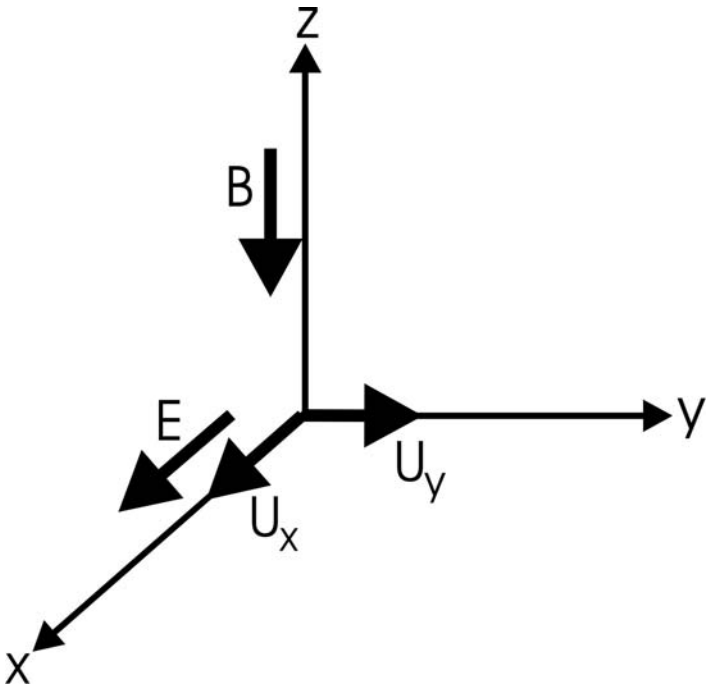

Figure 1.6: Coordinate system and configuration of magnetic field and electric field and neutral wind directions adopted for the analysis.

The fluid equation of motion in the ionosphere is (*Kelley*, 1989):

$$m_\alpha \frac{d\mathbf{v}_\alpha}{dt} = q_\alpha\left[\mathbf{E} + \mathbf{v}_\alpha \times \mathbf{B}\right] - m_\alpha \nu_{\alpha n}\left(\mathbf{v}_\alpha - \mathbf{U}_n\right) \pm m_\alpha \nu_{ei}\left(\mathbf{v}_e - \mathbf{v}_i\right) - \frac{\nabla\left(n_\alpha T_\alpha\right)}{n_\alpha} + m_\alpha \mathbf{g}. \quad (1.1)$$

Here α represents the species, ions or electrons, m_α is the mass, $\mathbf{v}_\alpha$ is the velocity, q_α is the charge, $\nu_{\alpha n}$ is the species collision frequency with neutrals, $\mathbf{U}_n$ is the neutral wind velocity, ν_{ei} is the electron-ion collision frequency, n_α is the species number density, T_α is the temperature in units of energy (eV) and $\mathbf{g}$ is the gravitational acceleration. The third term on the right hand side describes Coulomb collisions (friction) between electrons and ions; it is positive for ions and negative for electrons. It is important to note that this term is negligible compared to the second term for the E-region plasma because $\nu_{\alpha n} >> \nu_{ei}$. To simplify the analysis, we will also assume that T = 0, the cold plasma approximation, and we will neglect gravity. Equation (1.1) then reduces to:

$$m_\alpha \frac{d\mathbf{v}_\alpha}{dt} = q_\alpha\left[\mathbf{E} + \mathbf{v}_\alpha \times \mathbf{B}\right] - m_\alpha \nu_{\alpha n}\left(\mathbf{v}_\alpha - \mathbf{U}_n\right). \quad (1.2)$$

Solving for the velocity at steady state conditions ($d\mathbf{v}/dt = 0$) results in general expressions for the electron and ion velocities in the *x* direction:

$$v_{\alpha x} = \frac{\nu_{\alpha n}\Omega_\alpha}{\Omega_\alpha^2+\nu_{\alpha n}^2}\frac{E}{B} - \frac{\Omega_\alpha \nu_{\alpha n}}{\Omega_\alpha^2+\nu_{\alpha n}^2}U_y + \frac{\nu_{\alpha n}^2}{\Omega_\alpha^2+\nu_{\alpha n}^2}U_x, \tag{1.3}$$

and in the *y* direction:

$$v_{\alpha y} = \frac{\Omega_\alpha^2}{\Omega_\alpha^2+\nu_{\alpha n}^2}\frac{E}{B} + \frac{\nu_{\alpha n}^2}{\Omega_\alpha^2+\nu_{\alpha n}^2}U_y + \frac{\nu_{\alpha n}\Omega_\alpha}{\Omega_\alpha^2+\nu_{\alpha n}^2}U_x, \tag{1.4}$$

where Ω_α is the particle gyrofrequency given by $\Omega_\alpha = \frac{q_\alpha B}{m_\alpha}$ and $\frac{E}{B}$ is the collisionless plasma speed in crossed electric and magnetic fields, which is derived from Equation (1.2), assuming no collisions.

As is evident from Equations (1.3) and (1.4), the drift of ions and electrons is dependent on their respective collision frequencies with neutral particles and their gyrofrequencies. According to the work of *Schunk and Nagy* (2000), the ion-neutral collision frequency depends only on the neutral species number density (n_n) by:

$$\nu_{in} = C_{in} n_n, \tag{1.5}$$

where C_{in} is the coefficient for the interaction between the dominant neutral particles (N_2, 0_2 and O) and NO^+ at E-region heights (C_{in} is 4.34×10^{-10} for N_2, 4.27×10^{-10} for O_2 and 2.44×10^{-10} for O). The electron-neutral collision frequency also depends on the neutral species density, as well as the electron temperature (T_e). The electron-neutral collision frequencies for N_2, O_2 and O are then respectively (*Schunk and Nagy*, 2000):

$$\nu_{en}(N_2) = 2.33\times10^{-10}\, n_n(N_2)\left(1 - 1.21\times10^{-4}\, T_e\right)T_e, \tag{1.6}$$

$$\nu_{en}(O_2) = 1.82\times10^{-10}\, n_n(O_2)\left(1 + 3.6\times10^{-2}\, T_e^{1/2}\right)T_e^{1/2}, \tag{1.7}$$

$$\nu_{en}(O) = 8.9\times10^{-11}\, n_n(O)\left(1 + 5.7\times10^{-4}\, T_e\right)T_e^{1/2}. \tag{1.8}$$

Using Equations $(1.5)-(1.8)$ in combination with neutral density and electron temperature profiles obtained from the MSIS-E-90 model for the 2002 March equinox (19:16 UT, 20 March 2002) at 63.86º N and 22.02º W, allows for the collision frequency profiles shown in Figure 1.7 to be calculated. The gyrofrequencies shown in Figure 1.7 are $\Omega_i = 160\ s^{-1}$ (for NO^+ ions) and $\Omega_e = -8.8 \times 10^6\ s^{-1}$, as calculated from $\Omega_\alpha = \frac{q_\alpha B}{m_\alpha}$.

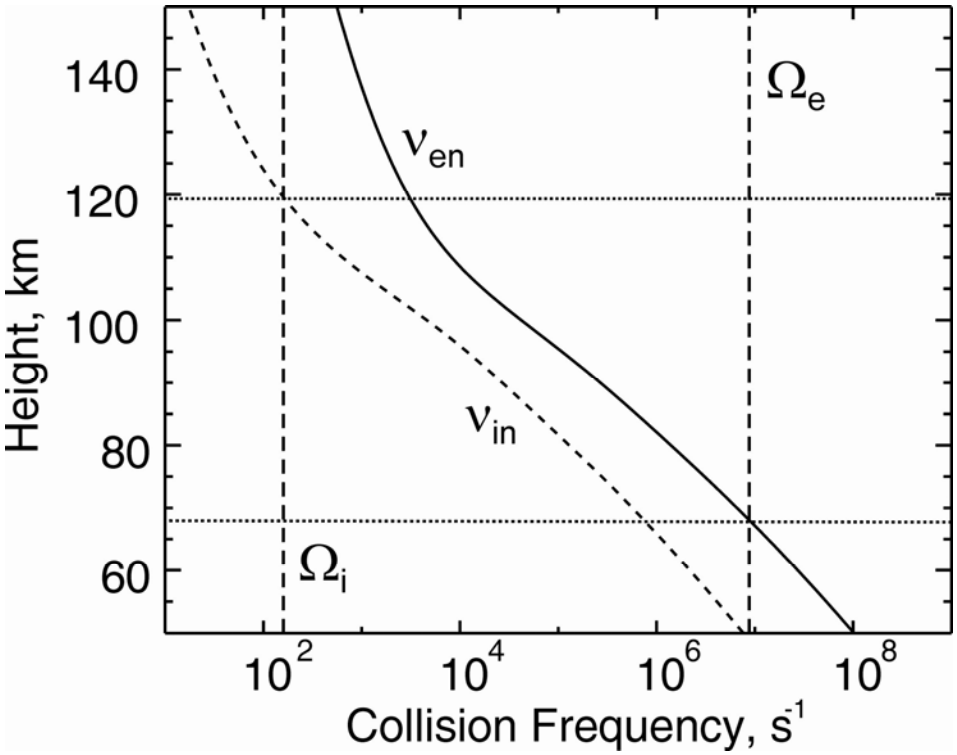

Figure 1.7: Height profiles of collision frequencies of the ions and electrons with neutral particles (ν_{in}, ν_{en}) in the bottom part of the Earth's ionosphere. The vertical dashed lines indicate the gyrofrequencies of the ions and electrons (Ω_i, Ω_e).

1.3.1 Plasma motion due to electric fields

Since the collision frequencies vary strongly with height, an investigation of how the electron and ion velocities of Equations (1.3) and (1.4) vary with height is undertaken for the height regions defined by the collision frequencies shown in Figure 1.7. The height where the gyrofrequency is equal to their respective collision frequencies are chosen as the boundaries between the considered regions due to the importance of the collision frequency to gyrofrequency ratio in the motion of plasma. The region above 120 km is the region where both Ω_i and Ω_e are greater than their respective collision frequencies, the region below 68 km is where both Ω_i and Ω_e are less than their respective collision frequencies and the intermediate region is where Ω_i is greater than and Ω_e is less than their respective collision frequencies.

To have an idea of the electron and ion velocities at these heights due to an electric field, we will first consider three height regions: above 135 km, where $\nu_{en} << \Omega_e$,

and $\nu_{in} << \Omega_I$; between 75 and 115 km, where $\nu_{en} << \Omega_e$, and $\nu_{in} >> \Omega_I$; and below 60 km where $\nu_{in} >> \Omega_i$ and $\nu_{en} > \Omega_e$. Above 135 km, Equations (1.3) and (1.4) become:

$$v_{ex} = \frac{\nu_{en}}{|\Omega_e|}\frac{E}{B} \approx 0, \quad v_{ey} = \frac{E}{B} \quad \text{and} \quad v_{ix} = \frac{\nu_{in}}{\Omega_i}\frac{E}{B}, \quad v_{iy} = \frac{E}{B}. \tag{1.9}$$

The electrons and ions are both **E** x **B** drifting at the collisionless speed $\frac{E}{B}$, and the ions also have a small collisional drift component in the electric field direction.

Between 75 and 115 km, Equations (1.3) and (1.4) become:

$$v_{ex} = \frac{\nu_{en}}{|\Omega_e|}\frac{E}{B} \approx 0, \quad v_{ey} = \frac{E}{B} \quad \text{and} \quad v_{ix} = \frac{\Omega_i}{\nu_{in}}\frac{E}{B}, \quad v_{iy} = \frac{\Omega_i^2}{\nu_{in}^2}\frac{E}{B}. \tag{1.10}$$

The electrons are **E** x **B** drifting at the collisionless plasma speed $\frac{E}{B}$, while the ions experience minimal **E** x **B** drift and drift slowly in the electric field direction.

Finally, below 60 km, Equations (1.3) and (1.4) become:

$$v_{ex} = \frac{|\Omega_e|}{\nu_{en}}\frac{E}{B}, \; v_{ey} = \frac{\Omega_e^2}{\nu_{en}^2}\frac{E}{B} \approx 0 \quad \text{and} \quad v_{ix} = \frac{\Omega_i}{\nu_{in}}\frac{E}{B} \approx 0, \; v_{iy} = \frac{\Omega_i^2}{\nu_{in}^2}\frac{E}{B} \approx 0. \tag{1.11}$$

The electrons are slowly moving opposite to the electric field direction, and the ions are nearly stationary.

To get a better idea of the velocities than what Equations (1.9) to (1.11) provide (which only consider the leading terms) Equations (1.3) and (1.4) are considered without simplification in some general numerical calculations. We assume that the magnitude of the electric field is 50 mV/m, which corresponds to a speed of $\frac{E}{B}$ = 1000 m/s, with no neutral wind ($U_x = U_y = 0$) and the collision frequencies have the vertical profile as shown in Figure 1.7. Plasma drift magnitudes due only to the electric field term from Equations (1.3) and (1.4) are presented in Figure 1.8, where the electric field component of the velocity is shown in Figure 1.8a, and the **E** x **B** directed component of the velocity is shown in Figure 1.8b. Above 130 km, the electrons drift in the **E** x **B** direction with the speed $\frac{E}{B}$. The ions are also drifting in the **E** x **B** direction with the speed $\frac{E}{B}$, with a drift component in the electric field direction. Between 75 and 110 km, the electrons do not

move much in the electric field direction and undergo mostly **E** x **B** drift while the ions undergo drift primarily in the electric field direction with a small drift in the **E** x **B** direction. Below 65 km, the electrons are drifting in the electric field direction, with a drift component in the **E** x **B** direction, while the ions are stationary. In general, the speed in the **E** x **B** direction begins to increase roughly 10 km below where the collision frequency to gyrofrequency ratio is less than one (~ 120 km for ions and ~ 65 km for electrons) and increases towards $\frac{E}{B}$ within 20 km. The speed in the electric field direction peaks at exactly of $\frac{E}{B}$ where the collision frequency to gyrofrequency ratio is equal to one and decreases to zero within 15 km with an increasing or decreasing collision frequency to gyrofrequency ratio.

1.3.2 Plasma motions due to neutral winds

Now consider the electron and ion velocities at heights above 135 km, between 75 and 115 km and below 60 km due to the neutral wind by including only the neutral wind terms in general Equations (1.3) and (1.4), similar to what was done for the electric field in Section 1.3.1. Above 135 km, $\nu_{en} << |\Omega_e|$, and $\nu_{in} << \Omega_i$, and Equations (1.3) and (1.4) become

$$v_{ex} = \frac{\nu_e^2}{\Omega_e^2} U_x = 0, \quad v_{ey} = \frac{\nu_e}{|\Omega_e|} U_x = 0 \quad \text{and} \quad v_{ix} = \frac{\nu_i^2}{\Omega_i^2} U_x = 0, \quad v_{iy} = \frac{\nu_i}{\Omega_i} U_x \qquad (1.12)$$

for the electrons and ions, respectively. Therefore, above 135 km, it is expected that the electrons are not moving and ions have a small velocity in the **U** x **B** direction.

Between 75 and 115 km, $\nu_{en} << |\Omega_e|$, and $\nu_{in} >> \Omega_i$, and Equations (1.3) and (1.4) become:

$$v_{ex} = \frac{\nu_e^2}{\Omega_e^2} U_x = 0, \quad v_{ey} = \frac{\nu_e}{|\Omega_e|} U_x = 0 \quad \text{and} \quad v_{ix} = U_x, \quad v_{iy} = \frac{\Omega_i}{\nu_i} U_x \qquad (1.13)$$

for the electrons and ions, respectively. This indicates that the electrons are not moving and the ions experience minimal **U** x **B** drift, but mostly drift with the neutral wind.

Below 60 km, $\nu_{en} >> |\Omega_e|$, and $\nu_{in} >> \Omega_i$, and Equation (1.3) becomes:

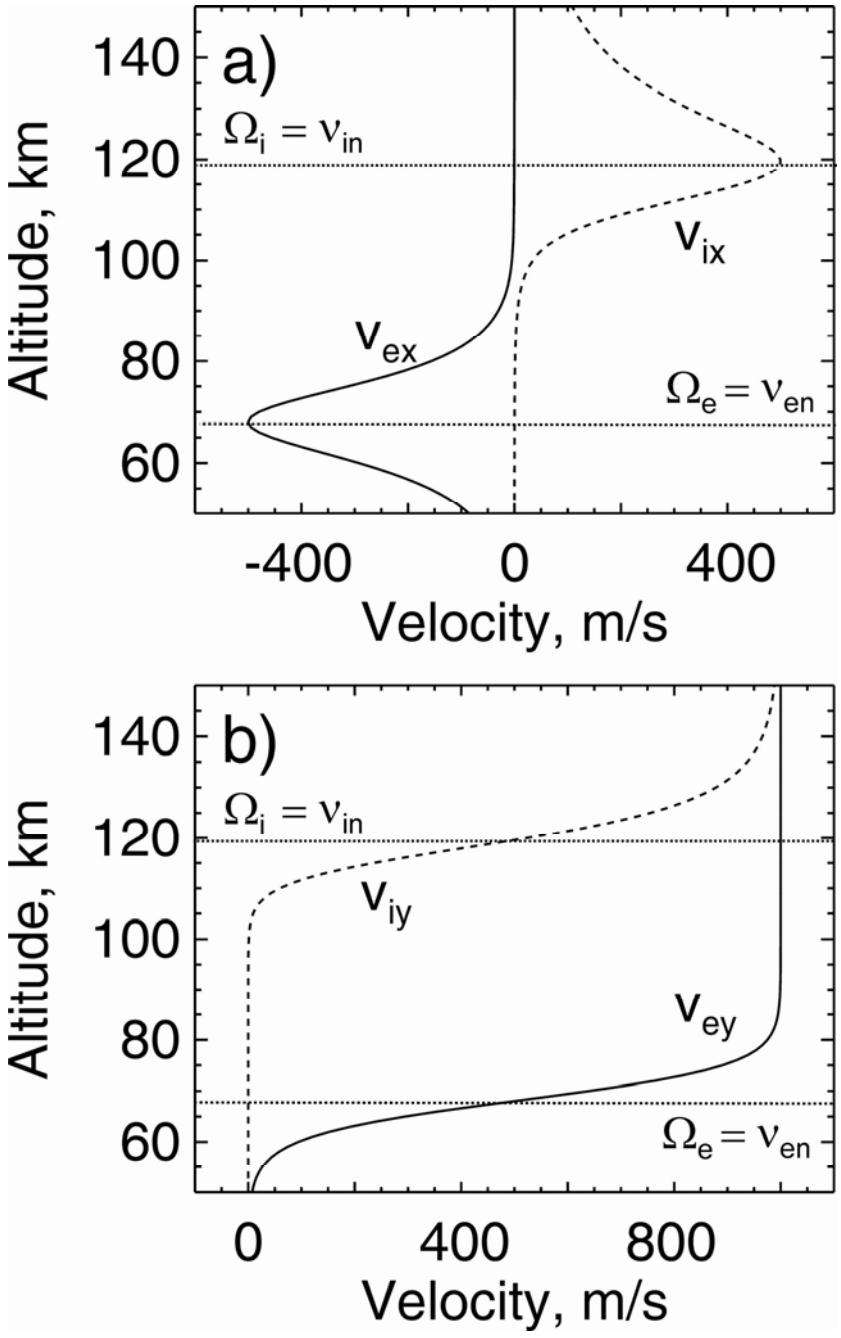

Figure 1.8: Electron (e) and ion (i) velocity at various heights for an electric field driven plasma ($\frac{E}{B}$ = 1000 m/s). (a) Velocity in the electric field direction (*x* direction). (b) Velocity in the **E** x **B** direction (*y* direction) as calculated from Equations (1.3) and (1.4).

$$v_{ex} = U_x, \quad v_{ey} = \frac{|\Omega_e|}{\nu_e} U_x \quad \text{and} \quad v_{ix} = U_x, \quad v_{iy} = \frac{\Omega_i}{\nu_i} U_x = 0. \tag{1.14}$$

Similar to what was done in Section 1.3.1, Equations (1.3) and (1.4) are considered without simplification in some general numerical evaluations. We assume that the neutral wind speed is U_x = 200 m/s and U_y = 0 m/s, with no electric field ($\frac{E}{B} = 0$). For the collision frequencies as shown in Figure 1.7 and the gyrofrequencies from Section 1.3.1, the plasma velocities due only to the neutral wind term from Equations (1.3) and (1.4) are presented in Figure 1.9, where the velocity component along the neutral wind direction is shown in Figure 1.9a and the velocity component along the **U** x **B** direction is shown in Figure 1.9b. Above 130 km, the electrons are stationary with respect to the neutral wind. This is consistent with the estimations from Equation (1.12). The ions are drifting in the **U** x **B** direction with a speed less than the neutral wind speed and they are mostly stationary in the neutral wind direction, as predicted by Equation (1.12). Between 110 and 80 km, the electrons are not moving in the neutral wind direction but do undergo some **U** x **B** drift closer to 75 km, while the ions undergo drift primarily in the neutral wind direction with a small drift in the **U** x **B** direction closer to 110 km, consistent with the predictions from Equation (1.13). Below 65 km, the electrons drift in the neutral wind direction, with another drift component in the **U** x **B** direction, while the ions drift entirely in the neutral wind direction, consistent with Equation (1.14). In general, the speed in the neutral wind direction begins to increase roughly 10 km below where collision frequency and gyrofrequency are equal (~ 120 km for ions and ~ 65 km for electrons) and increases towards U_x within 15 km. The speed in the **U** x **B** direction peaks at exactly of U_x where the collision frequency and gyrofrequency are equal and decays to zero within 15 km of the height where the collision frequency and gyrofrequency are equal.

1.3.3 Summary of plasma motions

According to the calculations performed in Section 1.3, the fastest changes in the behavior of the plasma motion occur where the ratio of the collision frequency and

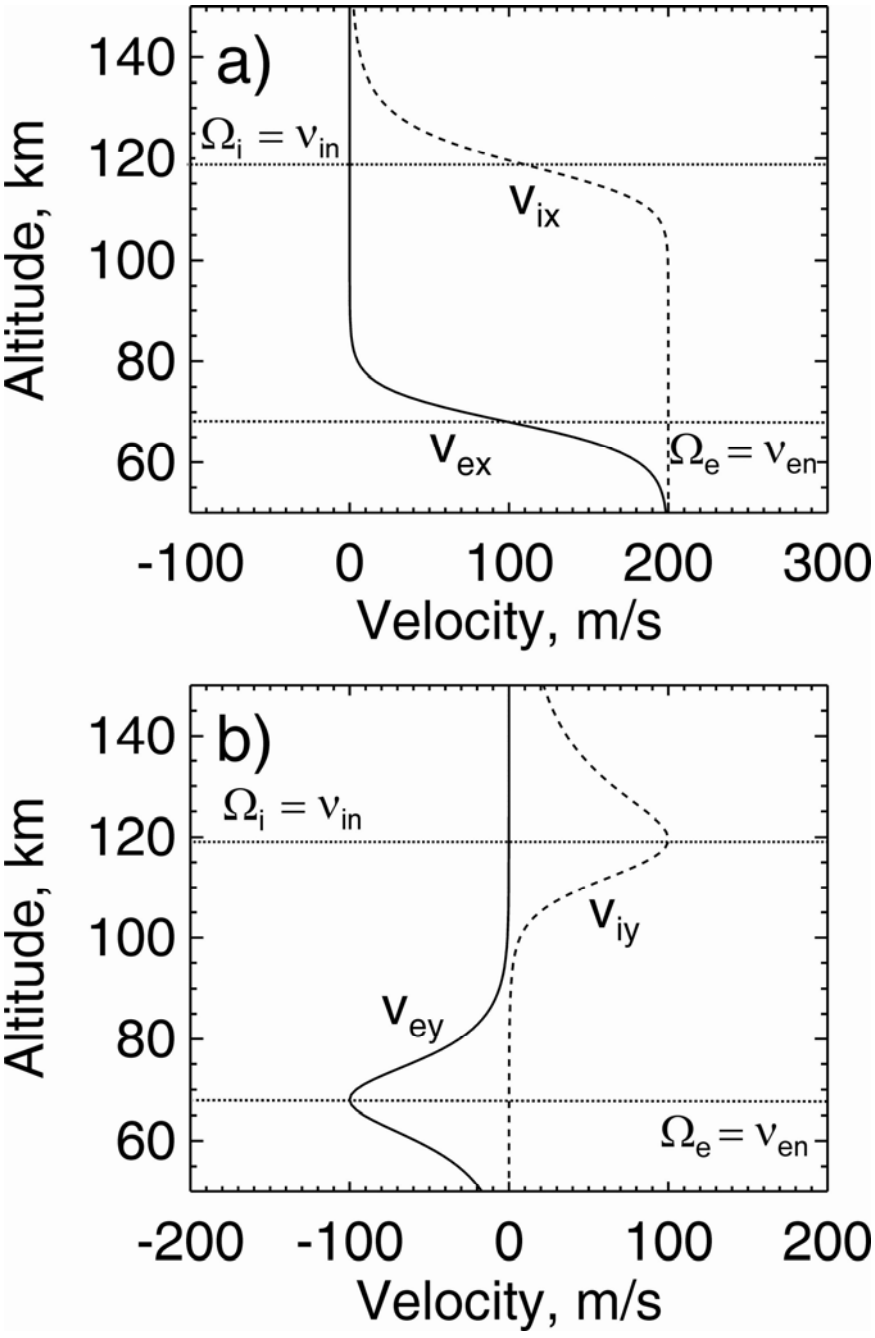

Figure 1.9: Electron (e) and ion (i) velocity at various heights for a neutral wind driven plasma (U_x = 200 m/s). (a) Velocity in the neutral wind direction (*x* direction). (b) Velocity in the **U** x **B** direction (*y* direction) as calculated from Equations (1.3) and (1.4).

gyrofrequency are equal, which occurs at ~ 120 km for ions and ~ 68 km for electrons. With respect to these heights, the motion of the plasma species due to an electric field behaves as follows. The speed in the **E** x **B** direction begins to increase sharply from zero roughly 10 km below the height where the collision frequency to gyrofrequency ratio is equal to one and increases to $\sim \frac{E}{B}$ within ~ 20 km. The speed in the electric field direction peaks at exactly half of $\frac{E}{B}$ at the height where the collision frequency to gyrofrequency ratio is equal to one and decays to zero 15 km away from that height.

Plasma species motion due to the neutral wind behaves as follows. The velocity in the neutral wind direction begins to increase roughly 10 km below the height where the collision frequency to gyrofrequency ratio is equal to one and increases towards U_x within 15 km. The velocity in the **U** x **B** direction peaks at exactly half of U_x at the height where the collision frequency to gyrofrequency ratio is equal to one and decays to zero 15 km away from that height.

1.4 Formation of small-scale ionospheric structures, plasma irregularities

Because of the non-uniformity in the solar luminosity received by the upper atmosphere, and because energetic particles only commonly precipitate at high latitudes, the electron density is strongly inhomogeneous. It is well established that the electron density at a specific height changes on the scale of hundreds of kilometers. Observations showed, however, that the ionospheric plasma often contains inhomogeneities not only of this scale but also of much smaller size, practically all the way down to centimeter scales. These are usually called irregularities, and they are envisioned as electron density plasma waves propagating in the ionosphere.

Among irregularities of various scales, the ones at 0.1-10 m are of special interest in the physics of the Earth's ionosphere. This is not only because they represent the fine structure of the ionosphere, but also because they can scatter radio waves and thus provide valuable information on the physical processes occurring in the plasma. The velocity of the irregularities is related to the ionospheric electric field, which potentially

makes it possible to estimate the ionospheric electric field from Doppler velocity of echoes observed by ground-based radars.

1.4.1 Coherent echo classification at VHF and HF

Coherent radar echo spectra in the E region demonstrate a number of distinctly classifiable types. Traditionally, very high frequency (VHF) radar observations form the basis for classification (*Fejer and Kelley*, 1980; *Haldoupis*, 1989; *Schlegel*, 1996; *Sahr and Fejer*, 1996; *Moorcroft*, 2002). Figure 1.10 shows the types of echoes in terms power and velocity, both in arbitrary units. Type 1 echoes are narrow and powerful and are centered on the ion-acoustic speed at electrojet heights, E-region heights where differentials in the ion and electron velocities results in a current flow (Figure 1.10a); these are typically observed along the **E** x **B** direction. Type 2 echoes (Figure 1.10b) are broad echoes, with power typically lower than Type 1 echoes. Additionally, the velocity of Type 2 echoes tends to change according to a cosine function with respect to the flow angle, the angle between the **E** x **B** electron drift and the radar beam direction. Type 3 and 4 echoes (Figures 1.10c and d) are similar to Type 1 echoes in that they have high power and narrow widths. They differ from Type 1 in that Type 3 echoes have a much lower velocity than the ion-acoustic speed (roughly a half of Cs), whereas Type 4 echoes have a velocity higher than the ion-acoustic speed. Types 1 and 2 echoes form the majority of VHF radar observations, with Types 3 and 4 occurring less often. In addition, a weak Type 3 peak typically accompanies a strong Type 4 peak (*St-Maurice et al.*, 1994).

Observations of high frequency (HF) echoes, however, show the presence of five major classes of echoes (*Milan and Lester*, 2001). These classes are as follows:

1) Narrow echoes with velocities near the ion-acoustic speed, similar to Type 1 echoes at VHF.
2) Broad echoes with velocities below the ion-acoustic speed, similar to Type 2 at VHF.
3) Echoes with velocities greater than the ion-acoustic speed, occurring at low L-shell angles and whose velocity increases with L-shell angle.

4) Echoes with velocities greater than the ion-acoustic speed, occurring at large L-shell angles and whose velocity decreases with an increasing L-shell angle.
5) Broad echoes with a velocity below the ion-acoustic speed directed opposite to the **E** x **B** direction.

The absence of VHF analogues for some of the HF classes suggests that there may be a radar frequency dependence on the observation of these types. Additionally, it is believed that these types may be explained by recent non-linear theories (*Drexler et al*., 2002; *Drexler and St.-Maurice*, 2005; *St.-Maurice and Hamza*, 2008), which will be discussed latter in Chapter 2, and further investigations may contribute to the better understanding of E-region irregularity formation processes.

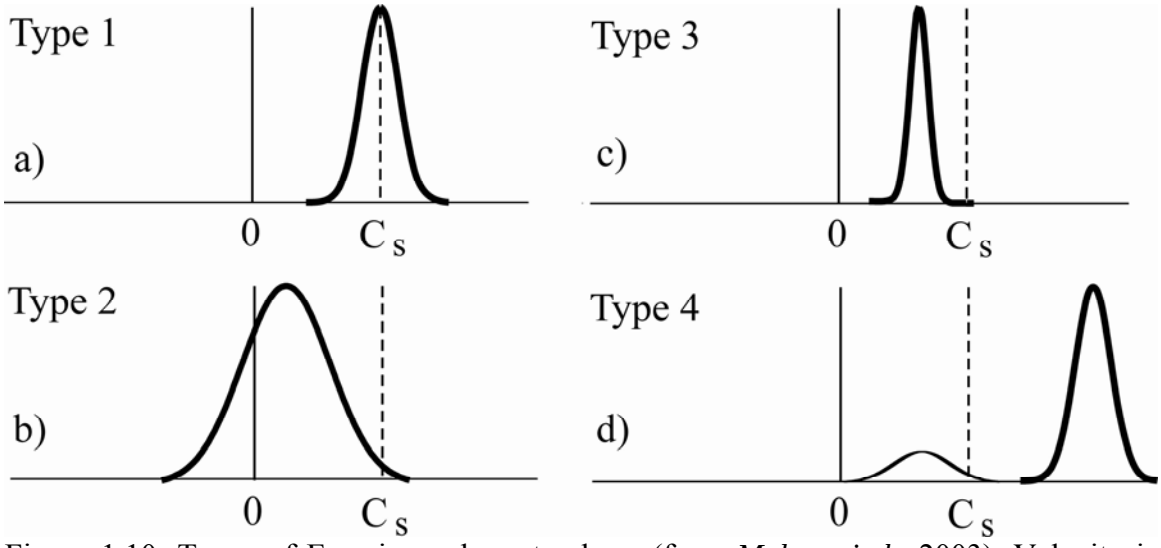

Figure 1.10: Types of E-region coherent echoes (from *Makarevitch,* 2003). Velocity is shown on the x-axis and power is shown on the y-axis.

1.4.2 Formation of electrojet irregularities through the Farley-Buneman instability

To generate ionospheric irregularities, a source of free energy is needed. A relative drift between the various species is one possible source of free energy for plasma irregularity formation. E-region heights are where the largest drifts between electrons and ions exist. This can lead to counter streaming instabilities that can produce small-scale (meter to decameter scale) irregularities, the Farley-Buneman (FB) and Gradient-Drift (GD) plasma instabilities.

The FB plasma instability occurs in homogeneous plasmas when the relative drift between the electrons and ions exceeds the ion-acoustic speed of the medium. This instability is most effective at meter-scale wavelengths, and it is believed that the FB instability is the cause for the onset Type 1 coherent echoes.

To introduce the FB instability, one can consider the case of the high-latitude E region, where the magnetic field is anti-parallel to the vertical *z*-axis, the electric field is along the *x*-axis, and there is arbitrary perturbation propagation in the horizontal *xy*-plane, as shown in Figure 1.11. The equation of motion including the ion inertia and temperature effects included is described by Equation (1.1), and the continuity equation is given by:

$$\frac{\partial n_\alpha}{\partial t} + \nabla \cdot \left(n_\alpha \, \mathbf{v}_\alpha \right) = 0. \tag{1.15}$$

If one introduces small perturbations such that **E,** $\mathbf{v}_\alpha$ and n_α consist of a background component and a perturbed quantity that is for example for density $n_\alpha = n_{0\alpha} + \delta n_\alpha$, with $\delta n_\alpha << n_{0\alpha}$, and assuming that the electric field can be expressed as a gradient in an electrostatic potential ($\delta \mathbf{E} = -\nabla \delta \varphi$), the plasma is quasi-neutral ($\delta n_\alpha = \delta n_i = \delta n_e$) and the perturbed quantities $\delta \mathbf{E}_\alpha$, $\delta \mathbf{v}_\alpha$ and δn_α vary as a sinusoidal wave (e.g., $\delta n_\alpha \propto e^{i(\mathbf{k}\cdot\mathbf{r}-\omega t)}$), Equation (1.14) can be linearized to:

$$-i\omega \delta n_\alpha + i n_{0\alpha} \mathbf{k} \cdot \delta \mathbf{v}_\alpha + i \delta n_\alpha \mathbf{k} \cdot \mathbf{v}_{0\alpha} = 0. \tag{1.16}$$

Neglecting Coulomb collisions ($\nu_{\alpha n} >> \nu_{ie}$) and no neutral wind ($U_n = 0$) being considered, Equation (1.1) can be linearized and presented in the form:

$$-i\omega \delta \mathbf{v}_\alpha = \frac{q_\alpha \delta \mathbf{E}}{m_\alpha} - \Omega_\alpha \left[\delta \mathbf{v}_\alpha \times \mathbf{e}_z \right] - \nu_{\alpha n} \delta \mathbf{v}_\alpha - \frac{i \mathbf{k} \delta T_\alpha}{m_\alpha} - \frac{i \mathbf{k} T_\alpha \delta n_\alpha}{m_\alpha n_{0\alpha}}. \tag{1.17}$$

Neglecting the variations in the temperature in equation (1.16) and considering all three dimensions to solve equations (1.15) and (1.16), the dispersion relation can be written (*Drexler and St.-Maurice*, 2005):

$$\omega\left(\omega + i\nu_i\right) + i\frac{\nu_i}{\psi}\left(\omega - \mathbf{k}\cdot\mathbf{v}_d\right) - k^2 C_s^2 = 0, \tag{1.18}$$

where $\mathbf{v}_d$ is the relative electron-ion drift, $C_s = \sqrt{\frac{(T_e + T_i)}{m_i}}$ is the ion-acoustic speed of the medium and $\psi = \frac{\nu_e \nu_i}{\Omega_e \Omega_i}\left(1 + \frac{\Omega_e^2}{\nu_e^2}\sin^2\alpha_o\right)$ is a parameter that depends on the collision frequencies, gyro-frequencies (Ω_α) and the aspect angle (α_o) between the wave propagation direction and the perpendicular to the magnetic field, and ω is written for the coordinate system moving with the ions.

The roots of the dispersion equation have two important limits, ψ small ($<< 1$) and ψ large. According to *Drexler and St.-Maurice* (2005), for the small ψ values in the dispersion equation results in a wave frequency (ω_r) and growth rate (γ) of:

$$\omega_r = \mathbf{k} \cdot \mathbf{v}_d (1 - \psi) \tag{1.19}$$

and

$$\gamma = \frac{\psi}{\nu_i}\left((\mathbf{k} \cdot \mathbf{v}_d)^2 - k^2 C_s^2\right). \tag{1.20}$$

For small ψ, equations (1.18) and (1.19) are the traditionally accepted solutions for the FB wave frequency and growth rate without having to resort to the typically used restriction that $\gamma << \omega_r$ since the smallness of ψ itself forces γ to be smaller than ω_r, even when ω_r is small (*Drexler and St.-Maurice*, 2005).

For the large ψ values in the dispersion relation, the terms containing $1/\psi$ can be neglected and the dispersion equation becomes:

$$\omega(\omega + i\nu_i) - k^2 C_s^2 \approx 0 \tag{1.21}$$

The solution to equation (1.20) is that of a damped harmonic oscillator. At E-region heights (~ 105 km, $\gamma > 2kC_s$), this results in a wave frequency (ω_r) and growth rate (γ) (*Drexler and St.-Maurice*, 2005) of:

$$\omega_r = \mathbf{k} \cdot \mathbf{v}_{0i} \tag{1.22}$$

and

$$\gamma \approx -\frac{k^2 C_s^2}{\nu_i}, \tag{1.23}$$

where $\mathbf{v}_{0i}$ is the velocity of the ion drift.

For ψ small, the growth rate (equation 1.19) is positive when the electron drift along the wave propagation direction is greater than the ion-acoustic speed. In the auroral E region, the ion-acoustic speed is ~ 400 m/s, which corresponds to an electric field of

20 mV/m. Thus, this is the threshold electric field for the onset of the FB instability at small ψ. At large ψ, the growth rate is always negative at E-region heights (*Drexler and St.-Maurice*, 2005), the origin of which could be related to the transformation of FB irregularities into purely damped modes as a jump in aspect angle is triggered by non-linear and non-local processes.

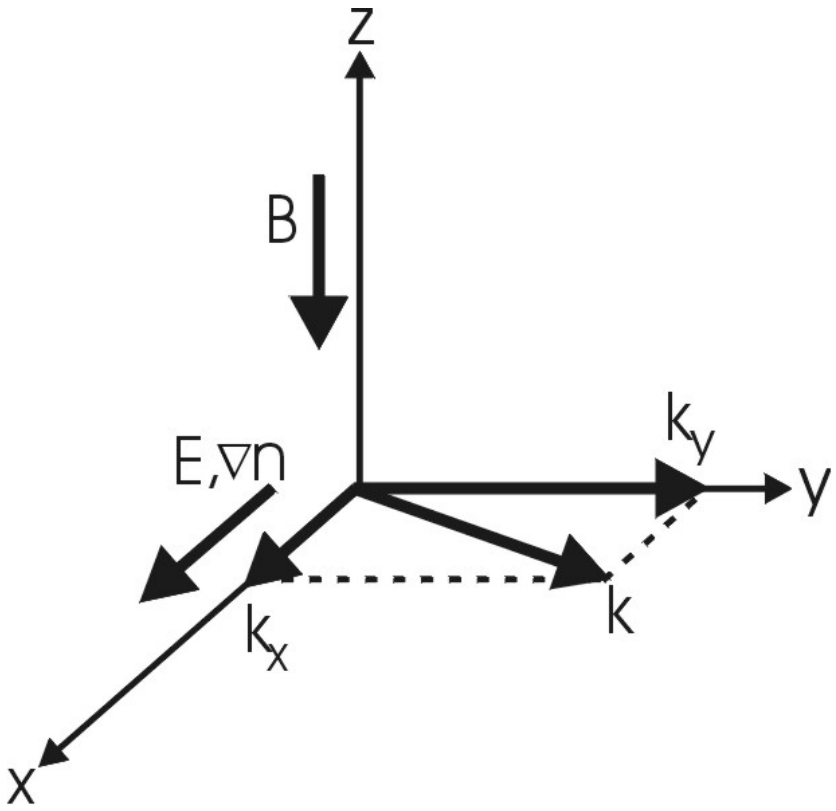

Figure 1.11: Coordinate system and orientation of magnetic field, electric field, wave vector and density gradient adopted for the analysis.

1.4.3 Formation of electrojet irregularities through the Gradient-Drift instability

If a density gradient parallel to the electric field is present at auroral electrojet heights, then the Gradient-Drift (GD) instability becomes possible. For the GD instability to occur, the background density gradient should be directed along the electric field, as shown in Figure 1.11. The analysis is similar to that of the FB instability except the

density is no longer spatially constant and one can neglect the ion inertia. The wave frequency (ω_r) and growth rate (γ) of the GD instability are then (*Kelley*, 1989):

$$\omega_r = \frac{\mathbf{k}\cdot\left(\mathbf{v}_{0e} + \psi\,\mathbf{v}_{oi}\right)}{1+\psi} \tag{1.24}$$

and

$$\gamma = \frac{1}{1+\psi}\left[\frac{1}{Lk}\frac{\nu_i}{\Omega_i}\left(\omega_r - \mathbf{k}\cdot\mathbf{v}_{oi}\right) - \frac{\psi}{\nu_i}\left(k^2 C_s^2 - \omega^2\right)\right], \tag{1.25}$$

where $L = \left(\frac{\nabla n_0}{n_0}\right)^{-1}$ is the gradient scale length.

The GD instability does not have a threshold condition, as long as the wavelengths are long enough (i.e. > 30 m). The instability can lead to the generation of smaller-scale irregularities through cascading of the energy from unstable large-scale waves to linearly-stable short wavelengths (*Sudan et al.*, 1973). In the past, Type 2 echoes were often associated with the effects of the GD irregularity, though it is very likely that secondary waves produced by both the GD and FB instabilities can lead to Type 2 echoes.

Although the description of the linear stage of the FB and GD instabilities is more or less understood. What happens with the instabilities at the later stages, when non-linear effects come into play, is less clear. Numerous theories describing the nonlinear evolution of the FB and GD instabilities were proposed (e.g., *Fejer and Kelley*, 1980; *St.-Maurice and Hamza*, 2008). Application of computer simulations to the evolution of the FB and GD instabilities greatly improved the general understanding of the processes occurring at the non-linear stage. However, agreement of the theoretical conclusions and observations is far from satisfactory (*Fejer and Kelley*, 1980; *St.-Maurice and Hamza*, 2008).

1.5 Objectives of the performed research

The research performed focused on HF radar velocity data collected simultaneously from the E and F regions, with the ultimate goal to better understand the nature of small-scale irregularities in the high-latitude E region. To achieve this goal, joint E-and F-region data, with minimal spatial separation and in all possible flow

directions are considered. *Makarevitch et al.* (2004) conducted this kind of study using the Finland Super Dual Auroral Radar Network (SuperDARN) radar, which has a poleward-oriented Field-of-View (FoV), with their observations being predominantly perpendicular to the electrojet flow. They found that E-region echo velocities were typically 20% of those from the F region and that the direction of the E-region maximum velocity was rotated by ~ 30º clockwise from the F-region flow direction. *Makarevitch et al.* (2004) suggested that the irregularity velocity in the E region was strongly influenced by the ion drift contribution, which is in the direction of the ion Pedersen drift at heights ~ 110 km. We intend to conduct a similar investigation of the E-region HF velocity using the Stokkseyri SuperDARN radar.

The Stokkseyri HF radar in Iceland is convenient because its FoV covers both zonal and nearly meridional directions. In the evening sector, the electric field is typically oriented poleward so that the **E** x **B** convective flow is zonal, roughly in the direction of the magnetic L shells. Consideration of Stokkseyri data is advantageous in a sense that data from observations along the electrojet, the most interesting direction in terms of the plasma physics involved, are available.

The research performed had several objectives. The main objective is to study the velocity of E-region irregularities with respect to the magnitude and direction of the ionospheric electric field (**E** x **B** electron drift). We target the HF radar velocity variation with changing flow angle for various magnitudes of the electric field. The primary focus is on strongly driven electrojet conditions, when the Farley-Buneman instability is certainly present. One interesting question is whether the velocity variation is of the cosine type suggested by *Bahcivan et al.* (2005) at VHF. Two other important questions are whether the E-region velocity along the flow is below or above the ion-acoustic speed and how it compares to predictions of various non-linear theories. An additional objective of the research performed was to understand the additional types of HF echoes identified by *Milan and Lester* (2001). Finally, we will explore *Milan and Lester's* (2004) hypothesis on the High-Aspect Angle Irregularity Region (HAIR) echoes, the echoes at large aspect angles whose velocity is close to the ion drift velocity.

1.6 Thesis outline

The remainder of this thesis is organized as follows. A discussion of the concept of auroral coherent radars and provide information on the SuperDARN network of HF radars including a description of the Stokkseyri radar geometry and raw data analysis, and give a brief summary of the theories concerning the velocity of coherent echoes, the parameter to be targeted in the thesis, in Chapter 2. Measurements of the **E** x **B** drifts in the ionosphere with the DMSP satellites are also described in Chapter 2. In Chapter 3, a comparison of the velocity of E-region echoes and the **E** x **B** drifts measured by DMSP satellites. In Chapters 4 and 5, an analysis of the Stokkseyri data alone by considering echoes at short and far ranges. In Chapter 4, the focus is on one specific event for which the velocity of E-region echoes was persistently close to the ion-acoustic speed of the plasma at the electrojet bottom side. In Chapter 5, we consider a different event for which the observed velocity was much smaller than the ion-acoustic speed. In Chapter 6, we conclude with a summary of the major findings, their discussion and suggestions for future research.

CHAPTER 2

AURORAL ELECTROJET IRREGULARITIES AND THEIR DETECTION WITH COHERENT SUPERDARN HF RADARS

Observations of high-latitude irregularities can be done using a number of instruments, each with its own advantages and disadvantages. A coherent radar is one such instrument. This Chapter introduces the principle of coherent radar observations and show how coherent radar observations are made with Super Dual Auroral Radar Network (SuperDARN) HF radars. We provide additional details about the Stokkseyri radar, located in Iceland, and explain the reasons for considering data from this radar in this thesis. Additionally, a discussion of the general empirical relationships and theories of coherent radar echoes is undertaken. Finally, the measurements of the **E** x **B** plasma drift onboard DMSP satellites are introduced. These data are used to support the research with the Stokkseyri SuperDARN radar.

2.1 Principle of auroral coherent radar operation

Coherent scatter radars are designed to receive echoes from structures (irregularities) within the ionospheric plasma. These structures are stretched along the magnetic field lines due to plasma diffusion in a magnetized environment, and they are produced by various plasma instabilities. In case of the E-region plasma, these mainly are the FB and GD instabilities described in Chapter 1.

If these structures are elongated along the magnetic field direction, any radio wave with a wavelength of double the wavelength of the quasi-periodicity in the structure, $\lambda_{medium} = 2\lambda_{\text{irregularity}}$ (*Fejer and Kelley*, 1980), can result in multiple, in-phase

echoes that constructively interfere, producing a detectable signal, where the incident radio wave must be close to perpendicular (less than about 10º off perpendicular) to the magnetic field at the point of scattering. At equatorial latitudes, this is easy to accomplish because the magnetic field lines are parallel to the ground. At high latitudes, however, the magnetic field lines are nearly perpendicular to the ground, restricting observations from the ground.

At high latitudes, a radar must be located a considerable distance equatorward of the observation volume to reach perpendicularity with the magnetic field. The usage of HF frequency radar is preferred because HF radar waves refract significantly in the presence of ionospheric plasma, and can reach perpendicularity at multiple locations at both E- and F-region heights. The received coherent echoes are typically characterized by power, velocity and spectral width for applications. Coherent radars rely on the Doppler Effect to determine the velocity of an echo. In this case, the Doppler Effect is occurring in a medium of refractive index n_M, and the Doppler velocity becomes (*Rob Gillies*, personal communication):

$$v_{Doppler} = \frac{c\,\omega_{Doppler}}{4\pi\, n_M f_{radar}}. \tag{2.1}$$

Coherent radars have the advantage of relatively low construction and operating costs and can continuously observe large volumes with reasonable spatial and temporal resolutions. However, they are not without their disadvantages, such as radar signals being absorbed in the D region.

Over the last few decades, coherent radars were configured such that two radars would observe the same volume, but from two different positions such that the two radars have multiple crossing beams. Such a configuration allows for the two dimensional determination of the velocity (and the **E** x **B** drift) within the observation volume. The capabilities of coherent radars is what attracts space physicists the most and has spurred construction of such radars and there is still interest in these radars as a means to study the physics of irregularity formation.

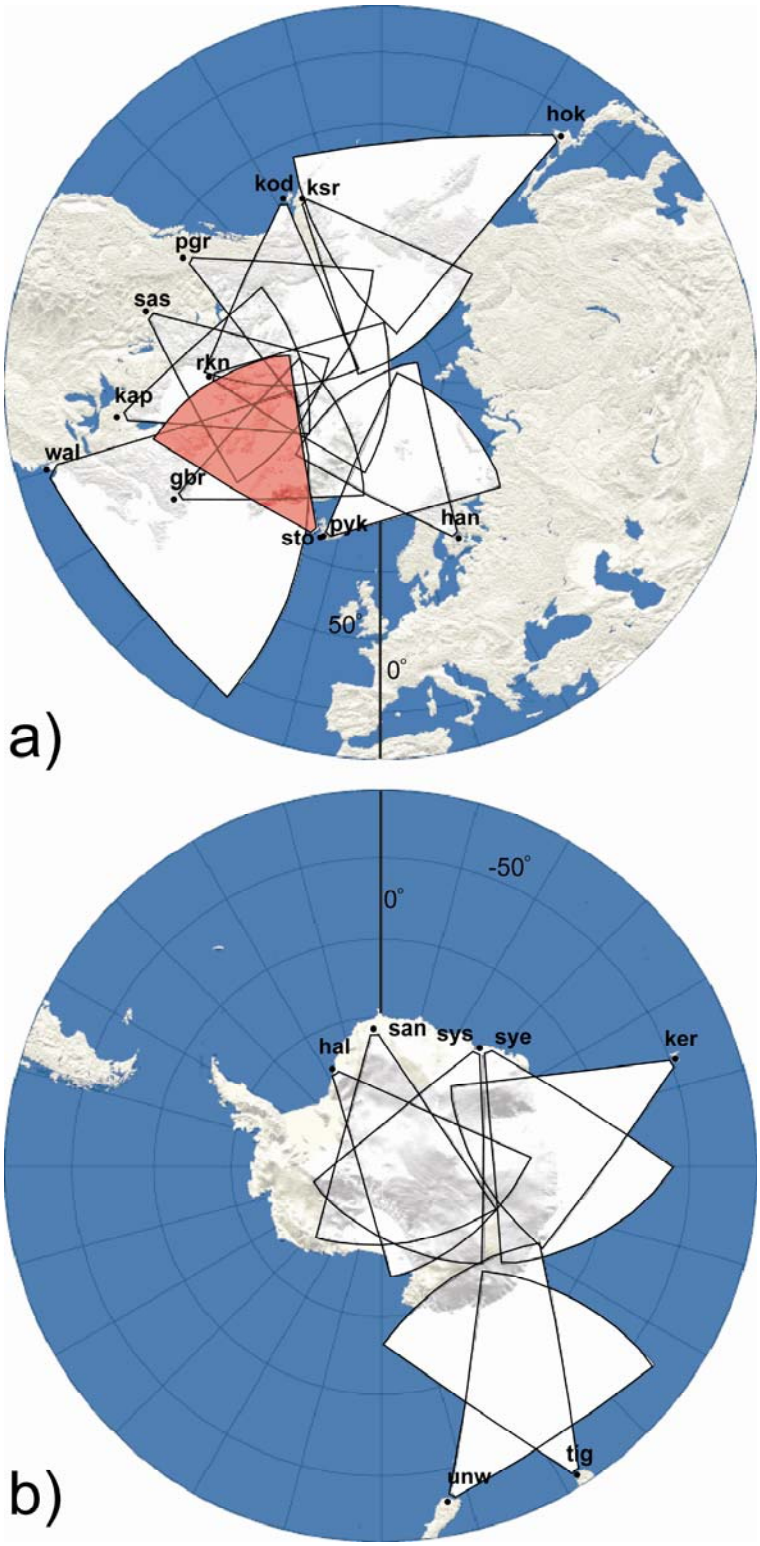

Figure 2.1: SuperDARN radars fields-of-views for the (a) Northern and (b) Southern hemispheres. The field-of-view for the Stokkseyri SuperDARN in the Northern hemisphere, from which data are considered in the thesis, is shown in red (adapted from the APL SuperDARN homepage).

2.1.1 Super Dual Auroral Radar Network (SuperDARN)

SuperDARN (*Greenwald et al.*, 1995) is a multinational collaborative project involving a network of HF coherent radars that monitor most of the polar cap and auroral regions in both hemispheres. The network currently consists of 19 operational stations, with 12 in the northern hemisphere and 7 in the southern hemisphere (Figure 2.1). The position of individual radars in geographic and geomagnetic coordinates, as well as their boresight direction, is provided in Table 2.1. Several additional stations either are under construction or under consideration for construction and are not listed here.

Table 2.1: SuperDARN locations and boresight directions

Radar Station	Station code	Geog. Lat. (ºN)	Geog. Long. (ºE)	AACGM Lat. (ºN)	AACGM Long. (ºE)	Boresight Direction (º)
King Salmon	ksr	58.68	-156.65	57.43	-100.51	-20.0
Kodiak	kod	57.61	-152.19	57.17	-96.28	30.0
Prince George	pgr	53.98	-122.59	59.88	-65.67	-5.0
Saskatoon	sas	52.16	-106.53	61.34	-45.26	23.1
Kapuskasing	kap	49.39	-82.32	60.06	-9.22	-12.0
Goose Bay	gbr	53.32	-60.46	61.94	23.02	5.0
Stokkseyri	sto	63.86	-22.02	65.04	67.33	-59.0
Pykkvibaer	pyk	63.77	-20.54	64.48	68.48	30.0
Rankin Inlet	rkn	62.82	-93.11	72.96	-28.17	5.7
Hankasalmi	han	62.32	26.61	59.78	105.53	-12.0
Wallops Island	wal	37.93	-75.47	30.93	75.52	26.14
Hokkaido	hok	43.53	143.61	38.14	145.67	30.0
Halley	hal	-75.52	-26.63	-61.68	28.92	165.0
Sanae	san	-71.68	-2.85	-61.52	43.18	173.2
Syowa South	sys	-69.00	39.58	-55.25	23.00	165.0
Syowa East	sye	-69.01	39.61	-55.25	22.98	106.5
Kerguelen	ker	-49.35	70.26	-58.73	122.14	168.0
TIGER	tig	-43.38	147.23	-55.31	-133.36	180.0
TIGER Unwin	unw	-46.51	-168.38	-55.15	-106.54	227.9

Each SuperDARN radar scans through 16 beam positions, separated by ~ 3.24º, resulting in a FoV of ~ 52º. Typically, ranges from 180 to 3555 km are arranged in 45 km gates, so that each radar observes upwards of several million square kilometers. SuperDARN radars operate in the common mode the majority of the time, which provides sweeps of 16 beam positions every two minutes, or one minute in the fast common mode, with a dwell time of seven seconds, or three seconds in the fast common mode. The operating frequency uses several discrete bands between 8 MHz and 18 MHz, allowing for observations of coherent structures of 8 to 18 meters in scale.

2.1.2 SuperDARN data analysis using the FITACF approach

To determine the Doppler velocity, echo power and spectral width, SuperDARN uses a multi-pulse sounding technique. Currently an eight-pulse sequence is used and is shown in Figure 2.2. Each pulse in the sequence is 300 μs in duration, and the pulses are separated by non-repeating integer multiples of the 1500 μs lag time. The return signal from this pulse sequence is processed into an auto-correlation function (ACF) dependent on the lag separation. An example of how the ACF is analyzed is shown in Figure 2.3. The real and imaginary components of the ACF versus the lag number are shown in Figure 2.3a, and the analysis is done using the FITACF approach (*Villain et al.*, 1987), which assumes that there is only one peak in the spectrum (Figure 2.3b) and that the ACF decays either exponentially or according to a Gaussian distribution. The Doppler velocity can be found using Equation (2.1) where $\omega_{Doppler}$ is the slope of the plot of the phase difference between the real and imaginary parts of the ACF against the lag number (Figure 2.3c). In this thesis, the uncertainty in the velocity measurements is assumed to be determined from the error in finding the slope of the fit line, a commonly accepted practice with the SuperDARN community. The echo power is determined by fitting the rate of power decay, as shown in Figure 2.3d, to either an exponential or a Gaussian distribution. With an exponential description, the power is given by:

$$P(\tau) = P_{\lambda} e^{-\lambda\tau}, \tag{2.2}$$

and according to a Gaussian description, the power is given by:

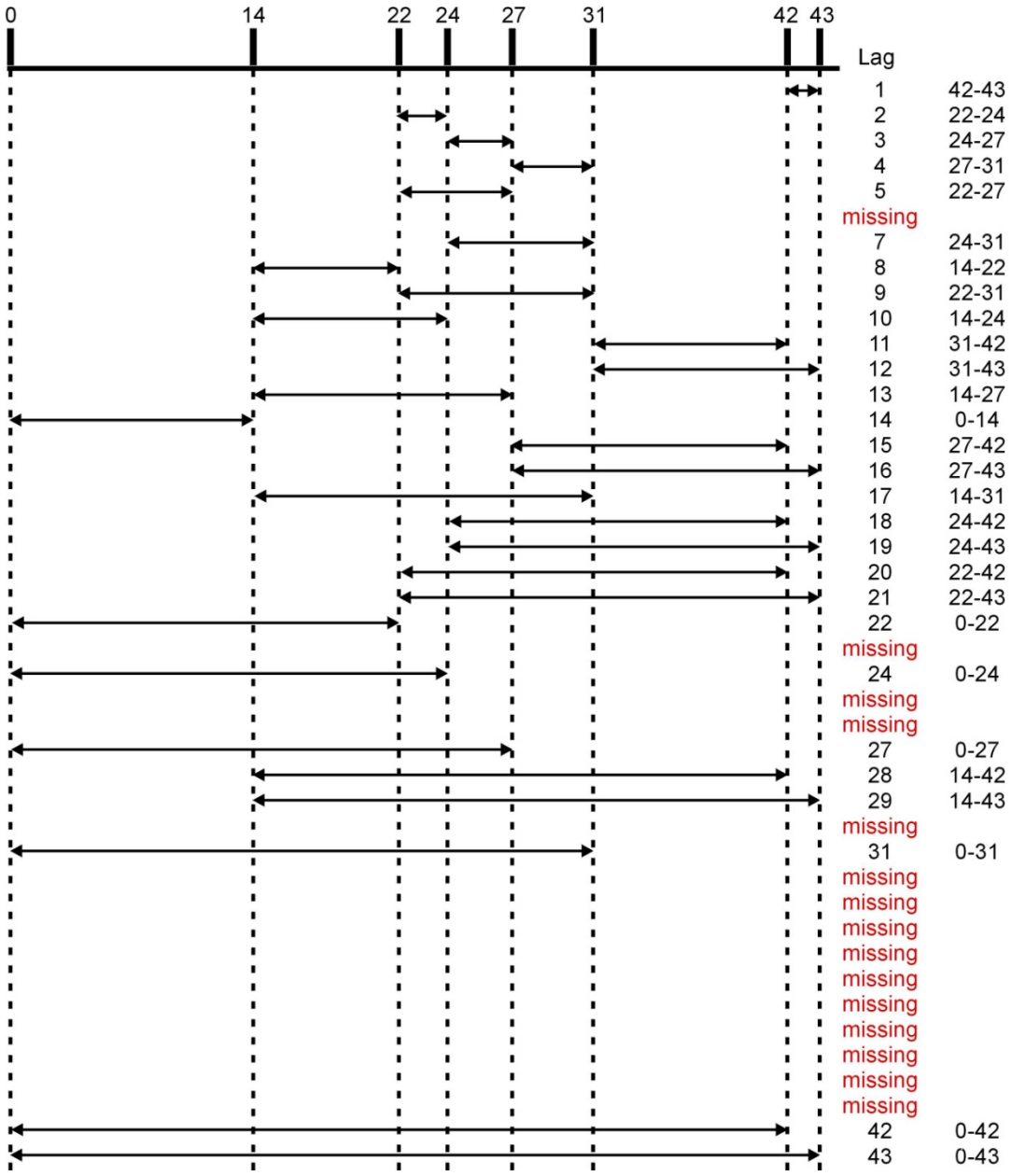

Figure 2.2: A diagram illustrating the 8-pulse sequence currently used in SuperDARN observations (re-created from the original by *K. McWilliams*)

$$P(\tau) = P_{\sigma} e^{-\sigma^2 \tau^2}, \tag{2.3}$$

where the echo power for the exponential and Gaussian distribution decays are P_{λ} and P_{σ} respectively, τ is the number of lags (always positive), and λ and σ are the exponential and Gaussian power decay constants, respectively (*Danksin*, 2003). The width of the

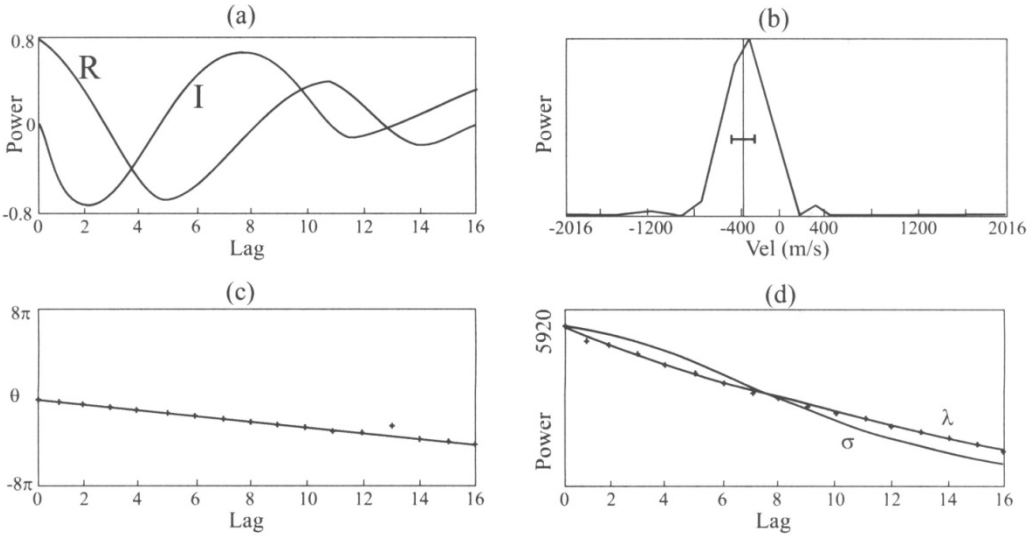

Figure 2.3: A diagram illustrating the principle of SuperDARN data processing (*Villain et al.*, 1987) (a) Real (R) and imaginary (I) parts of the ACF. (b) Magnitude of the FFT of the ACF with velocity (vertical line) and spectral width (horizontal line) obtained using FITACF. (c) Rate of change of the phase angle. (d) ACF power decay for exponential (λ) and Gaussian (σ) least square fits.

spectrum is determined from the coefficients λ and σ from Equations (2.2) and (2.3). According to an exponential distribution, the spectral width is given by:

$$\text{width} = \frac{c\lambda}{2\pi f_{radar}}, \tag{2.4}$$

and according to a Gaussian description, the spectral width is given by:

$$\text{width} = \frac{c\sigma\sqrt{\ln(2)}}{\pi f_{radar}}, \tag{2.5}$$

where f_{radar} is the radar frequency, *c* is the speed of light and λ and σ are the exponential and Gaussian decay constants, respectively.

Originally, SuperDARN radars were designed to be paired to observe a common volume. This was done in order to obtain two components of the Doppler velocity where the beams from the two radars intersected to reconstruct the two-dimensional velocity for each point of intersection in order to construct a global convection pattern. However, data from both of the paired radars are not always available and other methods of convection map determination are desirable. The current method of choice is the Map Potential

approach (*Ruohoniemi and Baker*, 1998). This method fits all available observations to a statistical convection pattern dependent on the IMF conditions. This method allows for a greater utilization of the available data; however, the reliability of these convection maps is dependent on the number of data points that contribute to the final solution as well as the number of spherical harmonics used in the calculation. An example convection map is shown in Figure 2.4.

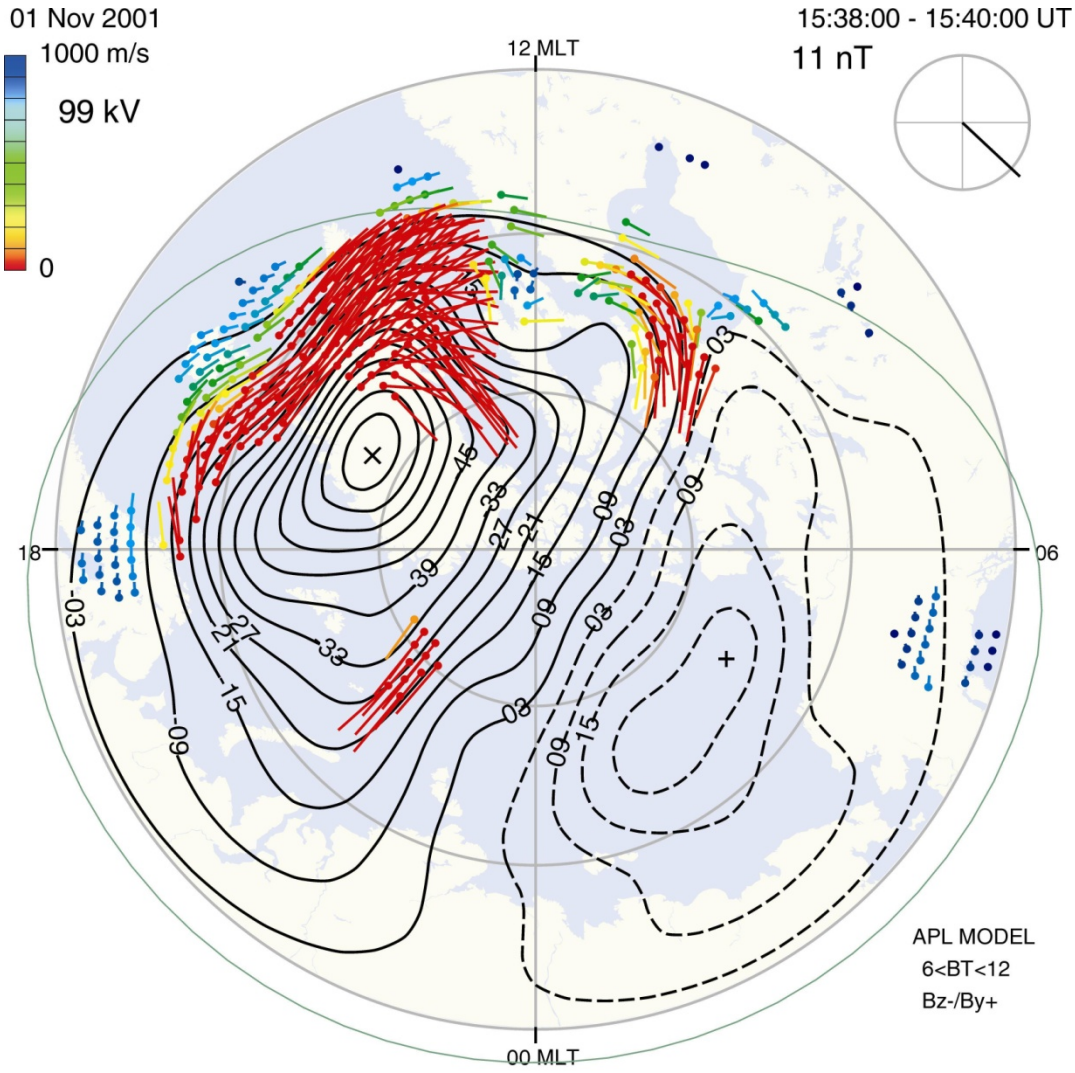

Figure 2.4: Convection pattern determined using Map Potential technique (*Ruohoniemi and Baker*, 1998) for 1 November 2001 at 15:38 – 15:40 UT. The vectors represent the fitted SuperDARN velocities while the solid and dashed lines represent the fitted equipotentials based on the Map Potential technique with a total potential difference between the cross and the plus of 99 kV. The IMF conditions are shown in the upper right hand corner

2.1.3 SuperDARN propagation modes

Since SuperDARN uses radio frequencies in the HF band, the transmitted radio waves are refracted in the ionosphere and the determination between E- and F-region scatter is not easy. Several different radio propagation paths are possible and according to the nomenclature (e.g., *Milan et al.*, 1997) radio waves that produce direct backscatter are referred to as half-hop and are denoted as ½E or ½F depending on which region where the backscatter occurs. It is possible that the radio waves will be refracted through the ionosphere and the backscatter will come from the ground, this is referred to as ground scatter and is denoted by 1E or 1F, depending on which region the radio wave propagated through. Reflection from the ground can also continue forward rather than back to the radar. This forward reflection will proceed to the ionosphere where backscatter from the ionosphere, or another full hop to produce ground scatter, are possible. These two backscatter paths are denoted as 1½E or 1½F for the ionospheric backscatter and 2E or 2F for the ground scatter.

In this thesis, we are only concerned with simultaneous observation of direct ionospheric scatter through the ½E and ½F propagation modes. Figure 2.5 shows an approximate geometry where the ½E backscatter is assumed to originate from ~ 110 km in height from a distance of ~ 300 – 500 km from the radar. Also shown is the geometry of the ½F backscatter, which is assumed to originate from ~ 300 km height at a distance of ~ 1500 km from the radar.

2.1.4 Stokkseyri SuperDARN as an instrument for the study of E-region echoes

The focus of this thesis is the investigation of the relationship between the velocity of HF echoes (electrojet irregularities) and the $\mathbf{E} \times \mathbf{B}$ drift, the major factor driving electrojet instabilities.

The majority of northern hemisphere SuperDARN radars have a poleward oriented boresight, which is often across or oblique to the flow direction. Observations along the flow directions for long periods are limited to few SuperDARN radars; one such radar is the Stokkseyri radar.

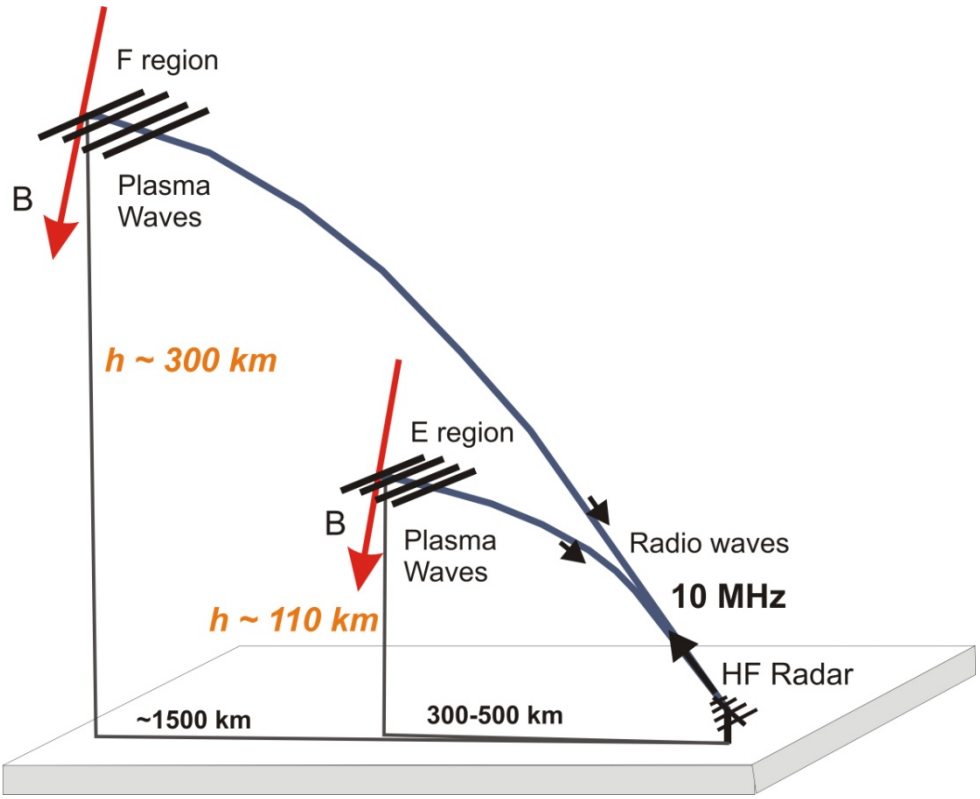

Figure 2.5: Geometry of simultaneous detection direct scatter from E and F regions using SuperDARN HF radar (not to scale).

The Stokkseyri SuperDARN station, with FoV shown in red in Figure 2.1, is located in Iceland and is operated by *Centre National de la Recherché Scientifique* in France. The Stokkseyri radar is of particular note due to two features not common for others. The first feature is the orientation of its FoV with respect to the magnetic L shells, which we define as the angle between the lines of constant magnetic latitude, according to the Altitude Adjusted Corrected Geomagnetic Model (AACGM) as a reference, and the line-of-sight of each range gate. For Stokkseyri, the L-shell angle varies from 5º equator-ward of the L-shell direction to 75º poleward of the L-shell direction within the first 40 range gates as shown in Figure 2.6. This large range of L-shell angles allows a study of the flow angle variation of the velocity.

The second feature of interest is the aspect angle conditions for various electron densities at E-region heights. Figure 2.7 shows how the lines of zero aspect angle change with refraction at 110 km for electron density peaks ranging from 3.5×10^{10} to 10×10^{10} m^{-3}. For typical E-region densities of 10^{11} m^{-3}, E-region echoes can be

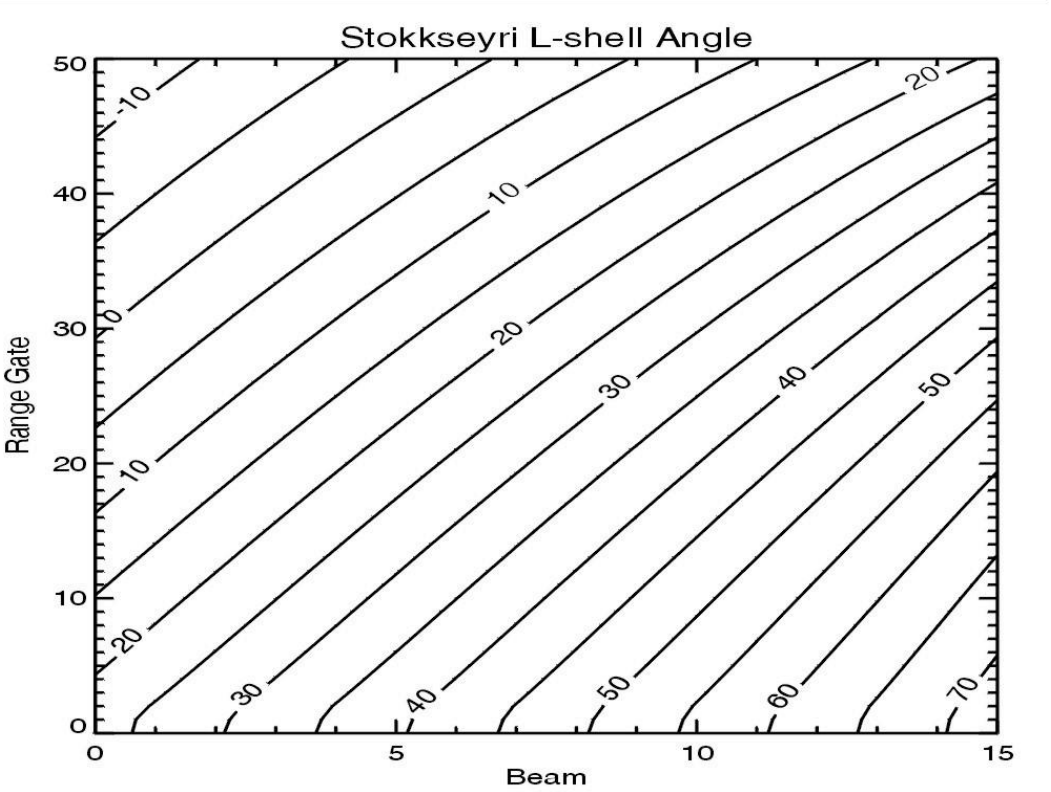

Figure 2.6: Stokkseyri SuperDARN L-shell angle plot for range gates 0 – 50 and beams 0 – 15. Shown are the contours of constant L-shell angle as calculated from spherical geometry and the AACGM magnetic field model.

detected from 300 to 500 km, in a band stretching across the entire FoV, which allows for identification of E-region echoes. Figure 2.8 shows an example of data from Stokkseyri for 19 November 2001 at 19:00 UT, where the band of E-region echoes at 300 to 500 km is evident, as well as typical F-region echoes at farther ranges.

2.2 Theory and experiment on the phase velocity of auroral electrojet irregularities

The goal of this thesis is to study of the velocity of E-region irregularities. In this section, we first consider some hypothesis of the FB instability theory with respect to the velocity of electrojet irregularities and give a brief review of the non-linear theories proposed to explain what has been observed.

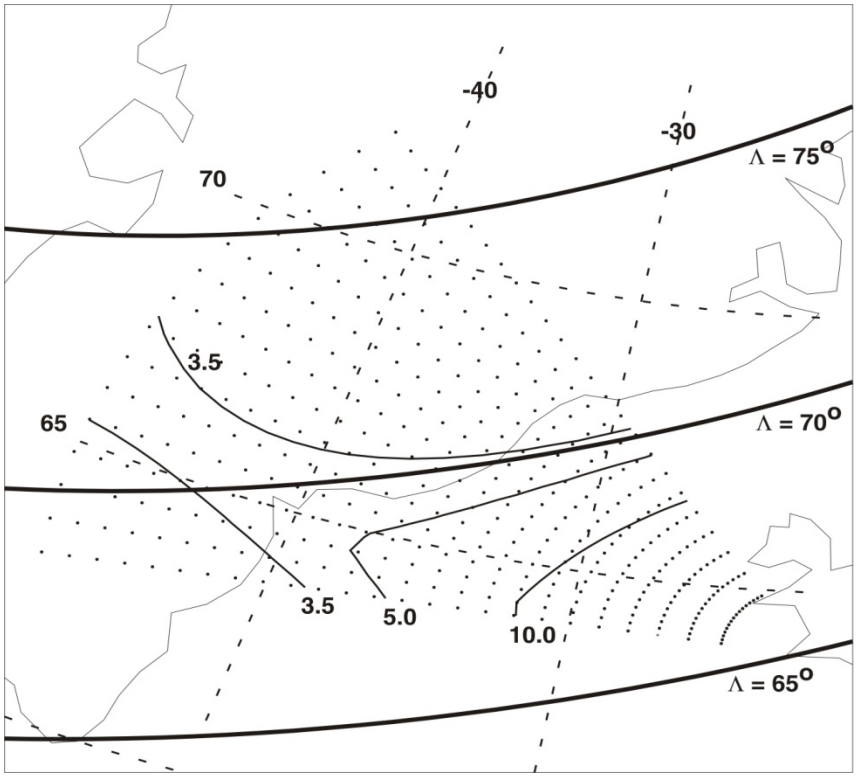

Figure 2.7: The field-of-view of the Stokkseyri SuperDARN radar for ranges 180 – 1260 km. Each dot represents the location of the beginning of a radar cell. A height of 110 km is assumed. The thin lines are the zero aspect angle lines for the shown peak electron densities (shown in units of 10^{10} m^{-3}) at 110 km for a radar frequency of 12 MHz. The thick lines are the AACGM magnetic latitudes (from *Koustov et al.,* 2005)

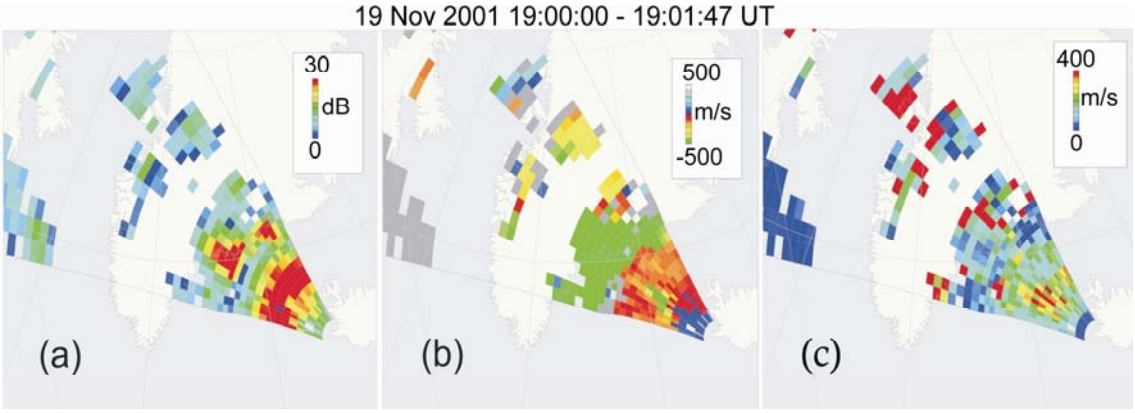

Figure 2.8: Stokkseyri SuperDARN radar parameter maps obtained on 19 November 2001 at 16:06:00-16:07:49 UT. For the analysis, echoes in bins 3-10 (315 – 630 km) were considered as coming from the electrojet heights while echoes in bins 11-40 (675 – 1980 km) were considered as coming from the upper E and F regions. Shown in panels are (a) Power (0 – 30 dB), (b) velocity (-500 –500 m/s) and (c) spectral width (0 –400 m/s) of echoes.

2.2.1 Linear theory of electrojet instabilities on the phase velocity of irregularities

As presented in section 1.4.2, the electrojet instability wave frequency (ω_r) depends on the parameter ψ, which in turn depends on the aspect angle (α_o). From Equation (1.18), the phase velocity for small aspect angle ($\alpha_o << 1^o$), where ψ is much less than one, is:

$$v_{ph} = \frac{\omega_r}{k} \approx v_{oe} \cdot \cos\theta. \tag{2.6}$$

Therefore, for small aspect angles, the phase velocity is proportional to the electron drift velocity and the cosine of the flow angle.

The value of ψ becomes much larger than one if the aspect angle is above $1^o - 2^o$ (*Kelley*, 1989). In this case, we must use the wave frequency of equation (1.21) to determine the phase velocity. If we consider β being the angle between the wave vector (**k**) and the ion velocity vector ($\mathbf{v}_{0i}$) we then get a phase velocity of ($\gamma > 2kC_s$):

$$v_{ph} = \frac{\omega_r}{k} \approx v_{0i} \cos\beta. \tag{2.7}$$

Therefore, for large aspect angles, the phase velocity is controlled by the ion drift term. It is evident from Equation (1.22), that at large values of ψ, the waves are strongly damped and the existence of such a wave is questionable. *Drexler et al.* (2002) proposed a non-local theory for the evolution of decameter structures employing mode coupling that deviates from the traditional plane wave approach of explaining echoes observations. Structures explained in this way can reach high aspect angles and *Drexler and St.-Maurice* (2005) proposed this argument to explain recent weak, short-ranged observations of unusually large aspect angle echoes.

2.2.2 Ion-acoustic saturation and flow angle variation of the velocity of unstable Farley-Buneman waves

As presented in the previous section, the expectations according to linear theory of the FB instability are that the irregularity phase velocity can be as large as $\frac{E}{B}$, which can amount to 1 – 2 km/s in the high-latitude ionosphere. However, in the developed state

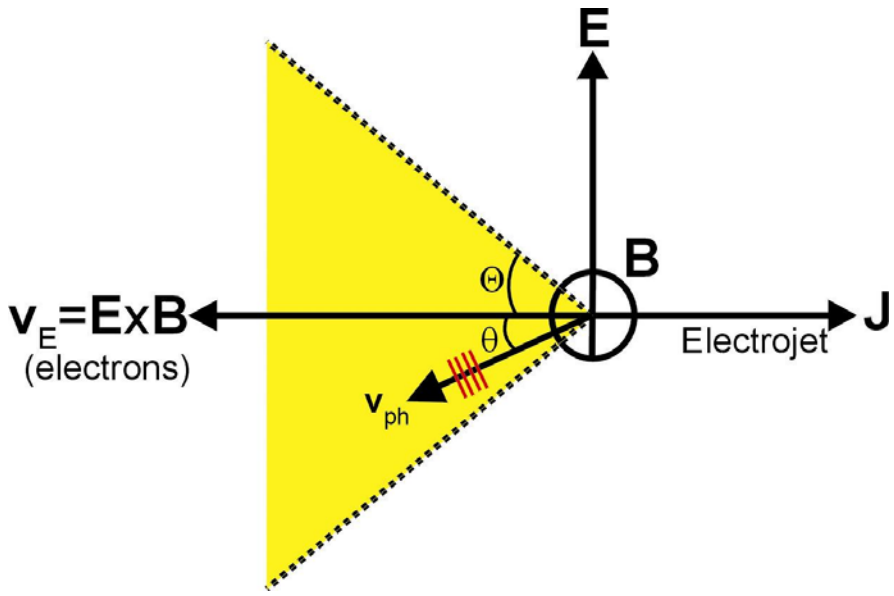

Figure 2.9: The instability cone within which the Farley-Buneman instability is expected to occur with respect to magnetic field, electric field and electrojet direction for observations at high latitudes.

of the instability, various non-linear effects come to play, and the irregularity velocity can be quite different from the linear theory expectations. Predictions based on observations have proposed that the FB irregularity phase velocity saturates at the ion-acoustic speed C_s.

This saturation is expected to occur within the cone of flow angles where the electron drift along the wave propagation direction is greater than the ion-acoustic speed ($\omega_r \geq kC_s$). Figure 2.9 shows the FB instability cone where the electron drift along the wave propagation direction is greater than the ion-acoustic speed. The FB instability cone has an angular half width of Θ, where Θ is given by:

$$\cos\Theta = \frac{C_s}{v_E}. \tag{2.8}$$

Other investigations of the flow angle variation of the echo velocity have arrived at contradictory results (*Makarevitch*, 2003). Some studies reported a cosine variation of the velocity with flow angle (as predicted by Equation (2.7)) while others have not seen such variation. Recently, two papers were published that addressed this question in an empirical way. *Nielsen et al.* (2002) considered data at 140 MHz and showed that the velocity variation with the flow angle can be described as:

$$V_{ph} = m^{\xi} C_s \cdot \cos^{\xi}\theta\,, \tag{2.9}$$

where the coefficient of proportionality m is of the order 1.3 and the value of ξ changes from 0.8 to 0.2 with an electron drift increase from 600 to 1600 m/s. On the other hand, *Bahcivan et al.* (2005) proposed that:

$$V_{ph} = C_s \cos\theta\,, \tag{2.10}$$

and presented data at 30 MHz supporting this hypothesis.

Some recent HF studies, notably *Makarevitch et al.* (2002b, 2004), showed a number of interesting features. They found that there is a frequency dependence on the observation of different populations of echo classes and that those classes seem to demonstrate different variations of echo velocity with L-shell angle. They also found that the E- and F-region echo velocities differ in the direction of maximum velocity magnitude; the E-region velocity is maximized in the direction ~ 30º clockwise of the F-region velocity maximum.

The saturation of FB waves at the ion-acoustic speed is thought to be related to the condition of marginal stability, the regime of very small growth rates (*Kelley*, 1989). Under marginal stability, the phase velocity of FB instability waves can be limited to the ion-acoustic speed. At large electron drifts, far in excess of the ion-acoustic speed, the velocity saturation at C_s can occur partly because the electrons are heated by large amplitude structures, and the increased ion-acoustic speed can provide the condition for zero growth (*St.-Maurice et al.*, 1981).

Several additional theories have been proposed in order to explain the saturation of FB waves at C_s. At first, an anomalous diffusion theory was proposed that proposed an extremely large anomalous electron collision frequency increase, significantly in excess of the electron collision frequency (*Kelley*, 1989). This theory would imply an increase the diffusion of FB waves in direction perpendicular to the magnetic field, leading to a decreased velocity due to an increased ψ. This theory has many flaws (*St.-Maurice*, personal communication, 2008) and has been largely rejected as an explanation for the C_s saturation effect.

With the plausibility of these large anomalous electron collision frequencies unlikely, several alternative theories were proposed. *Hamza and St.-Maurice* (1993) and

Otani and Oppenheim (1998, 2006) considered mode-coupling mechanisms of FB instability saturation, where the energy from growing waves is transferred to stable modes, so that equilibrium is achieved in the final turbulent state. In these theories the velocity saturation is explained, but begins to fall apart at large electric fields greater than ~ 40 mV/m (*J.-P. St-Maurice*, personal communication, 2008). Additionally, St.-Maurice and Hamza (2001) proposed a theory of elongated structures that slow down and rotate as they grow in amplitude. These structures would effectively be hard targets for radar scatter and the behaviour of these structures could explain the C_s saturation effect.

2.2.3 Turbulent heating due to FB waves

As has been shown in Section 1.3, a relative drift (changing with height) exists between the ions and electrons in the ionosphere in a plane perpendicular to the magnetic field. This implies the presence of a horizontal current. Such a current in a conductive medium leads to Joule heating of the medium. In practice, Joule heating rates are estimated from the product of the current density **J** and the electric field **E** (*Baumjohan and Treumann*, 1996):

$$Q_J = \mathbf{J} \cdot \mathbf{E}. \tag{2.11}$$

Equation (2.12) implies that only a current component along the electric field is important, the so-called Pedersen current. In the ionospheric E region, Joule heating of the ions is often detected at heights greater than 120 km with a temperature increase by a factor of two or more. The heating for the electrons is expected to be less significant. Observations, however, revealed anomalous electron heating by a factor of two or more between the heights of 100 and 120 km (*Schlegel et al.*, 1981; *St.-Maurice et al.*, 1981; *Milikh and Dimant*, 2002, 2003; *Dimant and Milikh*, 2003). The effect was found to depend on the magnitude of the electric field and is only obvious for electric fields greater than 50 mV/m (*St.-Maurice et al.*, 1999).

To illustrate the phenomenon, the electron and ion temperatures according to observations with the incoherent scatter radar EISCAT on 16 September 1999 are shown in Figure 2.10 for electric field values of 27 mV/m and 51 mV/m. At 27 mV/m, the electron and ion temperatures (and the temperatures of neutral particles) are all roughly

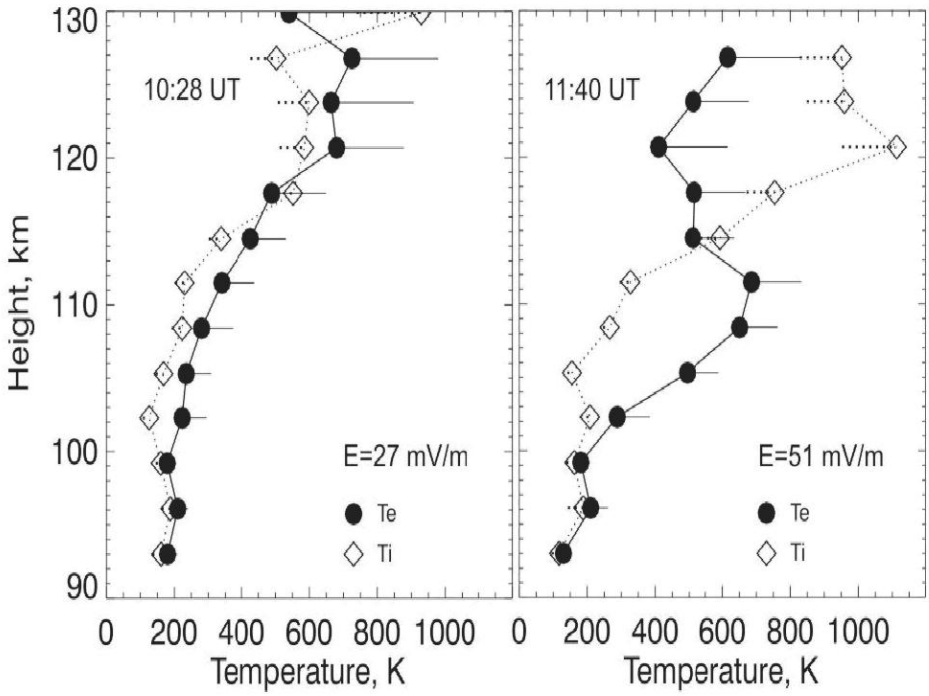

Figure 2.10: Electron and ion temperature profiles for heightss ranging from 90 to 130 km for electric fields of 27 and 51 mV/m. Observation obtained from EISCAT on September 16, 1999 (Courtesy of *A. V. Koustov*).

equal. At 51 mV/m, strong anomalous heating of electrons is evident in the 100 to 120 km height range. Above 120 km, heating of the ions is also evident; this is due to Joule heating produced by the background electric field.

The anomalous increase of electron temperatures at auroral electrojet heights was explained by the turbulent heating of the background plasma due to the presence of FB waves (*Schlegel et al.*, 1981; *St-Maurice et al.*, 1981; *Milikh and Dimant*, 2002, 2003; *Dimant and Milikh*, 2003). When the auroral electric field exceeds the threshold value of $E_{th} \approx 20$ mV/m the FB instability develops, and turbulent electric fields coupled with plasma density perturbations are excited. It is believed that these turbulent electric fields cause Joule heating of the electrons (*St.-Maurice and Laher*, 1985; *Milikh and Dimant*, 2002, 2003; *Dimant and Milikh,* 2003). The efficiency of the heating depends also on the cooling rates (well known as a function of the electric field strength, *St.-Maurice*, 1999) of electrons interacting with neutral particles, and the exact quantitative description of the balance between the electron heating rates and losses remains to be developed.

2.3 Ion drift measurements in the high-latitude ionosphere onboard DMSP satellites

In this thesis, data from the Defense Meteorological Satellite Program (DMSP) satellites was used. DMSP (*Greenspan et al.*, 1986; *Rich and Hairston*, 1994) is a US Department of Defense satellite series used in weather forecasting since the first satellite in the series was launched in 1965. DMSP series satellites operate in a circular polar orbit at a height of approximately 840 km, with an orbital period of ~ 100 minutes and are inclined at 98.7º to produce an orbit that crosses the equator at a fixed local time throughout its orbital precession. Of the many instruments aboard DMSP, this research is only concerned with the ion drift velocity instruments that have been a part of the DMSP series satellite instrument package since 1987.

Ion drift velocity measurements are performed with a thermal plasma detector array called Special Sensor for Ions, Electrons, and Scintillations (SSIES) instrument. The two detectors on this instrument that measure ion drifts are the Ion Drift Meter (IDM) and the Retarding Potential Analyzer (RPA). Both instruments are mounted facing the direction of the spacecraft's motion and are shielded by a biased wire mesh to repel electrons but allow ions to pass through without altering the flow direction. The RPA measures the along-track ion drift, as well as temperature, density and composition, to determine the velocity of the ions relative to the spacecraft. The IDM measures the cross-track component of the ions relative to the Earth by measuring ion currents from the plasma incident on the collector surface. The IDM measurements, however, are dependent on the RPA measurement of the ion velocity relative to the spacecraft. In situations where RPA measurements are not available, the IDM uses assumptions that can introduce an error on the order of 10% in the measured ion drift velocity. Additionally, the RPA measurements assume the most abundant ions are O^+ and when this assumption fails, the RPA measurements can be unreliable (*Greenspan et al.*, 1986).

2.4 Summary

In this chapter, some of the basic principles of coherent radar observations and their common uses were summarized. The coherent radar network used in this thesis,

SuperDARN, was introduced and general information about the network and the data analysis techniques was discussed. The reasons behind selecting the Stokkseyri SuperDARN station as our primary source of data were also discussed.

In order to facilitate an understanding of the motivations behind investigating the characteristics of the flow angle variation of the E-region velocity, several the theories of electrojet instabilities directly concerning coherent radars were discussed. The expectations of linear theory do not hold in the E-region, and one must consider empirical prediction on the velocity of E-region echoes as well as the non-linear theories that have been presented to explain the empirical predictions.

Finally, an introduction to the DMSP series satellites was presented with an explanation of how **E** x **B** drift measurements are made onboard the satellite. DMSP measurements were used in the investigations of Chapters 3 and 4.

CHAPTER 3

RELATIONSHIP BETWEEN THE VELOCITY OF E-REGION HF ECHOES AND THE E x B PLASMA DRIFT

In this Chapter, the value of the HF Doppler velocity with respect to the **E** x **B** drift is investigated. The major problem in addressing this issue is the significant difficulty of obtaining contemporaneous data; one needs an HF radar capable of detecting echoes over an area where the **E** x **B** vector is monitored continuously by an independent instrument. One such instrument can be an incoherent scatter radar. It would be reasonable to expect that the currently existing chain of SuperDARN HF radars (*Greenwald et al.*, 1995) should provide ample data to work with. However, appropriate data can only be collected in a short-range viewing zone of the Hankasalmi-Finland radar over the position of the tri-static mode of the incoherent scatter radar EISCAT. The analysis of Hankasalmi data indicates that the majority of echoes near the volume observed by the EISCAT tri-static radar mode come from the F region (e.g., *Davies et al.*, 1999; *Danskin et al.*, 2002).

For **E** x **B** magnitude estimates, we consider measurements onboard DMSP satellites crossing the Stokkseyri radar FoV. Unfortunately, because the data available are often only reliable for the component of the **E** x **B** drift across the satellite track, the comparison is not fully 2-dimensional, and one cannot say definitively at what flow angles the comparison is performed. Results presented in this Chapter were published in *Koustov et al.* (2005).

3.1 Previous studies and justification

According to the linear theory of the FB and GD instabilities, Equation (2.6), the velocity of plasma irregularities is, to a first approximation, the cosine component of the

E x **B** drift. This expectation has been widely used for plasma convection monitoring in VHF experiments, such as in the Scandinavian Twin Auroral Radar Experiment (STARE) (*Greenwald et al.*, 1978; *Nielsen and Schlegel*, 1985). For the success of the convection estimates, it is fundamentally important that the velocity magnitude is proportional to $\frac{E}{B}$ and varies as a cosine function of the flow angle.

VHF observations showed (Chapter 2), however, that the relationship between the velocity of electrojet irregularities and the **E** x **B** plasma drift is more complicated, especially for the condition of strong plasma flows of $\left|\frac{E}{B}\right| > C_s$ (where C_s is the ion-acoustic speed, roughly 400 m/s), when the FB instability is the prime factor controlling the irregularity production. Empirical explanations of the observed nonlinear effects postulate that the maximum phase velocity of the FB-related irregularities is close to the ion-acoustic speed within a relatively broad cone of flow angles (*Nielsen and Schlegel*, 1985). This property is often referred to as the C_s saturation of the irregularity velocity (*Nielsen and Schlegel*, 1985). Previous VHF observations showed that indeed the velocity of echoes observed within the FB instability cone is close to C_s, typically slightly above it (e.g., *Nielsen et al.*, 2002). Similar results were obtained at ultra high frequency (UHF) (*Foster and Erickson*, 2000).

Outside the FB instability cone, it is believed (e.g., *Nielsen and Schlegel*, 1985) that the irregularities (sometimes called the secondary irregularities) move with the velocity $v_{oe}\cos\theta$, as prescribed by the linear theory. VHF observations at large flow angles, outside the FB instability cone, are somewhat controversial. Evidence has been presented that the line-of-sight (l-o-s) velocity is, to a first approximation, the cosine component of the **E** x **B** plasma drift (*Reinleitner and Nielsen*, 1985; *Nielsen et al.*, 2002), especially at 50 MHz (*Ecklund et al.*, 1977). However, *Kustov and Haldoupis* (1992) published STARE data for large flow angles indicating that the l-o-s velocity can be 10 – 20 % smaller than the plasma drift component along the beam. This velocity difference was attributed to the aspect angle effect. Such interpretation is consistent with the generally accepted notion that the VHF velocity is aspect-angle sensitive, implying that the expected l-o-s velocity at certain radar directions cannot be computed by simple

multiplication of $\frac{E}{B}$ and the cosine of the flow angle (e.g., *Ogawa et al.*, 1982; *Nielsen*, 1986; *Kustov et al.*, 1994; *Kustov et al.*, 1997). More recently, *Koustov et al.* (2002) reported an even stronger STARE velocity depression, though this effect might be attributed to the shorter pulse separation in the modified STARE system.

The relationship between the velocity of HF coherent echoes and the **E** x **B** plasma drift has been investigated less than at VHF and UHF. As mentioned, the major problem is the significant difficulty of getting contemporaneous data. A limited EISCAT-Hankasalmi E-region HF velocity comparison by *Davies et al.* (1999) showed that the l-o-s velocities were typically smaller than the **E** x **B** flow components. Unfortunately, no information on the flow angle of the observations was provided.

E-region HF radar observations alone, without complementary **E** x **B** measurements, are contradictory. At small flow angles (presumably within the FB instability cone), a clear statistical clustering of HF velocities near 400 m/s (typical C_s value) was reported (*Hanuise et al.*, 1991; *Milan and Lester*, 2001). On the other hand, velocities of more than 700 m/s are not rare (*Milan and Lester*, 1998; 2001) and a strong velocity change with the flow angle within the FB instability cone has been reported (*Milan and Lester*, 2001; *Uspensky et al.*, 2001; *Makarevitch et al.*, 2002b). We should note that the velocity variation with the flow angle inside the FB instability cone was recently reported for the STARE radars (*Nielsen et al.*, 2002).

Large flow angle HF observations, *Koustov et al.* (2002) and *Makarevitch et al.* (2004) presented evidence from indirect measurements that the velocity of E-region HF echoes is significantly smaller than the **E** x **B** component. These results seem to disagree with the ones reported by *Jayachandran et al.* (2000) who compared DMSP ion drift measurements and Saskatoon HF data for observations at large flow angles and concluded that the HF velocity does indeed correspond to the DMSP drift.

In this Chapter, we continue the investigation of the relationship between the Doppler velocity of E-region HF echoes and **E** x **B** plasma drifts by considering the Stokkseyri HF radar measurements and DMSP ion drifts. The Stokkseyri observations were selected for a simple reason that as the DMSP satellites cross this radar FoV, their cross-track directions are almost a perfect match to some of the radar beam orientations.

Thus, a direct comparison of the **E** x **B** component and the radar l-o-s velocity can be performed without invoking the assumption that the irregularity velocity changes with the flow angle according to the cosine rule.

3.2 Experiment configuration and data selection

Stokkseyri SuperDARN data from the standard mode of operation are considered (scanning from beam 15 to beam 0 in one/two minutes). The data set consisted of power, velocity and width estimated according to the FITACF procedure (Chapter 2). For the selection of pure E-region events, several conditions were considered, as the HF echoes were often observed as a broad region extending from 300 to > 800 km. Analysis of the aspect angle conditions (Figure 2.7) shows that the E-region echoes should be aligned in the southeast to northwest direction and tilted at an angle of ~ 30º with respect to the magnetic L-shell directions. In addition, because the range of perfect aspect is less in smaller-numbered beams, one would expect the power to be stronger in those beams.

Another criterion for the event selection was that the echo region should be limited to a few hundred kilometers in range, since the aspect sensitivity of E-region echoes should confine the echoes to limited bands. For some events, the echo regions were quite broad, but the Doppler velocity scans clearly indicated that the far edge of the echo region had a much higher velocity, hinting that these are F-region echoes (*Makarevitch et al.*, 2004). Finally, for many events, additional confirmation that these were indeed E-region echoes comes from the simultaneous detection of F-region echoes or ground scatter at ranges consistent with the appropriate propagation modes with the detections of E-region echoes, similar to *Milan and Lester* (1998).

Identification of E-region echoes was an important part of the work but the final and the most crucial step in the event selection was the consideration of concurrent DMSP ion drift measurements. The southwest to northeast orientation of the E-region echo bands for the Stokkseyri radar dictates that the DMSP trajectories have to pass the Stokkseyri FoV at short ranges roughly along these orientations to enable a direct comparison of the radar velocities and the **E** x **B** flow.

Figure 3.1 gives an example of the Stokkseyri velocity observations on 3 November 2002 at 12:52 – 12:53 UT. Two regions of echoes are evident with one at

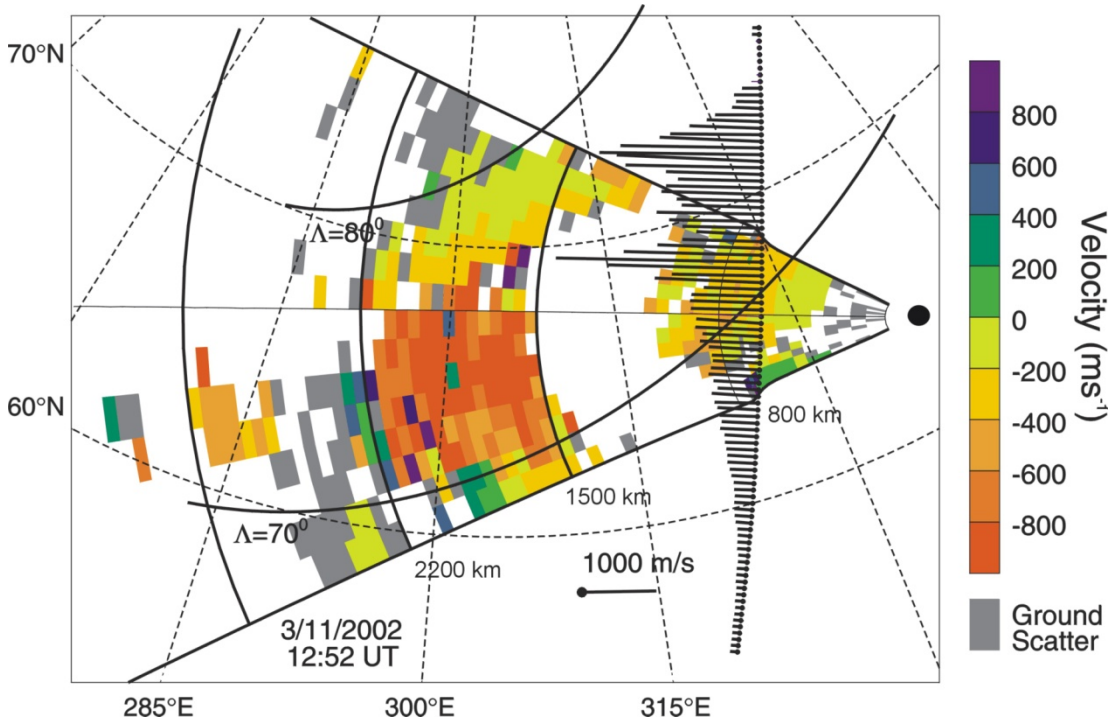

Figure 3.1: The Stokkseyri velocity map at 12:52 – 12:53 UT on 3 November 2002 and DMSP cross-track ion drifts along the satellite track over the radar field-of-view (*Koustov et al.*, 2005).

short ranges (E-region echoes) and the other one at far ranges (F-region echoes). Even though the echo regions occur at about the same magnetic latitudes, the F-region velocities are at least two times larger than the E-region velocities.

Also shown in Figure 3.1 is the trajectory of the DMSP F15 satellite and the measured cross-track **E** x **B** ion drift. The DMSP measurements were performed at a height of ~ 840 km; the track shown in Figure 3.1 is the projection of the satellite location along the magnetic flux lines to a height of 110 km. Such a projection was done to facilitate a direct comparison of the DMSP drifts and the Stokkseyri l-o-s velocities. For the projection, the magnetic coordinates of the satellite location were traced down along the same flux line according to the ACCGM model assuming that the electric field does not change with height. This introduces an 11% shift in the velocities (*St.-Maurice*, personal communication, 2006). In Figure 3.1, one can notice that the DMSP drifts are comparable in magnitude with the Stokkseyri far-range F-region velocities (beyond 1500 km), and they are definitely larger than the velocities of the short-range E-region echoes. Figure 3.1 shows that as the satellite travels to lower latitudes it crosses radar

beams at almost 90º angles. This is an important requirement for the present work, since the DMSP ion drift measurements along the satellite path are not as reliable as cross-track measurements. The azimuth difference between the DMSP direction of measurements and the Stokkseyri radar beam were computed so that a comparison at various orientations between the radar beams and the cross-track directions was possible to perform. A similar geometry of SuperDARN and DMSP measurements was sought for other SuperDARN radars but only the Stokkseyri and Syowa-East radars were consistently satisfactory.

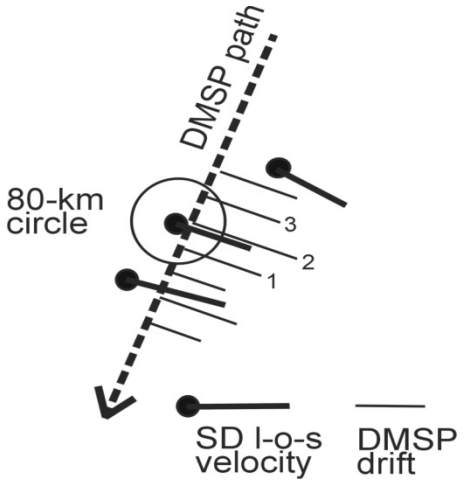

Figure 3.2: A schematic illustrating the principle of DMSP ion drift data averaging for the comparison with the SuperDARN line-of-sight velocities.

It is important to note that DMSP passes over the Stokkseyri field-of-view between 08:00 UT and 13:00 UT, which corresponds to the pre-noon (07:00 – 12:00) magnetic local time (MLT) sector. This is a poor time for the detection of E-region HF echoes, as they are more frequent during the evening hours and nighttime (*Milan et al.*, 1997; *Danskin et al.*, 2002). Figure 3.2 illustrates our approach to the data comparison. We used 4-second averaged DMSP ion drifts corresponding to the spatial resolution of ~ 30 km. The Stokkseyri data were integrated over ~ 3 s (1 min scans) or ~ 7 s (2 min scans) at every beam position and for every 45 km range cell. There was no exact correspondence of the satellite and radar measurements in terms of either time or location. To minimize temporal differences, we considered only the Stokkseyri scan that corresponded to the time of DMSP crossing the central beams of the radar. Spatially, each radar cell was associated with three measurements of the DMSP that were less than

40 km away from the observation location and for the comparison, the averaged DMSP ion drift at these measurements along the track was used.

Originally, over 60 passes with the proper trajectory orientation were located for observations in 1999 – 2002 (the period for which the DMSP drift-meter data were accessible to us). Out of these, about half of the passes were not considered for further assessment for a variety of reasons. For some events, the DMSP data were not continuous or had high variability. Besides concerns about the quality of the DMSP data, such cases might indicate the patchiness of the ionosphere, and comparison with HF data would not produce meaningful results since the obtained discrepancies could be explained by spatial and temporal differences in measurements. Some events were also excluded from consideration based on the quality of the data.

After this thorough selection, 29 events of reasonable quality were entered into the database and are shown in Figure 3.3. We should note that the DMSP/Stokkseyri comparison for all of the original events, without careful checking of the data quality, show tendencies similar to the ones for the selected events, but with more significant spread in the data. Note that as discussed in Chapter 2, the along-track component of DMSP is considered unreliable so only the cross-track component is used.

3.3 Results of the comparison

In Figure 3.3, we compare the Stokkseyri l-o-s velocities with the DMSP ion drifts for the 29 joint events. A strict analysis requirement that the azimuth of the DMSP cross-track velocity and the azimuth of the Stokkseyri beam differ by less than 5º was selected. The vertical bar for the HF data corresponds to the error in the FITACF velocity determination. The horizontal bar for the DMSP drift is the standard deviation. The dashed line indicates where perfect agreement between the data would occur. For positive DMSP drifts (eastward ion motion), one can see that all points but one are located below the line of perfect agreement, and the departure increases for stronger ion drifts.

For negative DMSP drifts (westward ion motion), there are two sorts of points. Several points (circled in Figure 3.3) are located near the line of agreement at speeds higher than the expected ion acoustic speed. However, for the majority of the points, the

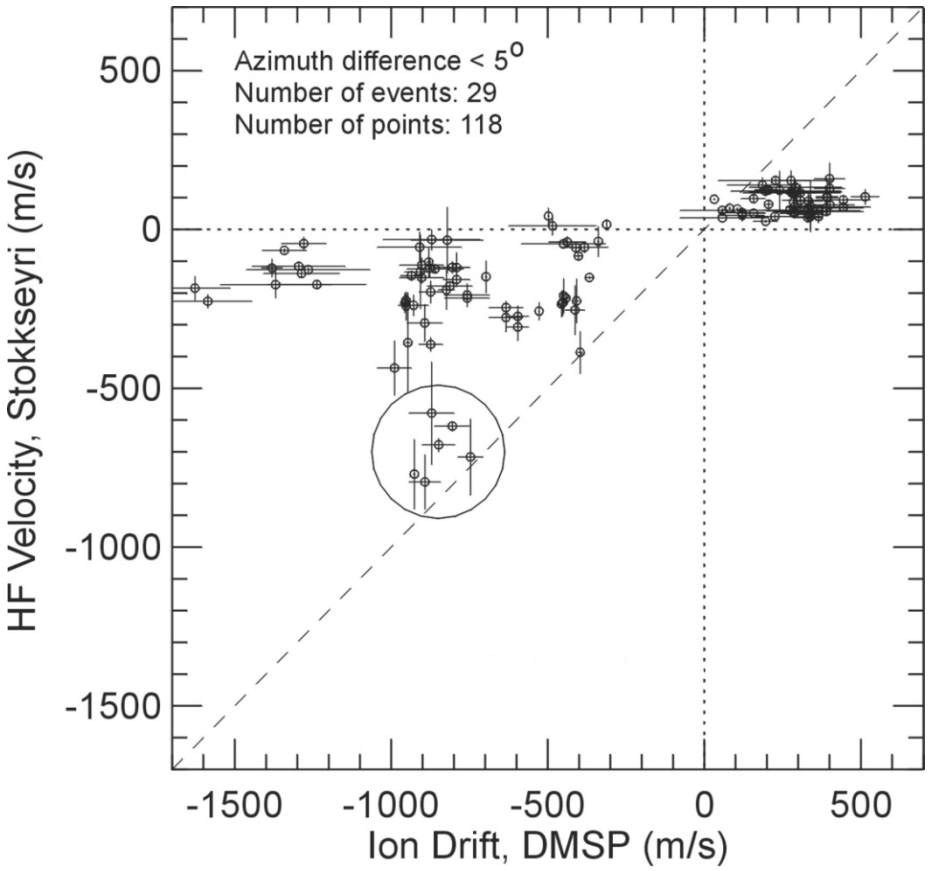

Figure 3.3: The line-of-sight Stokkseyri velocity versus DMSP ion drift when the deviation between the radar and satellite directions of measurements were less than 5º and the differences in time were less than 2 min. Radar data for the circled DMSP measurements corresponded to the radar cells just at the edge of the echo band, either at short or far ranges (*Koustov et al.*, 2005).

Stokkseyri velocity magnitude is well below the DMSP drift magnitude. This is similar to the result for the positive DMSP drifts. The velocity inconsistency increases as the ion drift magnitude increases. For example, for DMSP drifts of ~ 400 m/s, the velocity ratio $R = V_{HF} / V_{DMSP}$ is ~ 0.3 while for drifts of ~ 1300 m/s it is ~ 0.1 and the overall mean ratio is around 0.3. If one were to describe the Stokkseyri-DMSP velocity relationship by a straight line, the slope of the line (not shown) would be 0.2 and the intercept is zero. Note that for all DMSP values, there was only one point for which the ion drift was smaller than the Stokkseyri velocity. As mentioned, the data presented in Figure 3.3 satisfy quite a stringent requirement on the alignment between the satellite and radar directions of measurements. Analysis of the available data showed that with an increase in the azimuth difference, more points appear with either reasonable agreement

or low radar velocities. In addition, there are a couple of points for which the radar velocity is somewhat larger that the DMSP velocity, but the number of these points is insignificant. For example, for 15º azimuth difference, 2% of the points had stronger radar velocities.

3.4 Summary of findings

In Section 3.3 we compared directly the velocity of E-region Stokkseyri HF echoes and the **E** x **B** plasma velocity component along the radar beam as measured onboard DMSP satellites and showed that;

1. For large **E** x **B** drifts of greater than 700 m/s, the velocity of E-region echoes is typically smaller than the electron drift component along the radar beam by a factor of two to three. The effect is more pronounced at large drifts of more than 1000 to 1300 m/s. The peak observed HF radar velocities are less than 500 m/s in magnitude and are often less than 300 m/s. An HF radar velocity of 500 m/s is larger than the nominal ion-acoustic speed at 110 km (400 m/s) but smaller than the enhanced ion-acoustic speeds at 110 km for large electron drifts that were in effect for the events considered.
2. At **E** x **B** drifts along the radar beam below 300 m/s, the velocity of E-region echoes is somewhat smaller than **E** x **B**, but not significantly. If one considers the effect of **E** x **B** velocity reduction with height (11 – 12 %; *St.-Maurice*, personal communication, 2006), then the velocity of E-region echoes is closer to the **E** x **B** drift component and might be so for some points.
3. The overall average ratio $R = V_{HF} / V_{DMSP}$ is 0.3 ± 0.1.
4. Because only one component of the **E** x **B** velocity was available from DMSP observations, one can only hypothesize that simultaneous detection of low-velocity echoes corresponds to observations at large flow angles outside the FB instability cone. Another alternative is to be inside the FB instability cone but at small **E** x **B** drifts. For large **E** x **B** drifts, it is very likely that the comparison was done for observations inside the FB instability cone.

CHAPTER 4

HIGH-VELOCITY E-REGION HF ECHOES UNDER STRONGLY DRIVEN ELECTROJET CONDITIONS

In this Chapter, the investigation of the relationship between the velocity of E-region echoes and the **E** x **B** plasma drift is continued by focusing on two aspects, the velocity dependence on the **E** x **B** magnitude and the **E** x **B** direction. The latter is known as the flow angle variation. This study is an extension of the work reported in Chapter 3.

Only conditions with **E** x **B** drifts above 1000 m/s are considered, when the Farley-Buneman instability is operational. This is an interesting and intriguing range of plasma drifts; we showed in Chapter 3 that for this condition, the velocity of E-region echoes could be significantly smaller than the **E** x **B** component along the radar beam and perhaps even smaller than the ion-acoustic speed C_s.

Because there are no direct measurements of the **E** x **B** magnitude and direction within any SuperDARN radar FoV, as was mentioned earlier, a method was developed for inferring the **E** x **B** vector from the analysis of F-region echoes co-existing with E-region echoes, though at somewhat larger ranges. Relying on the fact that in the afternoon/evening sector of the auroral zone, the flows are homogeneous and mostly along the magnetic L-shell direction, so that the L-shell angle is a good proxy for the real flow angle. Independent verification of this assumption has been done for some events for which DMSP measurements were available.

Our approach is similar to the one used by *Makarevitch et al.* (2004), who considered data from the Hankasalmi SuperDARN radar and selected events for which both E-region and F-region echoes co-existed. Since the F-region echo velocity reflects the **E** x **B** drift, the flow direction was estimated by using the L-shell angle as a proxy and by fitting the F-region velocities across the field of view to a shifted cosine function of the form $V_{ph} = V_o\cos(\phi-\phi_o)$. The difference between our work and that of *Makarevitch et*

al. (2004) is that we consider data from the Stokkseyri SuperDARN radar that monitors echoes along the flow (small flow angles), while *Makarevitch et al.* (2004) considered Hankasalmi SuperDARN data obtained by observing almost perpendicular to the flow. As discussed in Chapter 2, the physics involved in the formation of irregularities in these two directions might be quite different and previous observations do show significant differences (i.e., *Makarevitch et al.*, 2004).

4.1 Event selection

Several events with stable and long-lived concurrent short-range (< 700 km, gates 3 – 10, presumably E region) and far-range (> 700 km but less than ~ 1500 km, gates 11 – 40, F region) HF echo bands, observed in the afternoon sector by the Stokkseyri SuperDARN HF radar. For this radar, the low numbered beams (0 – 2) are oriented close to the L-shell direction.

For the event selection, periods were sought with two adjacent, temporally stable echo bands, such that the far range echoes had a high velocity of approximately 1000 m/s and echoes at short ranges had a lower velocity, so that the distinction between the bands was obvious, as illustrated in Figure 4.1 for 1 November 2001. This event has a band of low-velocity echoes extending across range gates 0 – 14. These are assumed to be E-region echoes. Gates 11 – 14 fall outside of our assumption of the E-region band, but the backscatter power and Doppler velocity maxima do occur within the range gates 3 – 10. Therefore, we contend that the echoes are still coming from the E region, even in gates 11 – 14. For this event, the concurrent F-region echo band occurred at range gates 15 – 30. We believe these echoes are from the F region since they are at ranges above the radio horizon for the E region, are of significantly larger velocity and constitute a separate band visible in the backscatter power. The other criterion was that the far-range echoes occupy as many beams of the radar as possible. This criterion was not easy to satisfy, as quite often these echoes existed in limited number of beams, contrary to the E-region echoes. In addition, ideally, the velocity of the far-range echoes should be observed to change with the flow angle, so that one can anticipate a uniform electric field in the ionosphere.

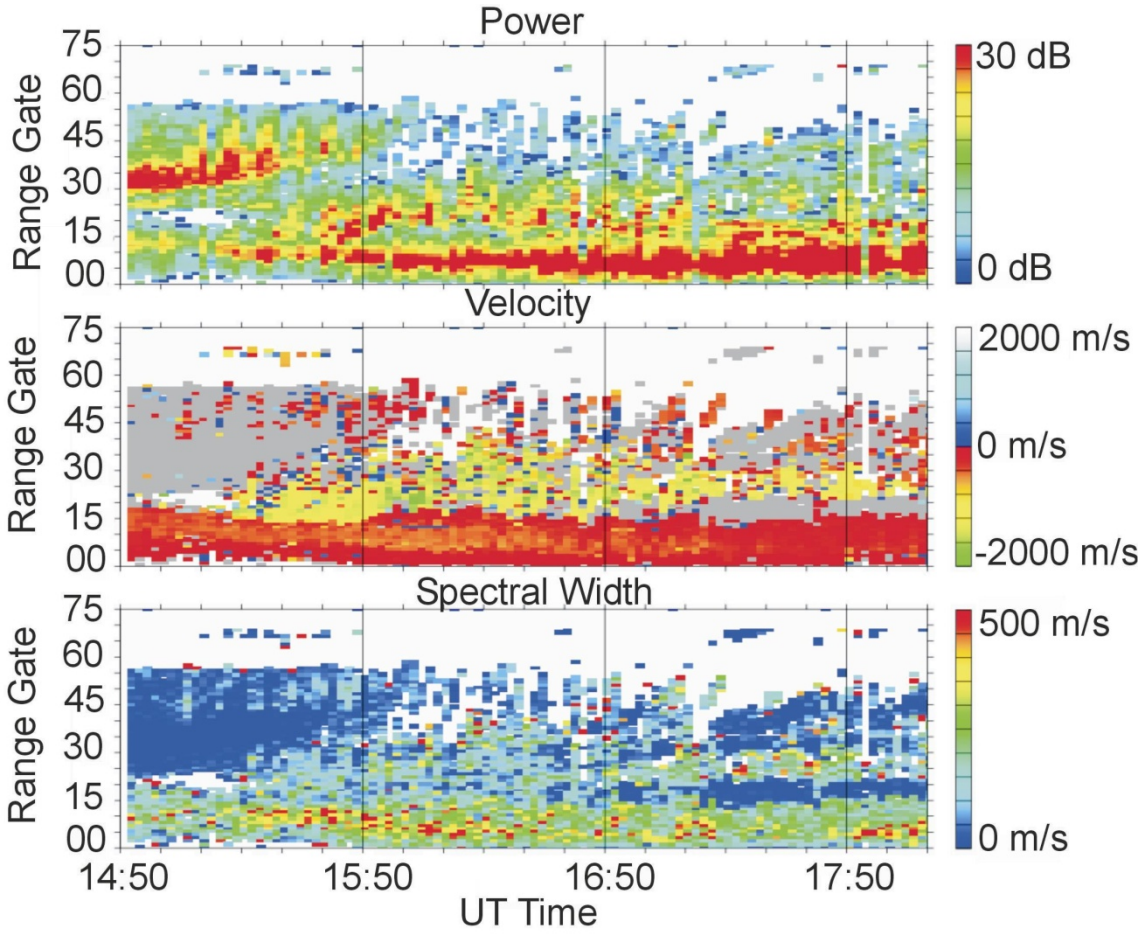

Figure 4.1: A standard SuperDARN data plot for beam 1 from Stokkseyri. Shown are power, velocity and spectral width of echoes versus time at various ranges for the event of 1 November 2001.

Forty-one events, each of two to three hours in duration, with similar characteristics as that of 1 November 2001, were identified for this study (see Appendix A). The convection maps (obtained through the standard Map Potential method (*Ruohoniemi and Baker*, 1998)) for each event were studied to ensure the convection pattern maintained a roughly consistent L-shell aligned flow in the region of interest. In this Chapter, we concentrate on one event, 1 November 2001. We should note right from the beginning that not all selected events demonstrated the features that will be discussed in this Chapter, but four events that do were selected for investigation. A number of other events exhibited much smaller velocities and one of these will be discussed in Chapter 5. There were cases that were more complicated where both high and low-velocity echoes were observed.

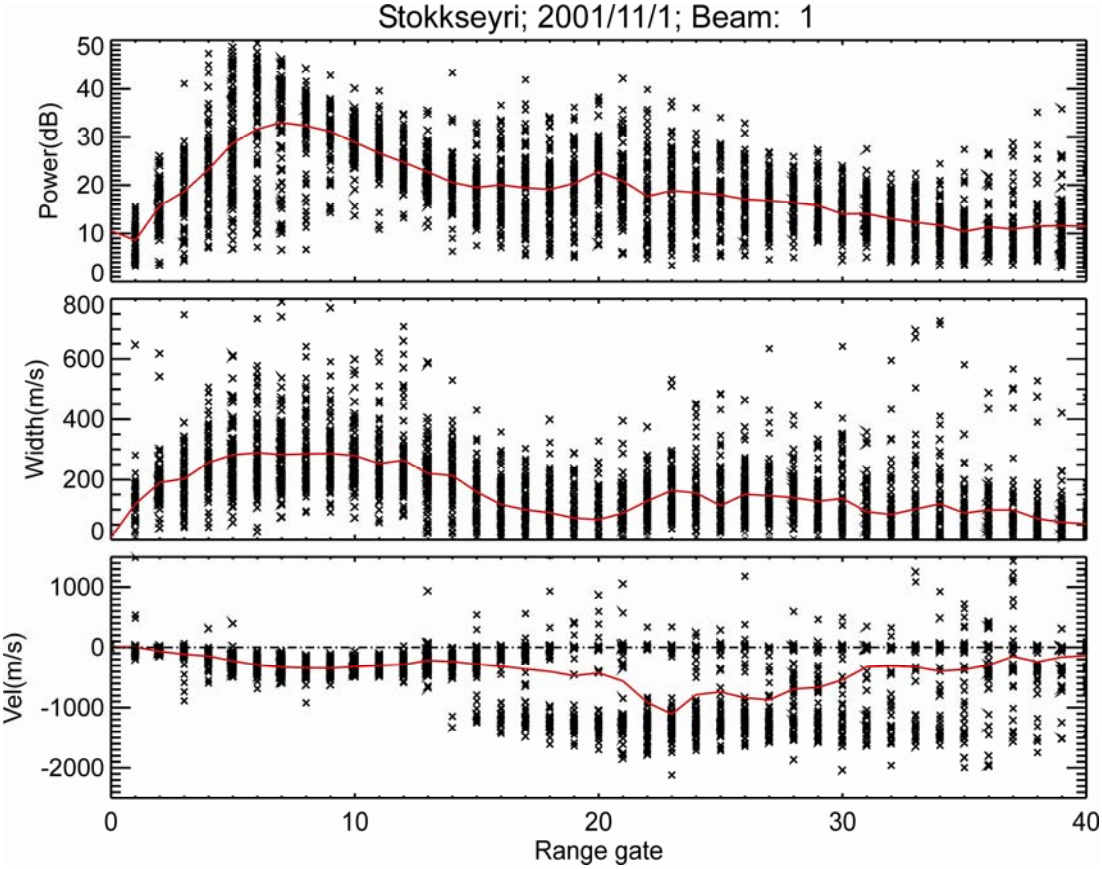

Figure 4.2: Echo power, spectral width and velocity recorded by the Stokkseyri radar for the entire event interval of 1 November 2001 in range gates 0 – 40. The red curve represent the average value of respective parameter at various range gates.

4.2 Analysis of one beam: E-region velocity along the flow and the E x B magnitude

First, the relationship between the E-region velocity and the **E** x **B** magnitude roughly along the electrojet direction was investigated. To achieve this, a simplified approach was considered; namely, data from Stokkseyri beam 1 was selected and compare the velocities at various ranges. This approach is illustrated by considering the data collected in beam 1 on 1 November 2001 (Figure 4.1).

In Figure 4.2, data for the echo power, velocity and spectral width are shown in Figure 4.1 but for range gates 0 – 40. The red curve traces the average value of the respective parameter for each gate. One can see that strongest echoes of 30 – 40 dB were received in range gates 6 – 8 and the echo power was gradually decreasing with range gate, all the way down to ~ 10 dB. The middle panel shows that strongest echoes were

also the broadest, 200 – 300 m/s at low range gates versus 100 – 200 m/s at the far range gates. The echo velocity, presented at the bottom panel, clearly demonstrates that while the velocity at the far range gates is up to 1000 m/s, at small range gates it is only 200 – 500 m/s. The velocity data in range gates 15 – 20 was is some places low, while at the other places it was high (see Figure 4.1. This is probably an indication that in these range gates, the echoes were coming from the E region at one time and from the F region at another. It means that the red curve does not characterize the velocity in these range gates. Velocities in range gates > 18 were remarkably stable at a level of 1000 – 1200 m/s. One can also notice near-zero velocity echoes in large gates, which are ground scatter signals.

The observed echo power variation (Figure 4.2) with range is as expected (*Makarevitch et al*., 2002a), as the E-region echoes are highly aspect sensitive. Range gates 6 – 8 correspond to a condition with minimum, perhaps zero, aspect angle observations. The velocity of the E-region echoes also maximizes in range gates 6 – 8 though not as obvious as in the echo power. We relate the existence of this maximum to the velocity aspect angle attenuation at ranges away from the maximum for the echo power and velocity, the effect is known for both VHF and HF echoes (*Fejer and Kelley*, 1980; Chapter 2, Section 2.2.5). In this study, to estimate the **E** x **B** magnitude, we find the maximum velocity in range gates 11 – 40 (F-region echo ranges). To include as many points as possible without including potential E-region echoes, this value is then averaged over all range gates whose velocity is within 40 % of the peak value. This provided an estimate of the mean **E** x **B** velocity in the F region along one radar beam. Criteria for echo rejection was spectral width above 800 m/s, backscatter power less than 3 dB and velocity error greater than 300 m/s to include as many points as possible but still have a rejection threshold of some relevance. To exclude ground scatter we also do not consider echoes with velocities less than 30 m/s and spectral widths less than 30 m/s.

As far as E-region velocity is concerned, to obtain an estimate of the velocity least affected by the aspect angle effect, the average velocity in three radar cells (among gates 3 – 10) corresponding to the ranges with the maximum echo power at short ranges was considered. Specifically, we find the range with the maximum echo power in the selected

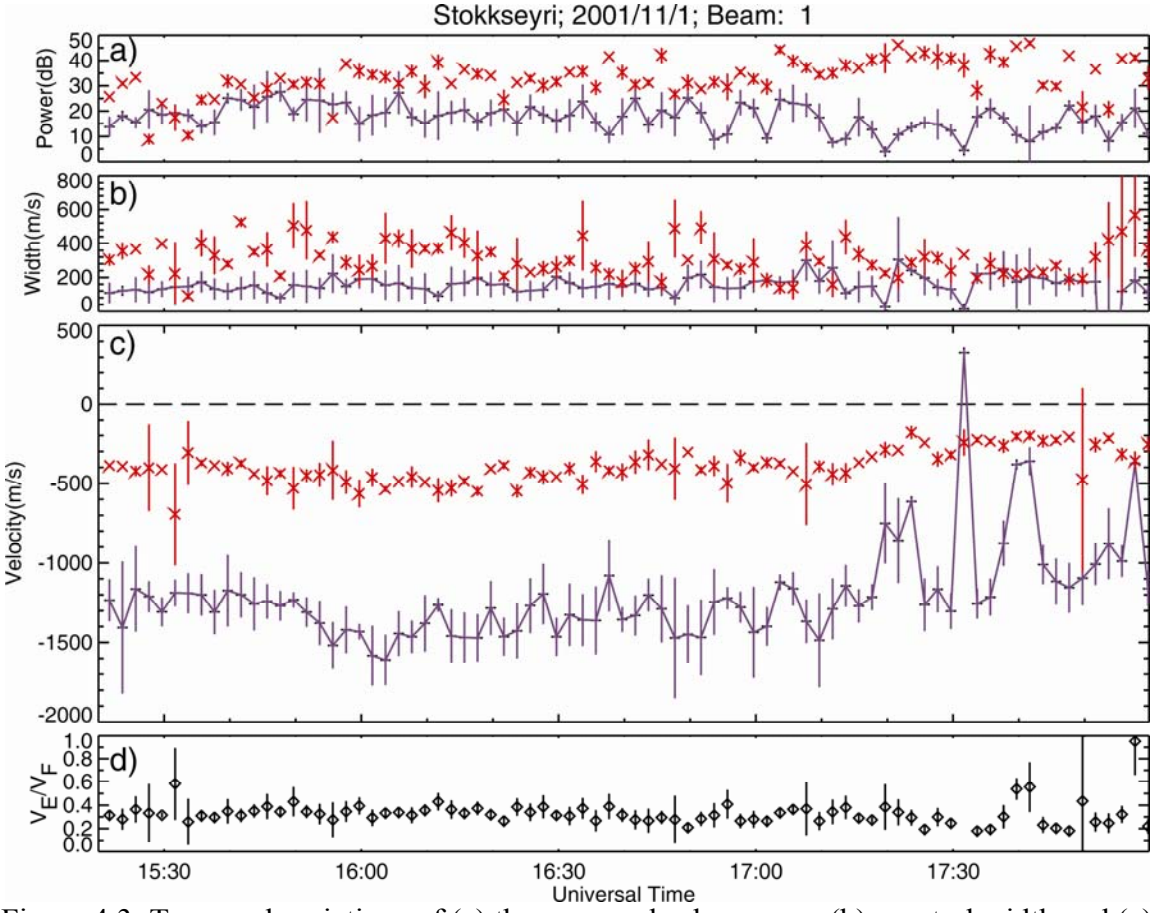

Figure 4.3: Temporal variations of (a) the averaged echo power, (b) spectral width and (c) velocity for the E-region and F-region echoes. Panel (d) shows the velocity ratio $R = V_E/V_F$. Red crosses represent the E-region parameters, plus signs connected by the lines represent F-region parameters, the diamonds are the ratio of the E-region velocity to the F-region velocity, and the vertical bars represent the errors.

beam, and then average this velocity with the velocity in the immediately adjacent range gates.

Figure 4.3 presents a time series plot of the (a) averaged echo power, (b) spectral width and (c) velocity for the event of 1 November 2001 (Figure 4.1). The E-region echoes were stronger and broader than the F-region echoes, panels (a) and (b) and the E-region velocity magnitudes were near the ion-acoustic speed while the F-region velocity (**E** x **B** component) was very large (~ 1300 m/s) and changing more significantly. One can notice the general trend of the E-region velocity to decrease as the F-region velocity decreases during the second half of the event. The magnitude of the E-region velocity (300 – 500 m/s) is expected from the non-linear theories of electrojet irregularities as the

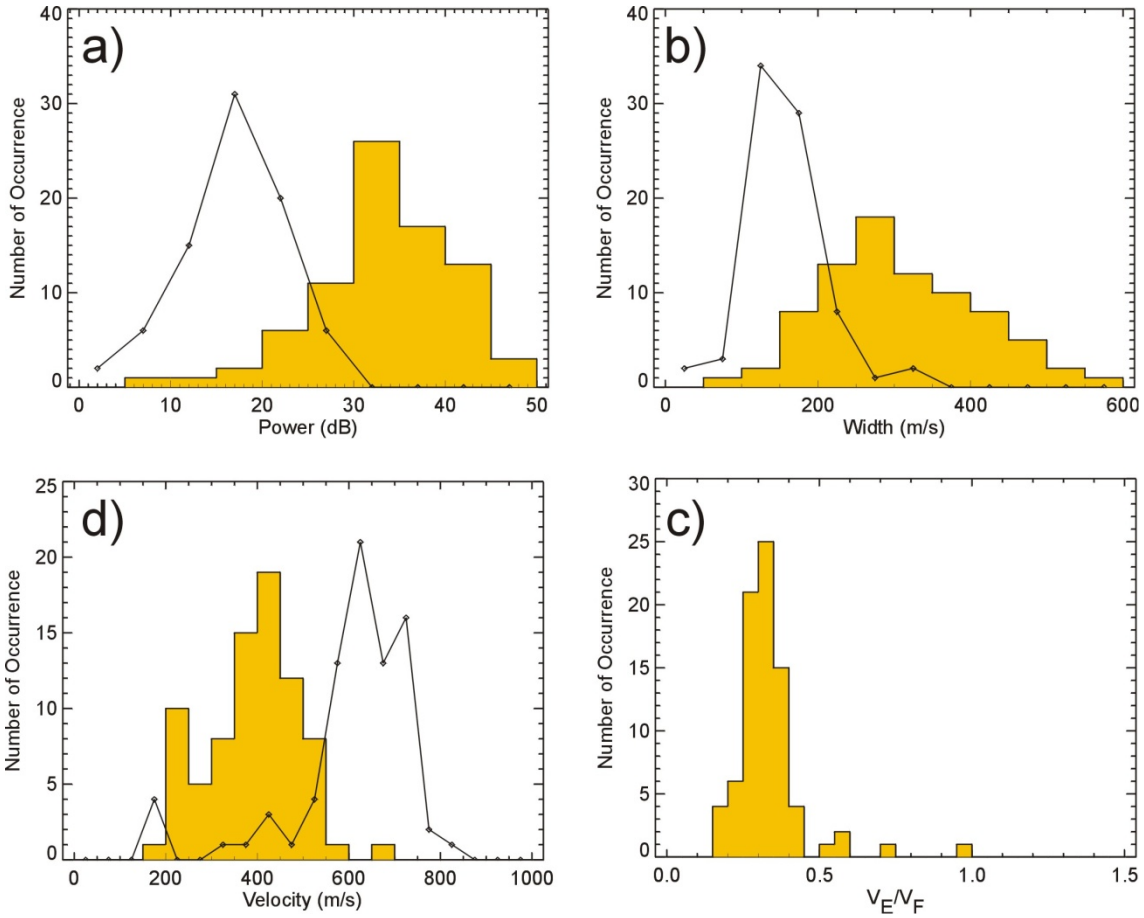

Figure 4.4: Histogram distributions for the parameters presented in Figure 4.3. F-region velocities (lines) were scaled down by a factor of 2 in panel (d).

velocity can saturate near the ion-acoustic speed (nominal value is ~ 400 m/s) for observations roughly along the electrojet direction (Chapter 2). The bottom panel (d) in Figure 4.3 shows temporal variations of the velocity ratio, $R = V_E/V_F$. Clearly, R holds steady at a value around 0.3, which is consistent with the observations presented in Chapter 3.

Figure 4.4 presents the data of Figure 4.3 in the form of histogram distributions. Panels (a) and (b) show that the E-region echoes are 5 – 7 dB stronger and 100 – 120 m/s broader than the F-region echoes. Panel (c) supports the conclusion of visual analysis of Figure 4.2 that the velocities in both echo bands were stable, as the distributions are narrow. Panel (d) gives statistics for the velocity ratio $R = V_E/V_F$, which is the target of this investigation. For this event, the ratio is stable and seems to be independent of the **E** x **B** magnitude.

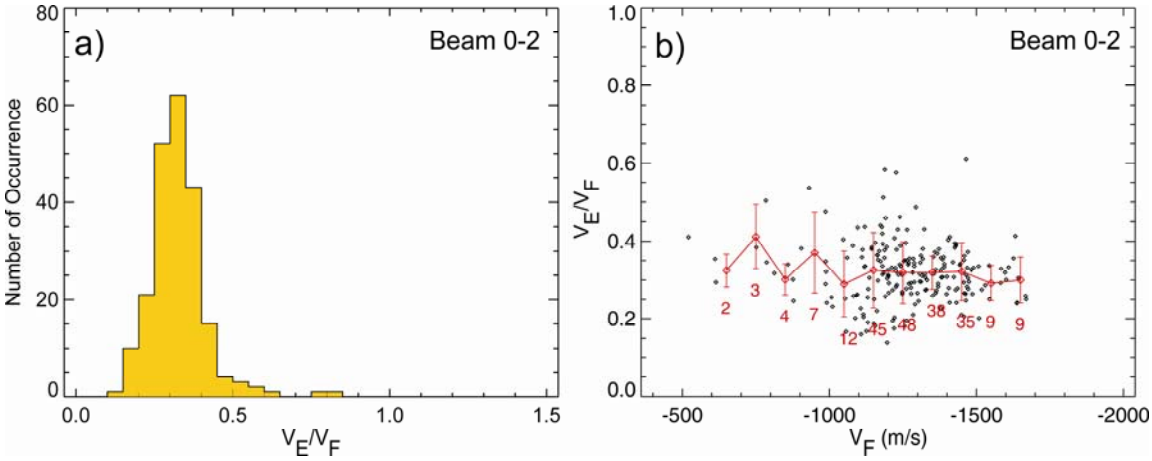

Figure 4.5: Velocity ratio R in beams 0, 1 and 2 for the event of 1 November 2001: (a) Histogram distribution. (b) Scatter plot of R for various **E** x **B** drifts. Averaged value of R is shown as the red line, with the number of values averaged shown.

Finally, note that the data from beam 1 has only been considered for illustrative purposes. We also considered data in adjacent beams 0 and 2 and did not find discernible differences whether one or three beams are considered. Figure 4.5 shows the histogram distribution for R and its dependence on $\frac{E}{B}$. Here data from beams 0 and 2 were added to the data collected in beam 1. Figure 4.5 shows that typical value of R for the considered event is 0.3 with no discernable trend in R.

4.3 Analysis of all beams: Velocity variation with L-shell (flow) angle

The analysis presented in the previous section can be criticized in three ways. Firstly, the flow angles are slightly different at the far and short ranges of the Stokkseyri FoV (Figure 2.6). Secondly, the velocity of the **E** x **B** drift can be slightly larger as the flow might be off the L-shell direction the assumed direction of the electron flow. Finally, the E-region echoes might not have been observed exactly along the **E** x **B** direction. In this Section, we attempt to address these points by considering data in all Stokkseyri beams. Such investigation has its own merit, as the characteristics of E-region irregularities do depend on the flow angle (*Fejer and Kelley*, 1980; *Schlegel*, 1996; *Sahr and Fejer*, 1996). In this section, as a proxy for the flow angle, we select the L-shell angle ϕ, which is counted counter-clockwise from the line of constant magnetic latitude

to the SuperDARN line-of-sight direction. Every range gate within the SuperDARN field of view then has its own unique L-shell angle.

4.3.1 Estimate of the flow angle variation for the echo power, velocity and spectral width

To examine the HF echo parameters variation with the flow angle, the echo power, velocity and spectral width for the entire event are presented in Figure 4.6 for both the E-region and F-region echoes. The data collected over the events are plotted in the form of scatter plots. Here overlaid are binned averages for all parameter in the entire range of L-shell angles. For the velocity variation with the flow angle, a cosine fit was applied. Errors in the parameters of the obtained equations (panels (c) and (d)) are not shown. They are less than ± 15º in the phase and ± 150 m/s and ± 300 m/s for the E- and F-region peak velocities, respectively. Both error values were determined from the standard error between the data and the fitted cosine curves.

The power of the F-region echoes does not change much with ϕ, and there is some change for the E-region case. The echoes are ~ 5 dB stronger at large flow angles, although this might be because echoes at these directions were received at closer ranges on average. The velocity of the F-region echoes changes drastically from ~ 1500 m/s at $\phi = 20º$ to ~ 0 m/s at $\phi = 70º$. Note that averaging is somewhat affected by ground scatter echoes seen at large ϕ. In Figures 4.6c and d, a cosine fit is made to the averaged values of the velocity (see Appendix B for the program used to perform this fit), and the results are presented on the diagram by dashed lines. The cosine dependence is reasonable for both the E and F-region echoes. This looks very reasonable for the F-region case, although the E-region case requires some justification, and we will be looking at this variation in detail later. One should notice the significant differences between the fitted maximum F and E-region velocities, 1330 m/s versus 390 m/s with a velocity ratio of ~ 0.3, which is in full agreement with the results of the one beam analysis, Figure 4.5. Another interesting feature is that the velocity maxima in the E and F regions are achieved at slightly different ϕ angles (-7º versus 18º, respectively). We will investigate this feature later. The spectral width, Figures 4.6e and f, shows some variation with ϕ.

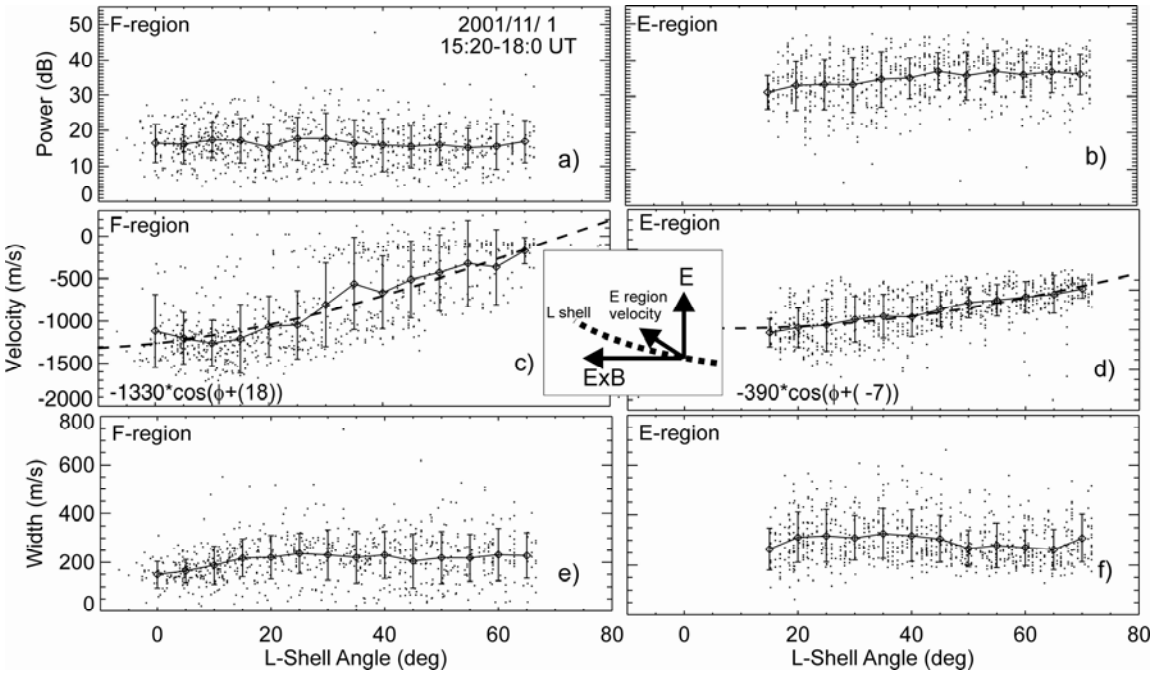

Figure 4.6: Scatter plot of measured echo power, velocity and spectral width for F-region and E-region echoes versus the L-shell angle. Data trends are illustrated by averaging (solid lines) and by fitting to a cosine function (dashed lines). The insert between panels (c) and (d) shows the directions of the E-region velocity and the **E** x **B** drift with respect to the electric field and L-shell based on the fitted results.

The reason for this is unclear; it seems that the echoes are broadest at intermediate ϕ. This result is peculiar for the E-region echoes, as one would generally expect narrow widths at small ϕ (*Makarevitch et al.*, 2004).

The data presented in Figure 4.6 indicate only the general trends. To investigate the velocity variation with flow angle, we have to consider the data from individual scans.

4.3.2 Analysis of individual scan data

Figure 4.7a gives an example of a Stokkseyri scan for which the band of E-region echoes, red colour at short ranges, is broad and extends across the entire field of view and the band of F-region echoes, yellow and green colour, is also quite extended, covering most of the field of view.

Figure 4.7b presents the velocity data in a more readable form. Here, red crosses show the velocities of the E-region band (gates 3 – 10) and diamonds show the velocities

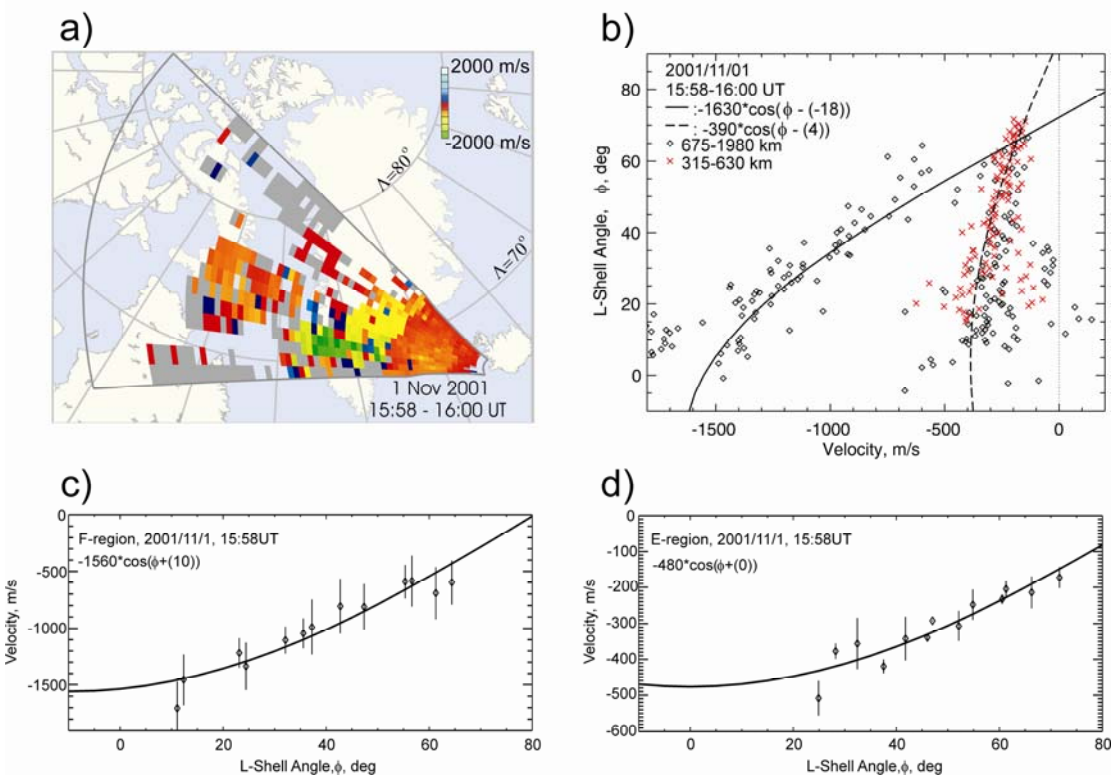

Figure 4.7: (a) Stokkseyri SuperDARN radar velocity map obtained on 1 November 2001 at 15:58:00 – 15:59:48 UT. The magnetic parallels of 70º and 80º are shown by grey line to simplify estimates of the L-shell angle ϕ. (b) Cosine fit results for the fit to SuperDARN velocities for 1 November 2001 at 15:58 – 16:00 UT (diamonds greater than -500 m/s and less than 40º not considered for F-region fit). (c) Cosine fit results for the fit to the peak line-of-sight F-region velocity estimates for 1 November 2001 at 15:58 – 16:00 UT. (d) Cosine fit results for the fit to the peak line-of-sight E-region velocity estimates for 1 November 2001 at 15:58 – 16:00 UT. Vertical lines in panels (c) and (d) represent the error in the averaged velocity.

in F-region band (gates > 10). Two sets of points are recognizable; one set is stretching to high velocities all the way up to 1600 m/s and the other one is a region of points sitting near velocities of 300 – 500 m/s. In the second band, there are a few points that are classified as F-region scatter; these were received in gates ~ 11 – 15. We believe that these are still E-region measurements, and the fact that they apparently belong to the cloud of E-region measurements supports this suggestion.

To characterize these two sets, we fit the velocities with a cosine function of the form $V_{los} = V_o\cos(\phi-\phi_o)$, where the V_o is the peak line-of-sight velocity and ϕ_o is the L shell angle of the velocity maximum. The major problem in accomplishing this task is

that there is a significant scatter in the data, especially in the low-velocity band. Another problem is an overlap of velocities: at small angles, some far-range velocities fall into the second group, which we associate with the E-region echoes. In addition, at angles of ~ 60º – 70º, the data for the two velocity-sets overlap.

To overcome the above difficulties, two different procedures were attempted. First, it was decided to apply a cosine fit straight to the velocity versus L-shell angle scatter plot, such as the one shown in Figure 4.7b; it resulted in dependencies $V_{los} = -1600\cos(\phi+18º)$ and $V_{los} = -400\cos(\phi-4º)$ for the F- and E-region echoes, respectively, if we neglect the F-region velocities greater than -500 m/s and an L-shell angle less than 40º. However, the number of scans comparable in quality to the ones shown in Figures 4.7a and b is low for this event, and the situation is worse for other events in the database. For these reasons, it was decided to employ fitting after preliminary averaging of the data.

Figures 4.7c and d illustrate this approach. At first, data in each beam position were considered separately, and velocity estimate for the E and F-region echoes were done as described in Section 4.3.1. Specifically, for the E region, the range with the maximum echo power was found in the selected beam, and then averaged this velocity with the velocity in the adjacent range gates. This velocity was associated with the L-shell angle for the range gate of the power maximum. For the F-region echoes, the velocity maximum was found along the beam in range gates 11 – 40 and then this value was averaged over all other observed velocities whose magnitude was within 40 % of the peak within that beam. This velocity was associated with the L-shell angle for the range gate of the velocity maximum. Figures 4.7c and d show that the dependencies obtained this way are $V_{los} = -1560\cos(\phi+10º)$ and $V_{los} = -480\cos(\phi+0º)$ for the F and E-region echoes. Errors in the velocity magnitude and L-shell angle determination are of the same order as those in Figure 4.6, i.e., 150 m/s and 300 m/s for the E- and F-region velocities and 15º for the L-shell angle. Although the obtained parameters of the cosine function are different, the differences are not believed to be significant, and this second approach can be used. The fits performed in the second way gives closer agreement with the cloud of points than the first method of simple fitting to the clouds of points (Figure 4.7b). The

reason is that even a couple of points laying outside from the general trend affect the fit significantly and these outliers are less significant in the second approach.

The cosine function fit to the velocity data was done by using a Levenberg-Marquardt algorithm (*Press and Vetterling*, 1986), which provides a numerical solution to the problem of minimizing a non-linear function over the space of its parameters, in this case the peak velocity, V_o, and the phase shift, ϕ_o. The Levenberg-Marquardt algorithm is a combination of the Gauss-Newton algorithm, which performs a non-linear least squares fit without considering derivatives according to Newton's Method, and the method of gradient descent. The Levenberg-Marquardt algorithm does suffer from a tendency to converge slower than other fitting methods; however, it is more robust than the Gauss-Newton algorithm and will find a solution in many cases, even when starting far from the final minimum.

Another advantage of the second approach to fitting is that the entire process can be automated, as the need to selectively eliminate outlying data points that would negatively influence the fit is eliminated. The automated fitting procedure required that a peak line-of-sight velocity estimate was available in a minimum of eight beams and that the fitted result converged within 200 iterations to a tolerance of the relative decrease in the chi-squared value of the fit to be less than 10^{-7} for the fit procedure to return a result. Considerable trial and error determined that the fitted result be discarded from the data set if the standard error between the fitted cosine curve and the peak line-of-sight velocity estimates was greater than 300 m/s for the F-region fits and greater than 150 m/s for the E-region fits.

4.3.3 Velocity flow (L-shell) angle variation at HF and VHF

Ideally, individual velocity maps presented in the form of Figure 4.7b would allow one to assess, at least qualitatively, whether the velocity of E-region echoes can be described by the cosine function or by some other function. For the considered case, a description of the red crosses by the cosine function looks reasonable for both methods of fitting to the E-region data. For other Stokkseyri scans, it was not as easy, as the data scatter was sometimes considerable.

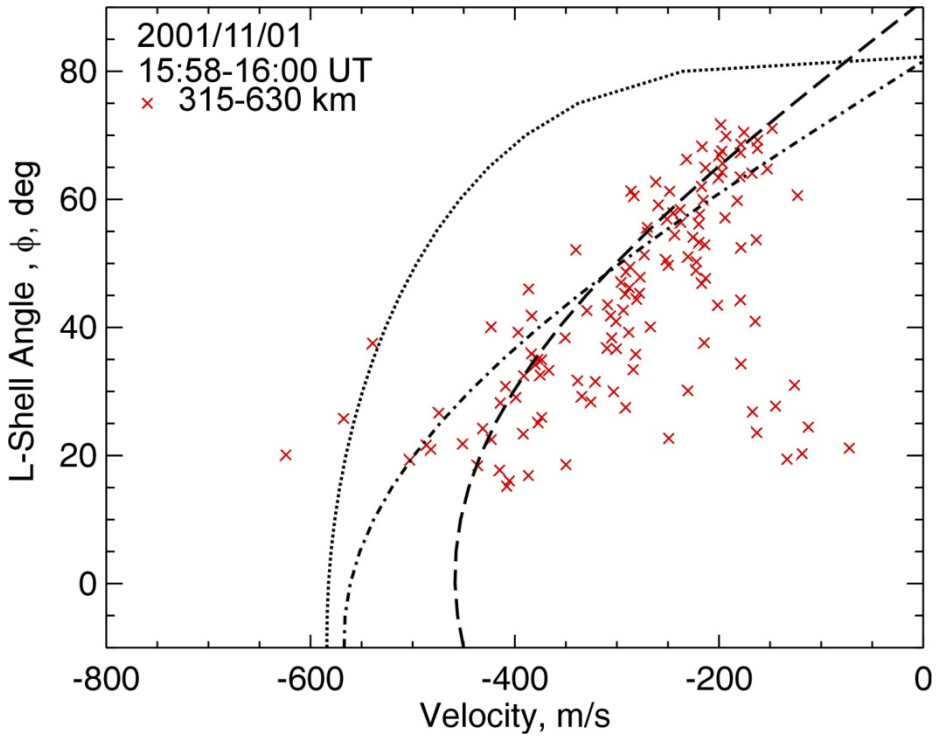

Figure 4.8: Cosine fit line for the E-region velocities presented in Fig. 4.7 (dashed line), velocity variation predicted by *Bahcivan et al*. (2005) (dash-dotted line) and empirical dependence given by *Nielsen et al.* (2002) for VHF (dotted line).

Our choice to characterize the velocity of E-region echoes by the cosine function is arbitrary, although it can be justified by recent results by *Bahcivan et al.* (2005) at VHF. *Uspensky et al*. (2001) presented hints supporting the same cosine variation at HF and Nielsen *et al*. (2002) also used a cosine function, but stated that it is only applicable to observations at large flow angles. At small angle, the variation was more complicated, although the cosine function was still involved.

Assuming the velocity of HF echoes can be described by a cosine function, one can see whether the data presented agree with the findings at VHF. To accomplish this task, we compare the E-region data to the predictions of *Bahcivan et al*. (2005) and *Nielsen et al*. (2002) in Figure 4.8. In this diagram, we also used estimates of C_s based on recent EISCAT data (*Koustov*, personal communication, 2007). Errors in the L-shell angle and the velocity are not shown in Figure 4.8, they are ± 2º and ± 150 m/s respectively.

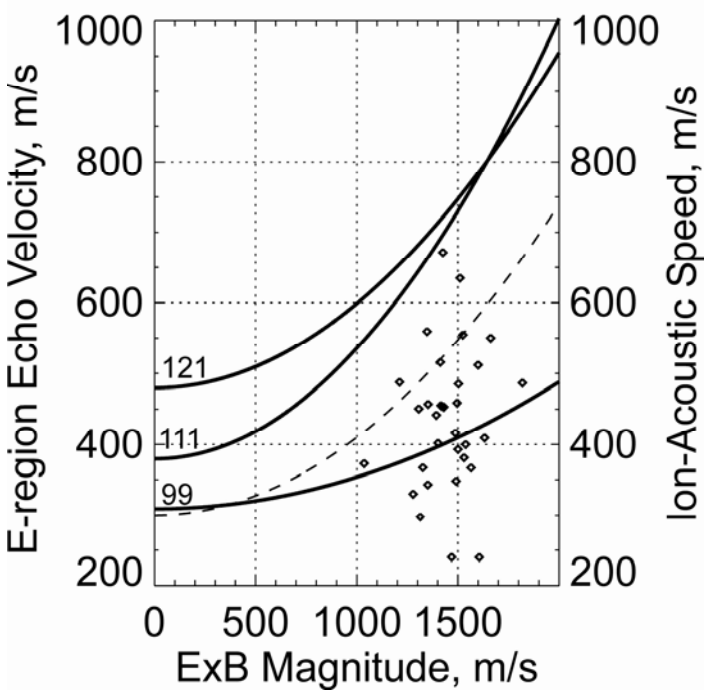

Figure 4.9: The maximum E-region velocity (derived from the fitting procedure) for various **E** x **B** magnitudes for 1 November 2001 is denoted by the diamonds and using the left hand vertical axis. The variation of the ion-acoustic velocity C_s at three heights indicated next to the left hand axis versus **E** x **B** is denoted by the solid lines and the experimental curve for VHF radar velocity by *Nielsen and Schlegel* (1985) is denoted by the dashed line, both using the right hand vertical axis.

At flow angles for which the data were available, the velocity is reasonably described by a $C_s \cos\theta$ dependence. The coefficient of proportionality of ~ 490 m/s is somewhat smaller than the expected value of $C_s \approx 570$ m/s (dash-dot line). The relationship by *Nielsen et al*. (2002) does not work well; the dotted line is not comparable to the experimental data and the curve fitted to the data. One might think that the data supports the hypothesis by *Bahcivan et al*. (2005), as the obtained velocity maximum of 490 m/s is close to the ion-acoustic speed at electrojet heights. Though it is tempting to state this right away, recall that C_s is a function of the **E** x **B** magnitude (Chapter 2) and it means that a more thorough comparison needs to be done.

We selected all the scans that passed the criteria for acceptance for the event of 1 November 2001 and found the maximum E-region velocities. Figure 4.9 presents all points in terms of the measured **E** x **B** drift along the horizontal axis. One can see that the number of points is limited, and their scatter is too large to make any conclusion about

the trend. We attempted to include one additional event, 3 March 2001, and the situation did not improve, even though we had ~200 points to consider. Unfortunately, we conclude that the data trend is indiscernible and more stable data are needed to resolve this aspect of the measurements. In Figure 4.9, we also show the C_s variation with **E** x **B** as inferred from EISCAT data at three heights (bottom, 99 km, middle, 111 km, and top, 121 km, of the electrojet layer) as well as the VHF velocity variation discussed in terms of C_s by *Nielsen and Schlegel* (1985). One conclusion can be made from this diagram: the HF velocity is smaller than what is expected assuming the echoes are coming from the central heights of the electrojet and is comparable to C_s if the HF echoes were all received from the bottom part of the electrojet layer. One may state that the data does not contradict the hypothesis by *Bahcivan et al*. (2005) if the HF echoes are systematically coming from the bottom of the electrojet layer. Whether the latter is correct needs further investigation.

4.3.4 Direction of the HF velocity maximum and the E x B direction

As we have already mentioned in previous sections, the L-shell angle of the F-region and E-region velocity maxima do not coincide. To investigate this further, we processed 184 Stokkseyri scans with echo coverage similar to the case of Figure 4.7. These scans were obtained for four events within our data set: 1 November 2001 at 15:16 – 17:18 UT, 17 November 2001 at 17:06 – 18:30 UT, 15 January 2002 at 18:54 – 21:30 UT and 3 March 2002 at 16:58 – 19:12 UT.

Figure 4.10a gives a histogram distribution of the differences between the azimuths of the F-region and E-region maximum velocity. The data were collected in the afternoon/evening sector of the high-latitude ionosphere with a northward oriented electric field. The bell shaped diagram suggests that there is a statistical mean value of the shift of approximately 20º, with the F-region velocities having smaller azimuth. This implies that the E-region velocity maximum is generally shifted by ~20º towards the direction of the electric field. We also examined how the above shift changes with **E** x **B** magnitude (Figure 4.10b). The shift is more pronounced at larger **E** x **B**; the linear fit to the obtained points gives a change in the L-shell angle as described by

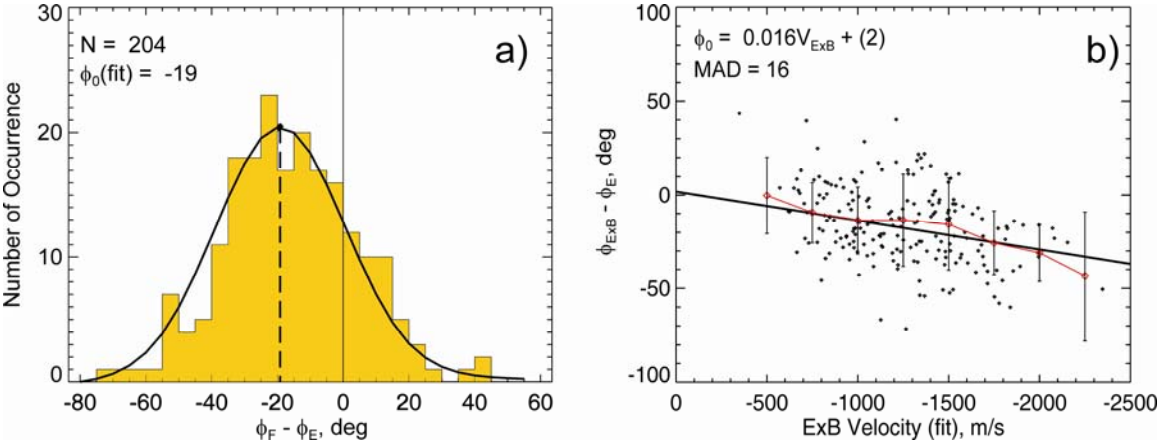

Figure 4.10: (a) Occurrence histogram of the L-shell angle difference between the peak E-region velocity and the **E** x **B** velocity. (b) The difference between the direction of maximum E-region velocity and the **E** x **B** direction versus **E** x **B** magnitude. Averaged values and their respective standard deviation are shown in red.

$\Delta\phi_o = 0.016(\pm 0.015)\frac{E}{B} - 2(\pm 16)$ and the averaged trends of the data (shown in red, Figure 4.10b) agree with the fitted result. The errors for the equation were obtained from the error in the least absolute deviation fitting method used.

4.4 DMSP validation of E x B vector determination from the Stokkseyri F-region velocity observations

The results reported in this section are based on the assumption that the flow was predominantly L-shell aligned. As we mentioned in Section 4.1, for several events of the selected data set, DMSP measurements of the ion drift in the F region were available. Such joint measurements allowed us to verify the approach adopted in this study. Additionally, these data had implications of their own and they are the subject of additional investigation that is beyond the scope of this thesis. One example of a unique, concurrent DMSP-SuperDARN event was shown in Figure 3.1, and here we consider another example (Figure 4.11).

Figure 4.11a shows the Stokkseyri l-o-s velocity map at ~ 19:00 UT on 15 January 2002 and the ion **E** x **B** drift component measured in the direction across the DMSP F13 track footprint. The satellite crossed the Stokkseyri FoV covering both E and F-region

echo bands. The DMSP velocities were mapped down magnetic field lines to SuperDARN heights of 110 km, assuming no **E** x **B** reduction due to difference in the magnetic field and divergence of magnetic flux lines. The along track ion drifts from DMSP were also considered, but they were discarded due to their poor quality.

Coverage of both the E- and F-region echo bands were significant; this allowed for reasonable quality fits. Figure 4.11b shows the fits to the averaged peak Stokkseyri velocities for this event. The fit for the F-region echoes gives a peak value of ~ 1400 m/s and orientation of ~ 20º counter-clockwise from the L-shell direction while the DMSP cross-track ion drifts peaks at ~ 1300 m/s. In this case, the cross-track ion drifts are nearly parallel to the L-shell direction and the DMSP cross-track ion drifts agree well with the L-shell aligned component of the fitted peak **E** x **B** velocity. One may conclude that the obtained peak **E** x **B** velocity is consistent with the DMSP cross-track ion drifts, supporting our approach to evaluation of **E** x **B** velocities for this event.

Additionally, a portion of the DMSP track passed over the short-range echoes, presumably E-region echoes. In this area, the DMSP cross-track ion drifts are ~ 900 m/s whereas the SuperDARN line-of-sight velocities are ~ 200 m/s, which is also what the fitted E-region peak velocity is, albeit rotated 10º counter-clockwise from the L-shell aligned direction. This comparison supports our conclusions made in Chapter 3.

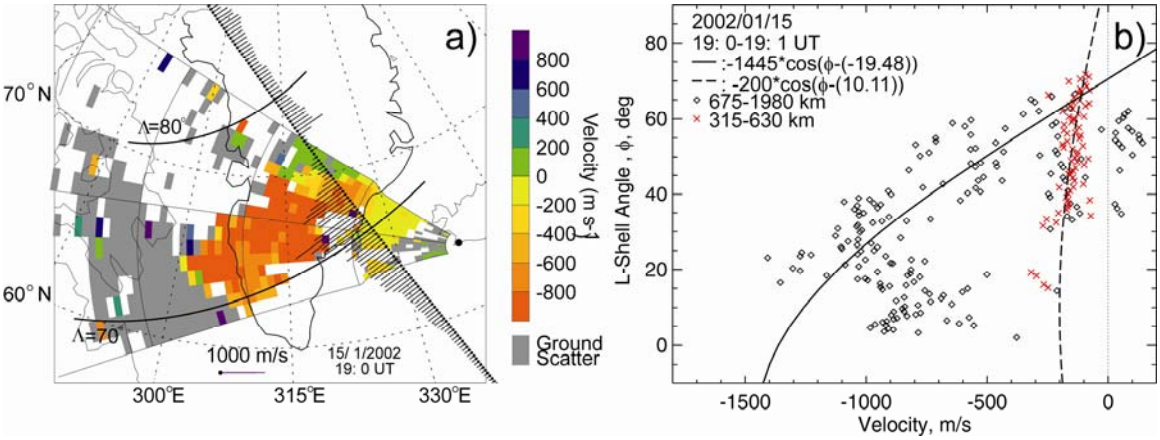

Figure 4.11: (a) Stokkseyri velocity map with DMSP footprints at 110 km (dots) and the ion **E** x **B** cross-truck velocities (vectors) observed by the DMSP radars in the event of 15 January 2002, 19:00 – 19:01 UT. (b) Cosine fit to the velocity maxima according to the second fitting method.

4.5 Summary of findings

In this Chapter, Stokkseyri HF radar data were considered to investigate the velocity of short-range echoes and to compare them to the velocity of far-range F-region echoes, which reflect the **E** x **B** drift of the ionospheric plasma. The focus was on the velocity ratio $R = V_E/V_F$ for observations roughly along the electrojet direction. An event with very large **E** x **B** drift (~ 1500 m/s) in the afternoon was studied in detail. Two approaches were employed:

1. A comparison for one (or three) beam(s) oriented roughly along the magnetic L-shell direction, the expected predominant direction of the **E** x **B** flows.
2. A consideration of the data collected in all beams to estimate the effective **E** x **B** vector from far-range echoes and an assessment of the E-region velocity in terms of the flow angle, **E** x **B** magnitude and ion-acoustic speed C_s.

Both approaches showed that the velocity of the E-region echoes was significantly smaller than the **E** x **B** electron drift in the ionosphere. Statistically, the mean velocity ratio R was found to be ~ 0.3 ± 0.1. The E-region velocities were found to be smaller than the expected ion-acoustic speeds of the plasma at the center of the electrojet (~ 110 km). This is in contrast with VHF echoes whose velocities are believed to be close to C_s at 110 km. The matching of the E-region velocity with the C_s magnitude multiplied by the cosine of the flow angle can only be achieved if one assumes that HF echoes are always coming from the heights below ~ 100 km. An attempt has been made to describe the E-region velocity variation with the azimuth (flow angle or L-shell angle) by assuming a cosine dependence on the angle. It was found that many individual scans can be described by such a function. The directions at which the maxima of the velocity were observed did not coincide with the direction of the **E** x **B**. Typically, for the westward electron drift in the afternoon sector E-region, the direction of the velocity maximum was closer to the northward direction (the electric field direction) by ~ 20º. This deviation was more pronounced at larger **E** x **B** drifts.

Finally, the validity of the **E** x **B** estimates from consideration of far-range Stokkseyri echoes were confirmed for one of the events for which concurrent ion drift data onboard a DMSP satellite were available.

CHAPTER 5

LOW-VELOCITY E-REGION HF ECHOES UNDER STRONGLY DRIVEN ELECTROJET CONDITIONS

In the selected database, events with small E-region velocities (100 –200 m/s) were found for F-region echo velocities in excess of 600 – 700 m/s. Since we expected that the echoes would have velocities closer to C_s, it was decided to investigate the properties of these low-velocity echoes in more detail in terms of their relationship to the **E** x **B** magnitude and direction. *Koustov and Gorin* (2007) has presented a preliminary report on these low velocity echoes.

5.1 Introduction to the low-velocity HF echoes

Once the ionospheric electric field exceeds ~ 35 mV/m, strong electron density irregularities at the meter scale are excited at auroral electrojet heights due to the Farley-Buneman (FB) plasma instability. The FB-related irregularities (Type 1 irregularities, Section 1.4.1) are preferentially observed along the direction of the **E** x **B** electron flow, and are identifiable by a relatively narrow spectrum VHF coherent echo and by a mean shift of the echo spectrum close to the ion-acoustic speed, C_s, at electrojet heights (~ 400 m/s). Type 1 irregularities are expected to occur at decameter wavelengths as well. A number of studies with HF radars seem to support this expectation (e.g., *Milan and Lester*, 1999; 2001), but some of the published data do not fit into this picture. For example, *Makarevitch et al*. (2001) reported that while the VHF radar detected echoes with Doppler shifts near C_s, simultaneously operated HF radars often observed echoes with very small velocities, on the order of ~ 100 m/s in the same scattering volume. Another unexpected result was presented in Chapter 3 of this thesis, where we showed

that the HF velocity is often well below both C_s and the **E** x **B** component in a selected radar beam of the Stokkseyri radar.

The absence of HF echoes with velocities near C_s at strongly driven electrojet conditions and the onset of low velocity (< 200 m/s) echoes seem to contradict the FB instability concept and this clearly requires further investigation. Note that the fact that SuperDARN radars detect velocities well below the **E** x **B** component at short ranges has not been widely recognized by the SuperDARN community. For example, the currently available Map Potential software (*Ruohoniemi and Baker*, 1998) does not automatically eliminate E-region echoes from the analysis. Inclusion of these low-velocity echoes leads to underestimated electric fields in areas where E-region echoes have been observed. In this regard, investigation of the nature of the low-velocity echoes becomes even more important.

Another interesting aspect of these low-velocity echoes is the nature of the echoes at the shortest ranges, range gates 0 – 5. The velocity magnitudes of the low- velocity E-region echoes (~ 200 m/s) are very close to the neutral wind velocities at heights of ~ 90 km (*Hall et al*., 1997). In a series of SuperDARN publications, HF echoes detected in bins 0 – 5 were attributed to meteor-related echoes and their velocity was thought to be the velocity of the neutral wind. However, meteor echoes are not considered in this Chapter. The echoes we study occupy a significant portion of the Stokkseyri FoV; they persist for several hours and do not show discreteness in their appearance. Their widths are larger than or comparable to those of concurrent E-region echoes, and finally their velocities are somewhat larger than nominal neutral wind velocities observed by other instruments.

As the existence of low-velocity HF echoes is not often acknowledged, our goal in this Chapter is simply to present more information on their characteristics for strong **E** x **B** electron drifts and all flow angles.

5.2 Observations along the L shell: Event selection and approach to the analysis

The same approach as in the previous Chapter is used here, namely, the E-region echoes in the low numbered beams 0 – 2 are first considered. These beams are oriented

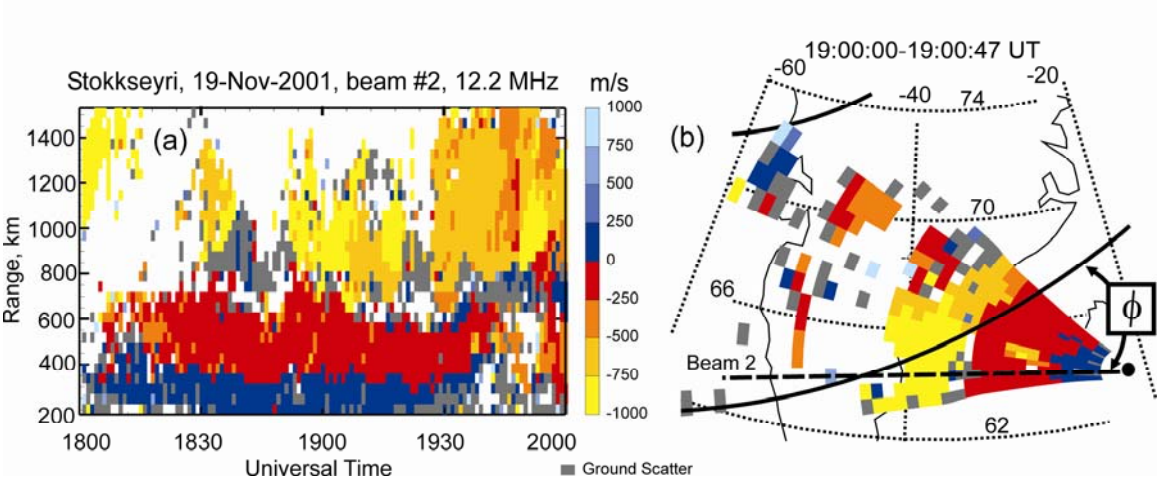

Figure 5.1: (a) Stokkseyri SuperDARN radar velocity in beam 2 at various ranges for the period of 18:00-20:00 UT on 19 November 2001 and (b) velocity map (in geographic coordinates) for the scan 19:00:00-19:00:47 UT. Thick lines are magnetic parallels of 70º and 80º. Dashed line shows the orientation of the radar beam 2. Angle ϕ is the L-shell (flow) angle.

close to the L-shell direction (the predominant direction of the **E** x **B** electron flow in the afternoon and evening sectors at magnetic latitudes ~ 70º), and we use the velocities of echoes at far ranges (> 700 km) as a proxy for the **E** x **B** magnitude.

Figure 5.1 illustrates the event selected. There exist two adjacent, temporally stable echo bands: high-velocity echoes (F-region echoes) at far ranges of 700 – 1500 km and much lower-velocity the echoes (E-region echoes) at short ranges of 200 – 700 km (Figure 5.1a). The echo bands are also distinguishable by their power. Additionally, it was common that while the F-region echoes demonstrated a strong variation of the velocity with the L-shell angle (Figure 5.1b), E-region echoes did not. For some beams, there was an occasional occurrence of high-velocity echoes at ranges < 700 km (yellow region at the center of the red region in Figure 5.1b) which could correspond to occasional reception of echoes from higher than the electrojet layer. One interesting feature for the selected event is the occurrence of echoes with opposite polarity (blue color) at the nearest ranges of 180 – 300 km. These echoes were termed as high aspect-angle irregularity region (HAIR) echoes (Milan et al., 2004).

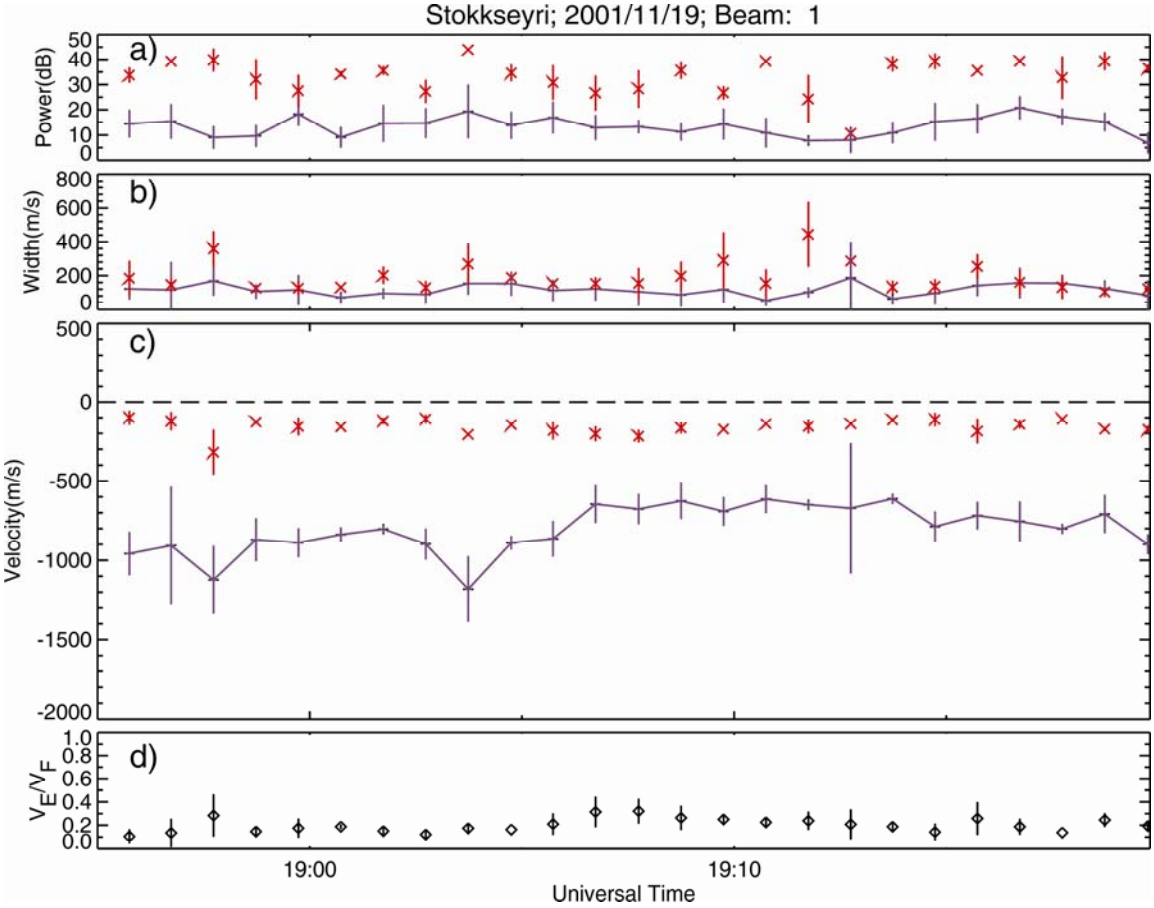

Figure 5.2: Temporal variations of (a) the averaged echo power, (b) spectral width and (c) velocity for the E-region and F-region echoes. Panel (d) shows the velocity ratio $R = V_E/V_F$. Red crosses represent the E-region parameters, plus signs connected by the lines represent F-region parameters, the diamonds are the ratio of the E-region velocity to the F-region velocity, and the vertical bars represent the errors in the averaged parameters.

5.2.1 E-region velocity along the flow and the E x B magnitude

Figure 5.2 gives the data presented in Figure 5.1 in the form of a line plot. E-region echoes are stronger but have widths comparable to the width of the F-region echoes (Figures 5.2a and b). Note that the considered short-range echoes were of typical power and Doppler width (e.g., *Makarevitch et al*., 2001).

To obtain the estimate of the E-region velocity least affected by the aspect angle effect, we consider the average velocity in 3 range gates corresponding to the range of the maximum in the echo power at short ranges (range gates 3 – 10) and the adjacent range

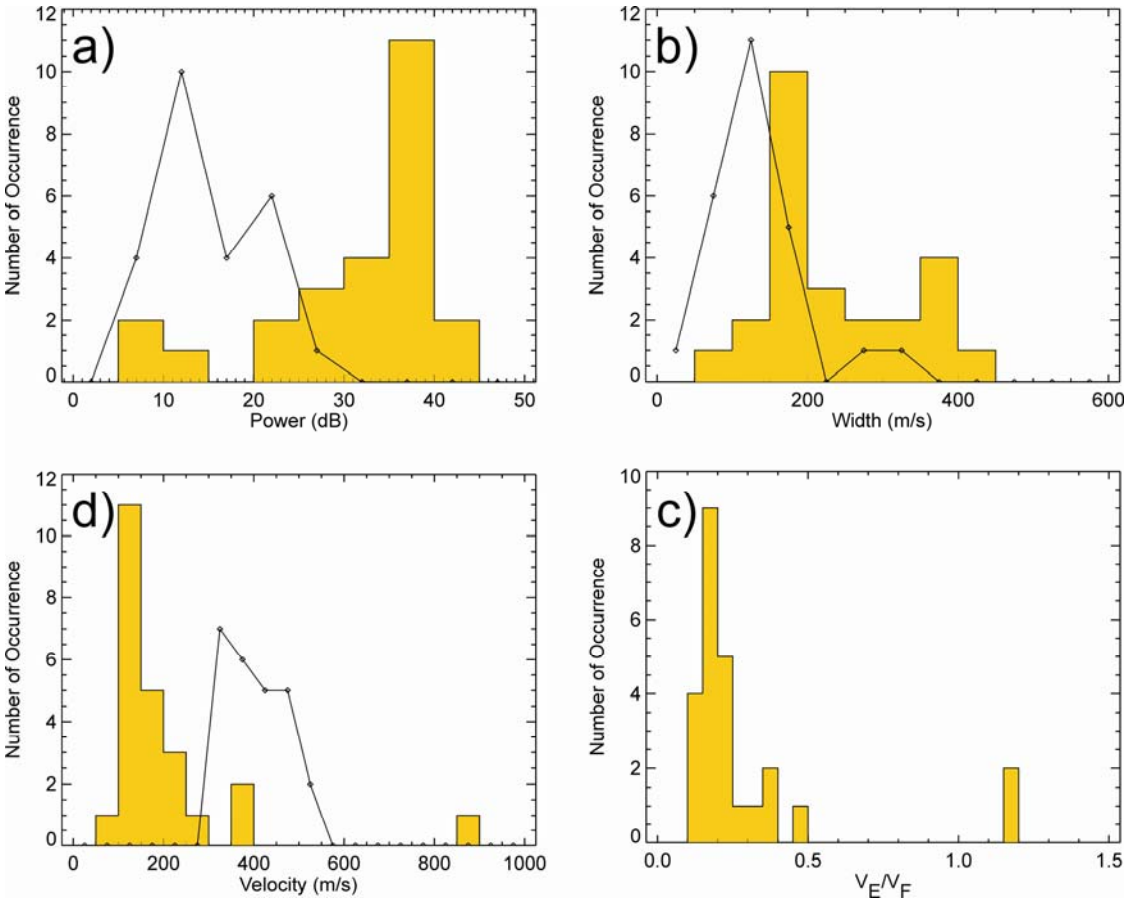

Figure 5.3: Histogram distributions for the parameters presented in Figure 5.2. F-region velocities (solid lines) were scaled down by a factor of 2.

gate in either direction along the beam. For the far range (F-region) echoes, the maximum velocity at ranges 700 – 1500 km was found and then the average velocity was computed by considering those gates in which the velocity was within 40% of the maximum value. This velocity is accepted as a proxy for the **E** x **B** electron drift component $\frac{E}{B}$ along the beam.

Figure 5.2c shows the temporal variations of V_E and V_F. V_E is below 200 m/s while $\frac{E}{B}$ is of the order of 800 m/s and varying between 600 and 1000 m/s. There seems to be no obvious correlation in the variations of V_E and V_F. The velocity ratio $R = V_E/V_F$ is $\sim 0.2 \pm 0.1$, which is smaller than the corresponding value for the high-velocity echoes.

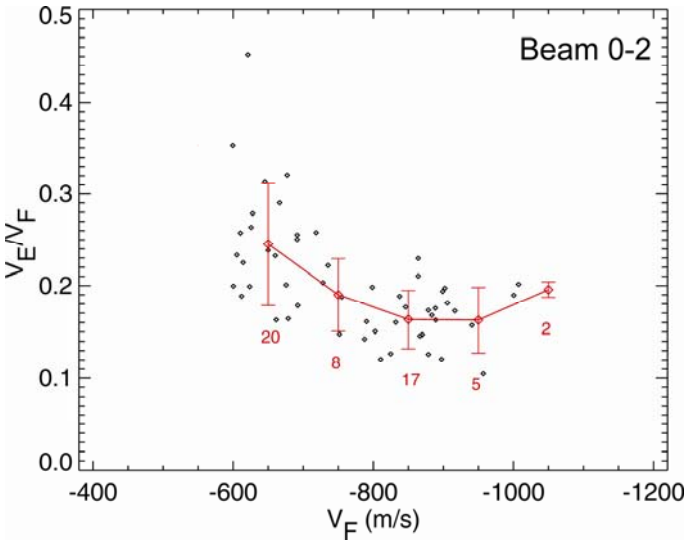

Figure 5.4: Velocity ratio $R = V_E/V_F$ versus V_F for the data collected in beams 0-2. Averaged value of R is shown as the red line, with the number of values averaged shown.

Figure 5.3 presents the same data in the form of histograms. One can see that the E-region echo power is ~ 15 dB larger than that of the F region, and the spectral widths are about the same, at ~ 150 m/s. The E-region velocities are almost a quarter of that in the F region, Figures 5.3c and d, with the maximum of the ratio R at about 0.2. This is 1.5 times smaller than for high-velocity echoes (Chapter 4).

Figure 5.4 presents the statistics for the velocity ratio $R = V_E/V_F$ versus V_F. Here, data from beams 0 and 1 were also considered to increase the point counts (velocity ratios in those beams were computed in the same way as in beam 2). Figure 5.4 confirms that typical value of R for the considered event is 0.2. R decreases with V_F reaching minimum value of ~ 0.15 at $V_F > 800$ m/s. Note that the above variation is quite clear, unlike for the high-velocity echoes in Chapter 4.

5.3 Observations along all beam: Flow angle variation for the E-region velocity

Figure 5.5 is a scatter plot for the E-region echo parameters (gates 3 – 10) versus the L-shell angle. The period between 18:55 UT – 19:20 UT on 19 November 2002 was considered. Here, many of the echoes are weaker at large ϕ, which is unusual for HF observations that usually demonstrate little flow angle dependence (*Koustov et al.*, 2001;

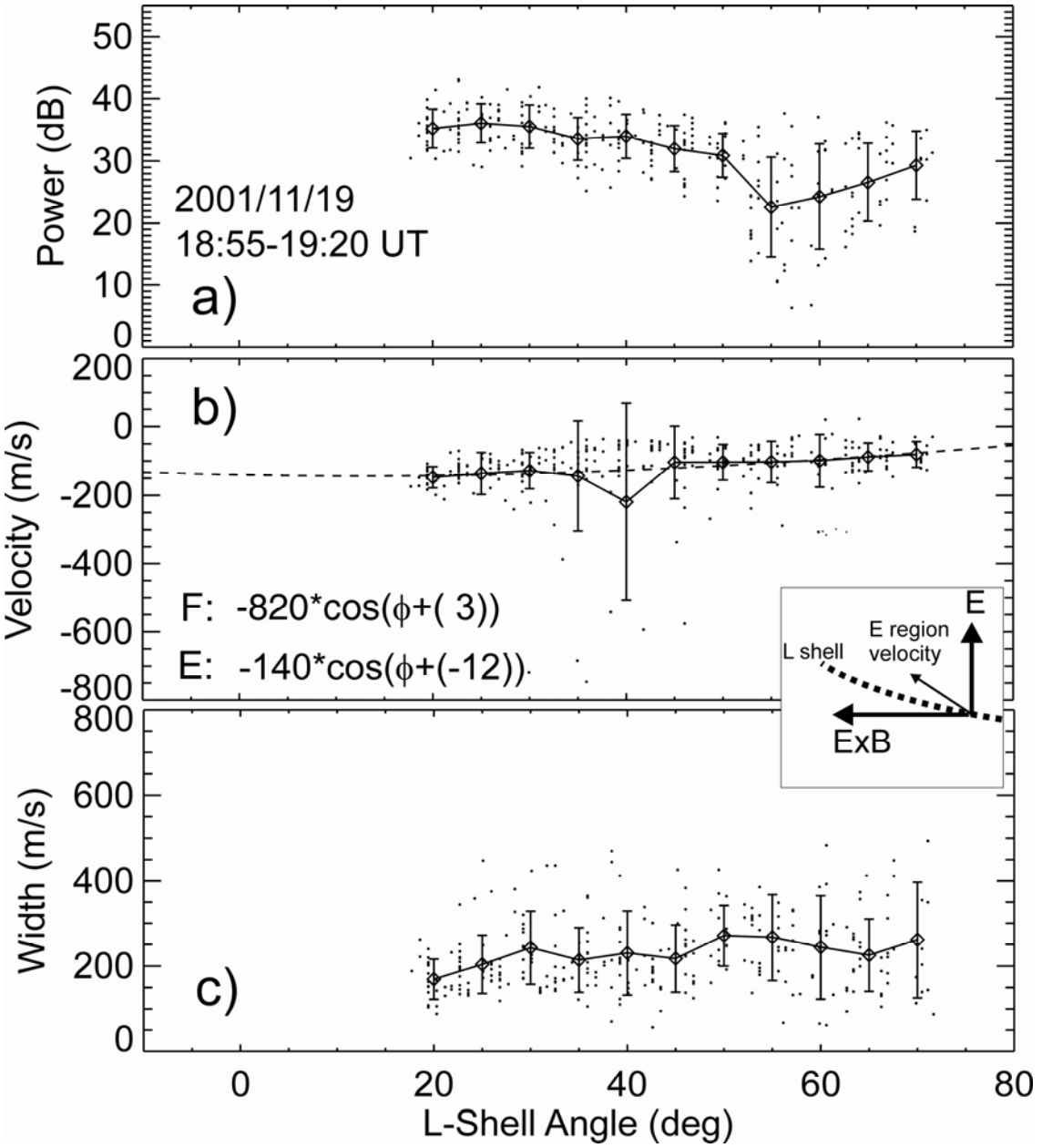

Figure 5.5: Scatter plot of measured echo power, velocity and spectral width for E-region echoes versus the L-shell angle. Data trends are illustrated by averaging and are shown as diamond connected by the solid lines. Cosine fit to the velocity is shown as a dashed line. The equation for the F-region fit is shown for reference. The inset between panels (b) and (c) shows the directions of the E-region velocity and the **E** x **B** drift with respect to the electric field and L-shell based on the fitted results. Errors in the parameters in the equations in panel (b) are not shown. They are less than ± 15º in the phase and ± 150 m/s and ± 300 m/s for the E- and F-region peak velocities respectively.

Makarevitch et al., 2002b). The echo velocity changes very little with ϕ, and if it is described by a cosine function, the maximum value would be ~ 140 m/s. This is significantly smaller than the F-region echo velocity of ~ 820 m/s. The velocity maximum is achieved at $\phi \sim 12^{\circ}$, rotated to the electric field direction from the **E** x **B** direction as shown in the insert of Figure 5.5. There is a trend in the spectral width to increase with ϕ, but it is not very pronounced.

To assess the velocity variation with the L-shell angle in Figure 5.5, the entire duration of the event was considered (~ 1/2 hour long) and plotted on one diagram all of the short-range echo velocities. The data is then averaged by using 5º bins in ϕ (Figure 5.5b). The averaged data were then fitted with the cosine function of a type $V = V_o\cos(\phi-\phi_o)$ to find V_o and ϕ_o, thus allowing some deviation of both the **E** x **B** flow and the maximum of the E-region velocity from the L-shell direction. According to Figure 5.5b, the cosine variation seems to describe the points well. Note that there is a ~ 15º difference in the velocity maximum directions, implying that the E-region velocity is maximized away from the **E** x **B** direction in the same manner as the high velocity E-region echoes considered in Chapter 4.

The second approach is to consider individual scans and to make cosine fits separately for the short and far-range echoes. Here we use the approach discussed in Chapter 4, namely, find the F- and E-region velocity estimates for each beam (each L-shell angle) and then make a cosine fit. The obtained dependence is then overlaid on top of all original points (in all beams) available so that assessment of the quality of the fit can be done. Figure 5.6 gives several examples for the 19 November 2002 event.

Consider Figure 5.6a. In this case, the F-region velocity and L-shell angle are -830 m/s and 10º respectively while the E-region velocity and L-shell are -130 m/s and 25º respectively, which is close to the statistical average for the entire event. It is noticeable that the points for the far-range echoes are well described by the fit line; for the E-region echoes it is less obvious. One special feature in this scan is that the short-range velocity is low, and it changes very little with the flow angle. Other scans show somewhat stronger variation, as in Figures 5.6b and c. Note that some short-range echoes have a velocity very close to the **E** x **B** component along the specific beams, supporting the notion that these echoes were coming from F-region heights. Figure 5.6d shows that

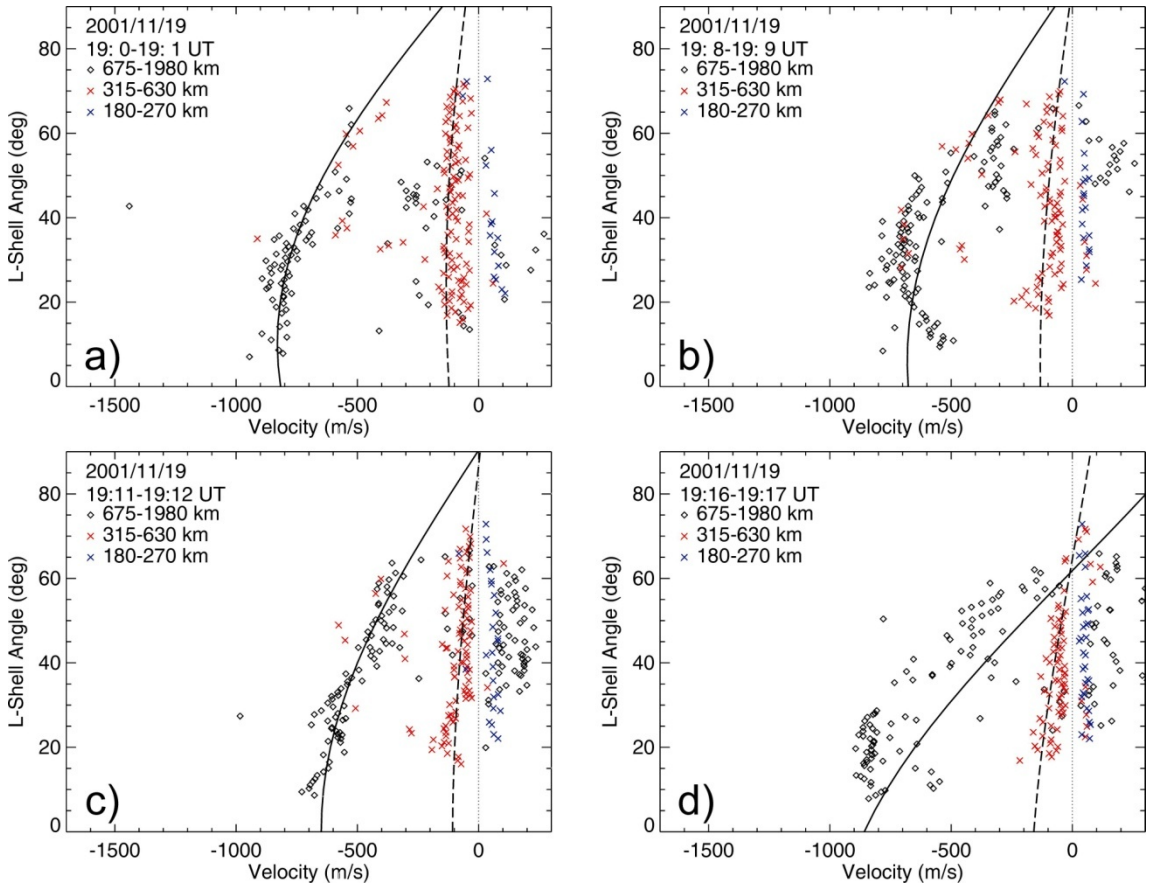

Figure 5.6: Velocity of short range (red and blue crosses) and far range (diamonds) echoes for four Stokkseyri scans on 19 November 2001. Overlaid are the cosine fit lines obtained separately for the far and short ranges. The blue crosses correspond to detection of HAIR echoes. Errors in the L-shell angle and velocity are not shown. They are ± 2º and ± 150 m/s respectively.

although the velocity of the F-region echoes changes significantly with the azimuth, showing a maximum at $\phi = 30º$ and contrary to the fitted cosine curve, E-region echoes do not show significant changes in velocity with ϕ.

We attempted to measure the difference between the azimuth of the **E** x **B** and the maximum of the cosine fit to the low-velocity echoes. Unfortunately, there were only 20 reasonable fits for the event of 19 November 2001. We found that $\Delta\phi = -15º$ on average, which is consistent with the result for the high-velocity echoes. Clearly, more events need to be identified and processed to draw a reliable conclusion.

5.4 HAIR echoes and their velocity with respect to the electric field direction

For most of the points in Figure 5.6, the velocity is of negative polarity. However, the blue crosses represent positive velocities that are presumably HAIR echoes. HAIR echoes also do not show a pronounced flow variation, although their velocity is sometimes larger at small ϕ (Figure 5.6a), or at intermediate ϕ (Figure 5.6b). *Milan et al*. (2004) related the velocity of HAIR echoes to the ion motions in an external electric field. However, this explanation does not work for the northward-oriented electric field that we expect in this case. Indeed, if the electric field is oriented across the L shells (Figure 5.1b), the velocity of HAIR echoes in high numbered beams should be negative, whereas Figure 5.1b clearly shows that the velocities are positive in those beams.

To reinforce this point, we present another case of HAIR echo observations, 5 November 2000 (Figure 5.7). In this diagram, a different color scheme was used for the velocity so that the HAIR echoes are seen as a green region at short-ranges of the large numbered beams. The F-region echoes did not exist in this case, but estimates of the electric field direction can be done by looking at the DMSP cross track ion drift measurements. One can see that the $\mathbf{E} \times \mathbf{B}$ drift changes its polarity at far edge of the region of echoes, near the L-shell line of 70º (Figure 5.7). In the areas equatorward of the 70º line, the electric field is oriented poleward, and so ions are moving poleward at electrojet heights. Thus, while the measured velocity is expected to be negative, it is in fact positive (Figure 5.7b). Note that the electric field can be rotated (20 - 30º) from the poleward direction such the observed component of the ion velocity could be negative, however, this would only hold for considerable clockwise (Figure 5.7b) rotation from the poleward direction.

We also identified events for which independent HAIR echoes were detected simultaneously by both the Stokkseyri and Pykkvibaer radars. For several of the events from both the Stokkseyri and Pykkvibaer radars, the interpretation of *Milan et al*. (2004) that HAIR echoes are simply the ion drift component in the electric field direction seems to be reasonable for the Pykkvibaer radar, but fails for the Stokkseyri radar. We suggest the interpretation of HAIR echoes by *Milan et al*. (2004) explains some HAIR echoes well, but does not provide a comprehensive classification.

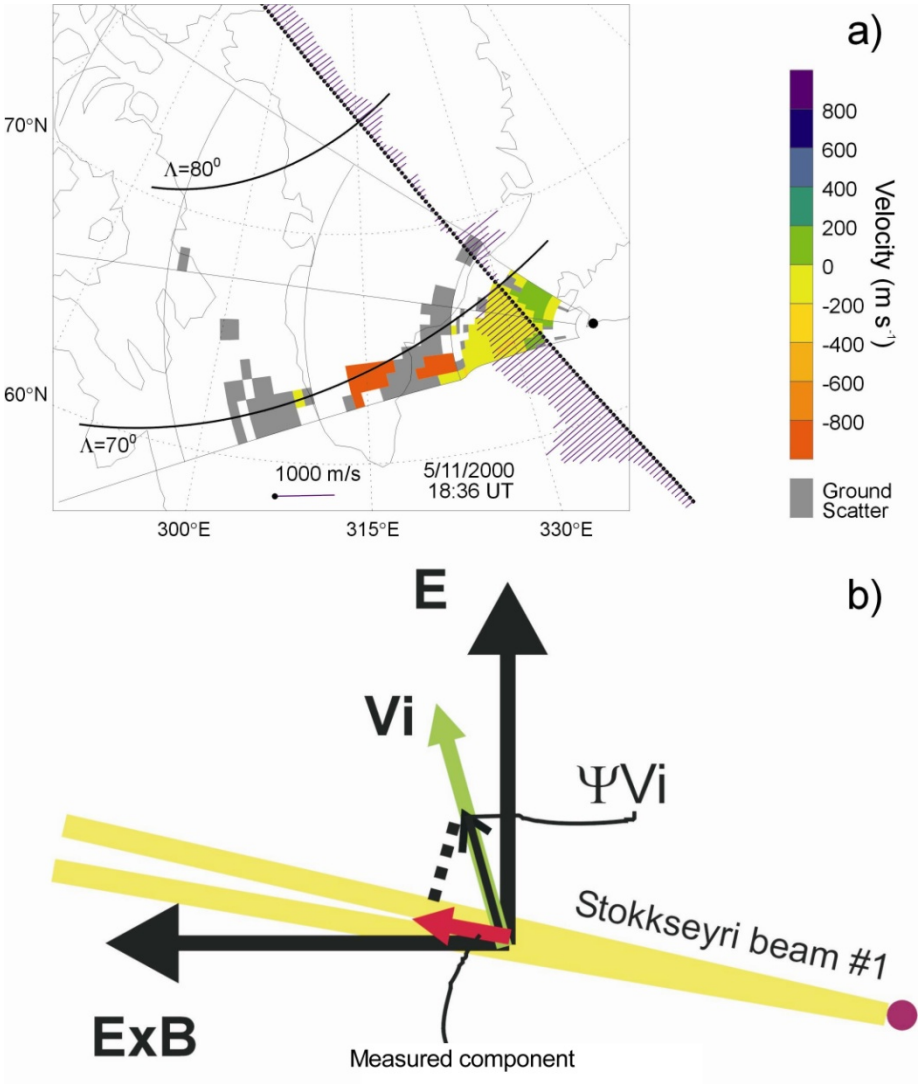

Figure 5.7: (a) Velocity map for Stokkseyri observations on 5 November 2000 and cross-track ion drift according to DMSP measurements. (b) Orientation of the electric field, **E** x **B** drift, ion drift and expected velocity within the linear theory of electrojet instabilities.

5.5 Summary of findings

This Chapter showed the frequent occurrence (by contrast to the occasional occurrence reported by *Makarevitch et al*. (2002b)) of low-velocity (< 200 m/s) short-range HF echoes at the Hankasalmi radar roughly along the **E** x **B** direction under the conditions of strong (> 800 m/s) **E** x **B** drifts. The velocity of these echoes is about a factor of 0.2 of the **E** x **B** drift magnitude. Their echo power and spectral width were not much different from that of the high-velocity echoes with velocities close to C_s. No

simultaneous HF echoes with Doppler shifts near the ion-acoustic speed of the medium were observed despite the fact of fast flows. We also pointed out the occurrence of the short-range HAIR echoes whose velocities were not consistent with the direction of the ion motion, contrary to the currently existing hypothesis.

CHAPTER 6

SUMMARY OF FINDINGS, DISCUSSION AND SUGGESTIONS FOR FUTURE RESEARCH

6.1 Discussion

In this thesis, the relationship between the velocity of E region echoes (irregularities) observed roughly along the electron flow direction by the Stokkseyri HF SuperDARN radar and the magnitude and direction of the **E** x **B** velocity was investigated. Strong drifts (electric fields) of more than 1000 m/s (50 mV/m) were targeted. The relationship with the ion-acoustic speed was also considered.

A comparison of the **E** x **B** velocity magnitude measured onboard DMSP satellites in the direction perpendicular to the satellite movement and the velocities of E-region echoes along that direction was performed. It was shown that the E-region echo velocity was typically smaller than the **E** x **B** drift component in a broad range of drifts between 0 and 1700 m/s. The velocity ratio $R = V_E/V_F$ was ~ 0.3 for drifts < 400 m/s and it was as low as 0.1 for drifts > 1000 m/s. The overall average R-value was 0.3 ± 0.1.

Stokkseyri radar observations in the afternoon and evening sectors were considered. A special configuration of echo distribution within the FoV was sought, namely events were selected when the radar detected echoes simultaneously at short (< 600 km, range gates 3 – 10) and far (600 – 2000 km, range gates 11 – 40) ranges and echoes were present in several bands along the radar beam. Another criterion employed was that the radar would show visually smaller velocity at short ranges compared with the far ranges on range-time-velocity plots. This implies that what was considered in this study is a special class of E-region echoes. An overview of the Stokkseyri data shows that E-region echoes with larger velocities are sometimes observed; these cases were not targeted in this thesis. The main reason is that one would not be able to determine

whether these echoes were received from electrojet heights or just above it, simultaneous observations with incoherent scatter radar are needed to investigate this class of echoes. In this thesis, distinguishing between E- and F-region echoes was done on the basis of significantly different velocities in the echo bands. Note that one could have tried the elevation angle information to help in the echo identification but the Stokkseyri radar elevation angle measurements are not considered reliable.

For the F-region echoes, it was assumed that the flow was homogeneous in all events considered and directed more or less ($\pm 30^{o}$) along the magnetic L shells. Under this assumption, if one considers observations in the low-numbered beams with orientations roughly along the L-shell direction, then the velocity of far-range echoes would be close to the **E** x **B** magnitude. On the other hand, if one considers variation of the far-range echo velocity with the azimuth, one would be able to infer more definitively the **E** x **B** velocity magnitude and direction, over the Stokkseyri FoV. Since concurrent short-range echoes were detected at magnetic latitudes very close to (and partially overlapping) the magnetic latitudes of the F-region echo detection, it was assumed that the inferred average (effective) **E** x **B** drift is a reasonable estimate of the **E** x **B** magnitude and direction in the area of the short-range E-region echoes.

Analysis of the Stokkseyri echoes observed at short and far ranges showed that irrespective of whether only low numbered beam data or data from all beams are considered, the velocity ratio R of the E-region echoes to the **E** x **B** drift has a value of about 0.3. This conclusion was made for **E** x **B** velocities up to 1500 m/s.

To support this conclusion, we present in Figure 6.1 the velocity ratio for the entire database of 41 events (Chapters 4 and 5 considered individual events). In Figure 6.1, we show the distribution of the velocity ratio R separately for low number beams and for all beams if one employs the same approach as for the low numbered beam observations. One can see that consideration of all the beams gives a somewhat narrower distribution, but the distribution peak is still around 0.3. One can notice a plateau slightly below R = 1 for the case of all beams. We interpret the occurrence of points with R ~ 1 as a manifestation of occasional Stokkseyri radar detection of echoes from the F region (above electrojet heights), even at short ranges. This is not an unexpected possibility for HF echoes as the amount of refraction can be significant (*Milan and Lester*, 1998).

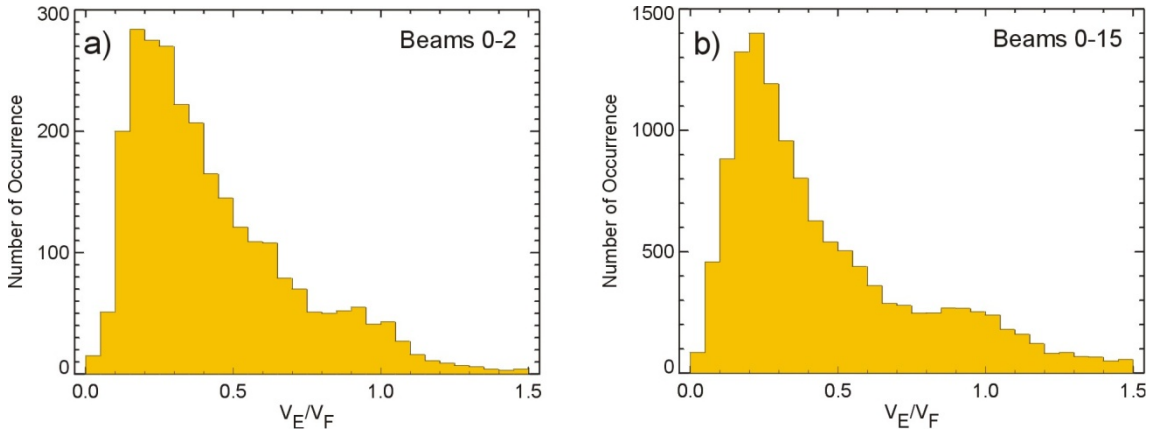

Figure 6.1: Histogram distribution for the velocity ratio R for the entire data set of 41 events: (a) in beams 0, 1 and 2 and (b) in all beams.

The two other characteristics of the considered E-region echoes - the power and spectral width - seem to be different from those reported in the past. For example, *Hanuise et al*. (1991) reported a typical power of ~ 10 dB (versus ~ 30 dB in our cases) and typical width of ~ 100 m/s (versus ~ 200 m/s in our case) using the Systeme HF d'Etude Radar Polaires et Aurorales (SHERPA) HF radar located at Schefferville, Quebec. *Milan and Lester's* (2001) data are more consistent with what has been reported here.

This thesis concludes that the E-region echoes considered in this study are consistent with Type 1 and 2 echoes according to the HF echo classification scheme of *Milan and Lester* (2001). However, the considered high-velocity echoes with velocities close to C_s did not have the narrow spectra expected for the Type 1 of *Milan and Lester* (2001). One fundamental difference between our observations is that the velocity of the echoes was changing with the flow angle while *Milan and Lester* (2001) expected no change for Type 1 echoes.

The echoes with low velocities do resemble Type 2 echoes, but an important feature is that their velocity is well below the **E** x **B** velocity component, a fact that was not considered by *Milan and Lester* (2001). The other difference is that, although we attempted to describe the velocity variation with the L-shell angle by a cosine function, several scans are not well described by the cosine function (see Figure 5.6).

It was shown that the E-region echoes were usually strong and exhibited clear maxima in the echo range profile at certain ranges, similar to *Koustov et al*. (2001) and

Makarevitch et al. (2001). We also showed that within the selected database, there are two types of E-region events, as far as the echo velocity magnitude is concerned. One type is echoes that have a velocity close to the ion-acoustic speed of the electrojet plasma. Echoes with such velocities were considered in numerous publications in the past at both VHF and HF (i.e., *Fejer and Kelley*, 1980; *Sahr and Fejer*, 1996). The second type of echoes that were considered had velocities substantially smaller than C_s, by a factor of 2 – 3; the HF velocity was persistently clustered around 150 – 200 m/s, similar to the low velocity echoes observed by *Villain et al.* (1990). These velocities are somewhat larger than the speed of the neutral wind at electrojet heights.

Importantly, even though these two types of E-region echoes were investigated for different events, it is not an uncommon that both types coexist. In Figure 6.2a we show the Stokkseyri velocity map for 1 November 2001, 16:04 – 16:6 UT, in which one can clearly see detection of very large velocities at far ranges and low velocities (with the exception of a small region) echoes at short ranges. In Figure 6.2b, we present the FFT spectra of the echoes observed at various range gates along beam 1. In range gates 2 – 4, only a slow component is observed; in range gates 6 and 8 two components are seen, one slow and one with the velocity magnitude close to C_s. Range gate 10 also has two velocity components: one related to C_s and the other one is the **E** x **B** component. Note that the detection of F-region (above electrojet heights) echoes whose velocity is the **E** x **B** component along the radar beam at short ranges is a common phenomenon. Consider Figure 3.3, which has a cluster of points (circled) at V_{DMSP} from −700 to −900 m/s, for which there was a reasonable agreement between the Stokkseyri and DMSP velocities. Another example is in Figure 5.1. These points indicate the occurrence of patches with enhanced electron density in the ionosphere, so that radio waves can be refracted to heights above the electrojet, even at short ranges. We note that the **E** x **B** component in gate 10 is ~ 1 km/s. This is less than the 1.5 km/s seen in gate 27. This difference is first of all because the flow angle for range gate 10 is about 10º larger than that of range gate 27. Also there might be some longitudinal inhomogeneity within the flow.

Frequent observation of E-region echoes with velocities distinctly smaller than the **E** x **B** velocity component along a radar beam is an important result of this research. This

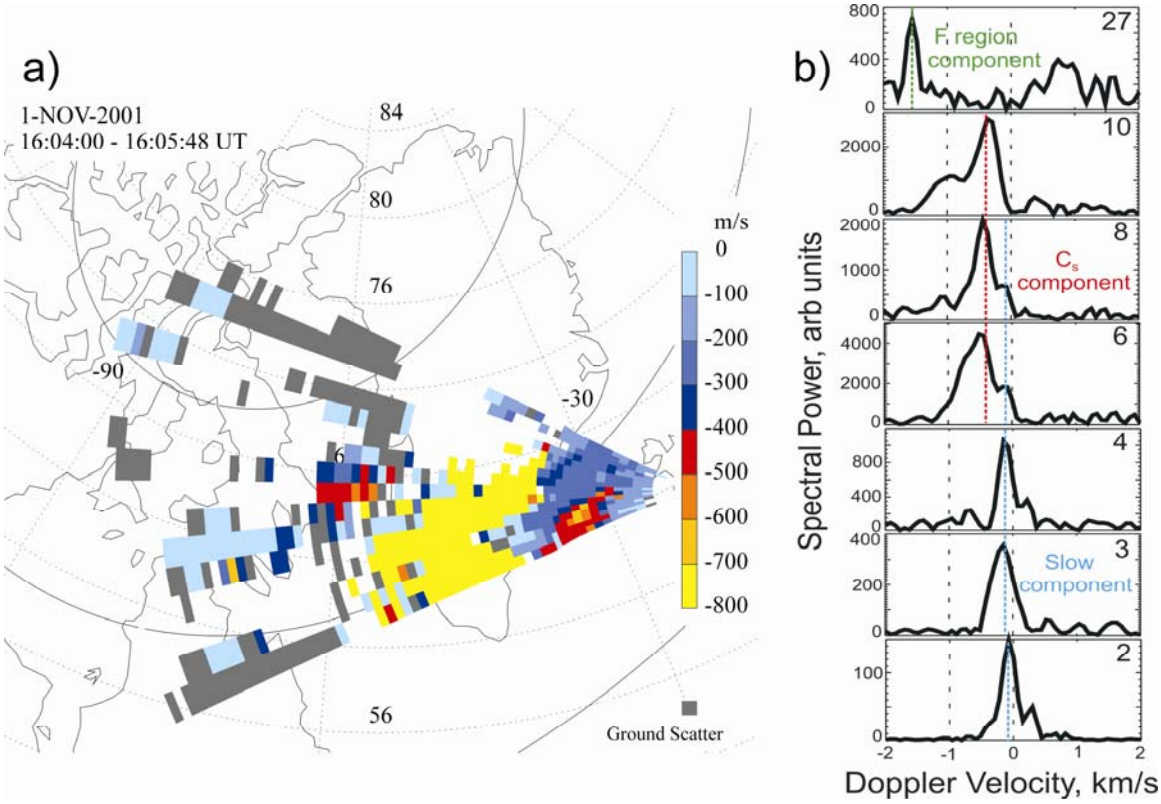

Figure 6.2: (a) Stokkseyri velocity map for 1 November 2001 at 16:06-16:08 UT and (b) spectra detected in beam 1 for selected range gates (numbers in the top right corner of the panels). Velocity scale was selected to highlight the velocity differences in the E-region.

is not an entirely unexpected discovery (i.e., *Makarevich et al.*, 2004). Yet here it was shown that the low-velocity echoes are systematically observed not only at large but also at small flow angles, for observations along the electrojet, and under the condition when only relatively high velocity, C_s related echoes are expected.

In the past, several explanations of the low-velocity echoes (compared to the **E** x **B** component) were considered. One assumption is that the phase velocity of decameter irregularities is modified by the sharp gradients of the background plasma, e.g., *Hanuise* (1991), *St-Maurice et al*. (1994) and *Milan and Lester* (2001). This explanation would require the presence of background density gradients of the proper orientation with scales on the order of several kilometers.

Alternatively, *Drexler et al.* (2002) recently proposed that at decameter scale the growth rate is small at electric fields less than 50 mV/m and non-local effects become

important to the generation of instabilities through convective or cascades from larger wavelength GD structures.

Another explanation is the irregularity phase velocity depression at low heights below the electrojet layer falls under the assumption that the conclusions of the linear theory of the FB and GD instabilities are still valid at the nonlinear stage of the instabilities (*Koustov et al*., 2002). Here we simply note that if echoes are mostly received from the bottom of the electrojet, the term $\frac{\nu_e \nu_i}{\Omega_e \Omega_i}$ is large and this would lead to strong velocity depression as compared to the **E** x **B** velocity magnitude. The velocity depression would be even stronger if the aspect angles of the observations are non-zero, e.g., 1º – 2º (Chapter 2).

With respect to the non-zero aspect angles, note that the E-region HF echoes are often believed to be received from exactly zero aspect angles (e.g., *Moorcroft*, 2002). However, *Uspensky et al*. (1994) and *Uspensky et al*. (2003) forwarded an idea that an E-region HF echo is a combination of scatter from a range of heights and a range of aspect angles so that the effective aspect angle is always non-zero. Whether this hypothesis is correct or not requires further investigation.

Another possible reason for strong velocity depression of the low-shifted components could be excitation of neutral wind related plasma instabilities (*Kagan and Kelley*, 1998; 2000), collisional thermal instabilities (*Dimant and Sudan*, 1995, 1997) or simply due to neutral wind turbulence (*Gurevich et al*., 1997). Note that the velocities of some of the low-shifted echoes are very close to zero, which might indicate that these echoes are simply the ground scatter received through anomalous radio wave propagation channels. Ground scatter at short ranges of 400 – 500 km can be expected in the presence of strong electron density patches. We should comment that some of the FFT spectra for the considered event were investigated. Analysis showed that they were usually asymmetric, consistent with *Danskin et al*. (2004), but the presence of two (or more) components was only identifiable with special methods such as the Burg method employed by *Danskin et al*. (2004). Visually, the spectra do not show strong power near zero velocity.

Additionally, the flow angle analysis for the velocity performed in this study assumed that the velocity of E-region echoes varies according to the cosine rule. This is a hypothesis that requires further investigation. For observations at large flow angles, one might expect deviations from the cosine rule because of the ion-drift contribution to the irregularity phase velocity as argued by *Makarevitch et al*. (2002b), who presented data for the E-region HF velocities that indicated the violation of the cosine rule. Later, *Makarevitch et al*. (2004) showed that inclusion of the ion contribution under the assumption of a finite aspect angle (as suggested by *Uspensky et al*., 2003) allows for an explanation of some features in the HF velocity azimuthal behavior identified by the Finland SuperDARN radar.

If the cosine dependence for $V_E(\phi)$ is acceptable, we showed that the velocity of the high-velocity E-region echoes does not contradict the hypothesis by *Bahcivan et al*. (2005) that the irregularity phase velocity is the ion-acoustic speed value projected onto the direction of a radar beam. One important part of this conclusion is that the height of the backscatter would have to be below 100 km. Another conclusion is that the empirical relationship by *Nielsen et al*. (2002) and results by *Nielsen and Schlegel* (1985) are not applicable to HF observations, the observed velocities can be consistently smaller than the ones measured at VHF.

An interesting result of our flow angle analysis is the fact that the speed of E-region echoes can be maximized away from the **E** x **B** direction, contrary to predictions of the linear theory of electrojet instabilities. No explanation of this effect is available at the moment. One might consider the theory proposed by *St-Maurice and Hamza* (2001) and later expanded by *Hysell and Drexler* (2006). Namely, one may propose that the polarization electric fields associated with the irregularities changes the direction of the macroscopic velocity maximum. For areas with an increased electron density, the maximum irregularity velocity would be rotated away from the **E** x **B** direction towards the electric field direction, similar to what has been reported in this thesis (Chapter 4). In areas with a depleted electron density, the rotation would be in the opposite direction, but these areas would contribute less to the total echo signal and would not lead to any observable effects.

Additionally, observations of low-velocity echoes along the electron flow direction at very large **E** x **B** drifts (Chapter 5) is another interesting result of this thesis. *Makarevitch et al*. (2002a) reported observations of similar echoes for the Syowa SuperDARN radar in Antarctica. For that study, estimates of the **E** x **B** component along the radar beam were made by simply looking at concurrent and co-located measurements by the 50 MHz VHF radar. At this frequency, it has been long believed that the 50 MHz velocity is the cosine component of the **E** x **B** drift (*Schlegel*, 1996). *Makarevitch et al*. (2001, 2002b) noticed the occasional occurrence of HF echoes with velocities ~ 100 – 150 m/s while the 50 MHz radar detected velocities > 500 m/s. Our Stokkseyri radar observations enhance *Makarevitch et al*.'s (2001, 2002b) result by showing that such echoes are not a rare occurrence but a regular phenomenon lasting for up to 2 hours in the eastward electrojet. Note that both our data and those reported by *Makarevitch et al*. (2001, 2002b) favor the cosine type of the low-velocity echo variation with the flow angle.

Finally, the HAIR echo results showed that the assumption that the velocity of these echoes is simply the component of the ion drift along the radar beam fails if one assumes that ions are fully controlled by the electric field. If one assumes that HAIR echoes are received from the bottom side of the electrojet layer, the velocity of the ions can be largely controlled by the neutral wind (Chapter 1). In this case, the explanation of *Milan et al*. (2004) about the nature of HAIR echoes could be correct if very fast neutral winds exist at the heights of ~ 90 km (Figure 6.3a), where the echo velocity is due to the ion velocity in the neutral wind velocity direction. In this case, the effect of the electric field can simply be overpowered by the neutral wind. Alternatively, if the direction of the electric field was rotated from the poleward direction (> 30º), it could be possible to observe opposite polarity echoes (Figure 6.3b) due to ions drifting with the electric field. It is also possible that these HAIR echoes may be the result of echoes being received from behind the radar; however, the elevation angle data from Stokkseyri required to investigate whether this is the case are not considered reliable.

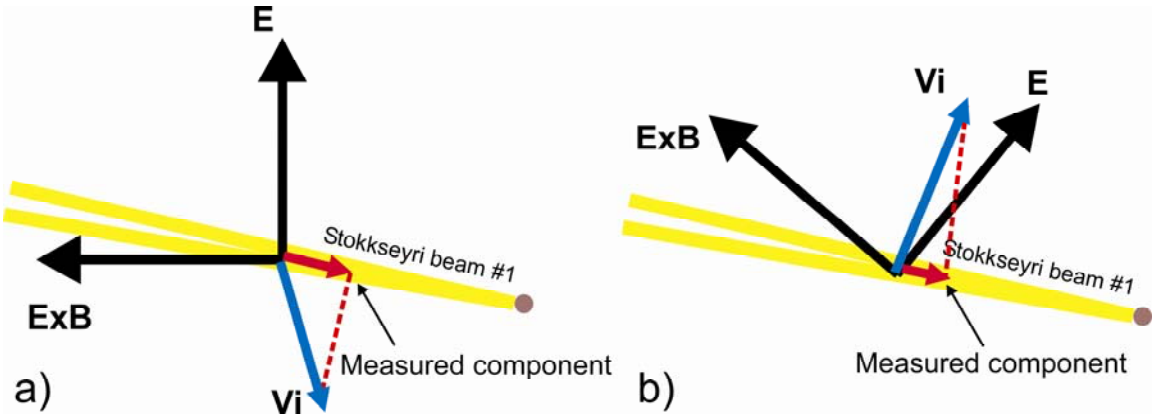

Figure 6.3: Orientation of the electric field, **E** x **B** drift, ion drift and velocity expected within the linear theory of electrojet instabilities. (a) for the case of neutral wind driven ions, (b) for the case of electric field driven ions.

6.2 Conclusions

To summarize what has been achieved in the present work:

1. Events has been identified for which the velocity of E-region echoes was significantly, by a factor of at least 2, smaller than the velocity of the **E** x **B** electron drift at electrojet heights. The echoes with such a depressed velocity were observed in the afternoon sector at auroral latitudes of ~ 65º for **E** x **B** drifts of more than 600 – 800 m/s, typically above 1000 m/s. The observations covered a range of directions, from almost along the **E** x **B** direction to up to ~ 70º – 80º from the **E** x **B** direction.
2. Within the identified group of events, there were cases when the velocity of echoes was close to the ion-acoustic speed of the medium at electrojet heights below ~ 100 km. These echoes were termed as the high-velocity echoes. The high-velocity echoes were somewhat stronger and broader than typical E-region echoes, observed, for example, by the SuperDARN radar at Syowa (Antarctica). For the high-velocity echoes, the velocity ratio with respect to the **E** x **B** magnitude was ~ 0.3, independent on the **E** x **B** magnitude. The velocity variation with the flow angle can be described reasonably by a cosine function. By fitting the velocity data, it was found that, in terms of the azimuth, the maximum velocity of E-region echoes was typically rotated away from the **E** x **B** direction

with a mean value of about 20º. The direction of this shift was clockwise, towards the northward oriented electric field, for the westward **E** x **B** drift of electrons.

3. There were a number cases where the velocity of the echoes was very small, but still above the typical speeds of the neutral wind at electrojet heights (150 – 200 m/s). Such events were rare, but lasted for rather long periods of up to an hour. These echoes were termed the low-velocity echoes. The power and spectral width of the low-velocity echoes were about the same as those for the high-velocity echoes. For the low-velocity echoes, the velocity ratio with respect the **E** x **B** magnitude was decreasing with an **E** x **B** increase with minimum values of the order of 0.15, i.e., a ratio about 2 times smaller than that for the high-velocity echoes.
4. Simultaneously with the low-velocity E-region echoes, echoes with opposite velocity polarity were often detected at shorter ranges. These were termed in the past as HAIR echoes. Cases were presented for which the velocity of HAIR echoes cannot be explained by assuming that the velocity is simply the component of the ion drift (at electrojet heights) due to electric field. It was suggested that involvement of strong neutral wind of proper direction or strongly rotated electri field (Figure 6.3) might explain the observations.
5. The occurrence of E-region echoes with velocity two or more times smaller than the **E** x **B** electron drift strongly suggest that the SuperDARN derivation of the convection patterns with currently employed Map Potential technique could be seriously underestimated at the equatorial edge of the SuperDARN combined zone, and care must be exercised when dealing with these observations.

6.3 Suggestions for future research

Ideally, to improve the knowledge of electrojet irregularity formation physics, one would want to have information on the electric field, electron and ion temperatures and the electron density distribution in the ionosphere within the FoV of an HF radar. Also, one would want to have a small scattering volume of the HF radar that would be comparable in size with the collection area of the other instrument. One would also want

to have the temporal resolution of the instruments involved as short as possible, say of the order of seconds, and comparable to each other. Unfortunately, such an experimental setup is unrealistic at this time and one is forced to use the best configurations available.

In this thesis, no measurements were available for several parameters. One of these is the ion-acoustic velocity at ~110 km (electron and ion temperatures), the parameter important for understanding the nature of coherent echoes observed along the electron flow at large electric fields. In this thesis, we used data collected by the EISCAT incoherent scatter radar over Tromsø, at about the same geomagnetic latitudes as the Stokkseyri FoV, but during different periods. The accepted functional dependence of C_s versus the electric field magnitude was derived by fitting a limited EISCAT data set to a quadratic function. This issue needs to be addressed in the future by obtaining a more extended EISCAT E-region temperature data set.

Since the velocity of HF E-region echoes show significant scatter, measurements of the ion-acoustic speed would decrease the degree on uncertainty in the arrived conclusions. Since temperature measurements can only be performed with incoherent scatter radar, one would hope that future EISCAT measurements concurrent with Hankasalmi SuperDARN radar would give more joint data, and this would be an important activity to be carried out.

In the near future, a new capable and highly flexible incoherent scatter radar will be installed at Resolute Bay, Nunavut. Unfortunately, this location is not convenient for E-region studies with the existing SuperDARN HF radars. The slant range for the Rankin Inlet PolarDARN radar is ~ 1300 km, and for the recently installed PolarDARN radar at Inuvik, NWT, the range is ~ 1500 km. Both ranges are beyond the radio horizon for E-region echoes, and installation of a new HF radar is needed (*Koustov*, personal communication, 2007). Perhaps the installation of a VHF radar with a scattering point over Resolute Bay would give opportunities to continue the work started in this thesis. If one considers a radar frequency of 50 MHz, the wavelength of the probed irregularities would be ~ 5 m for a bi-static configuration.

In this thesis, information on the electric field within the FoV of the Stokkseyri radar was obtained by considering concurrent DMSP measurements and by considering velocities of longer-range echoes detected by the radar simultaneously with the E-region

echoes. Both approaches had their own limitations, but the work can be extended in some aspects.

Currently, DMSP data are available at the U of Texas website for the period of ~ 4 years and one can envision a computerized search of joint SuperDARN/DMSP data by considering all radars. Note that in this thesis, the event selection was accomplished by visual inspection of SuperDARN plots and then the corresponding DMSP passes were found. Once again, the passes over the Stokkseyri FoV typically occur during times not optimal for echo detection at short ranges. As a part of this thesis, assessment of a DMSP/E-region echo investigation was performed for the Syowa radars in Antarctica. Preliminary conclusions are consistent with what has been reported in Chapter 3 of the thesis. One significant difference with the Stokkseyri observations is that E-region echoes exist there at very short ranges, 250 – 350 km while at ranges ~ 500 km F-region echoes are often observed. Since elevation angles are not available at Syowa, distinguishing between E and F-region echoes is a difficult task. The hope is that for other radar locations, the situation would be more favorable. Identifying joint DMSP/SuperDARN events might be beneficial for carrying out other projects for which the electric field information is substantial, i.e., identifying SAPS-like events (*Drayton*, 2005) or for an investigation of HF radar capabilities for detection of echoes at the equatorial edge of the auroral oval (*Jayachandran et al*., 2002). Additionally, the future Canadian Space Agency (CSA) enhanced Polar Outflow Probe (ePOP) satellite and the European Space Agency (ESA) Swarm satellite constellation missions will provide alternative sources of satellite derived drifts and they could be considered once sufficient data has been collected to create an adequate data set.

Another possibility in E-region irregularity studies is joint observations of the Saskatoon and Rankin Inlet SuperDARN radars. The idea is that the Saskatoon radars sometimes detect echoes at ranges of ~ 3000 km. The monitored area in this case overlaps with the area of E-region echo detection at Rankin Inlet. However, only the component of the flow along the Saskatoon beams would be available; this is certainly a limitation, but still the obtained data would be very useful, considering that the direction of the flow can be estimated. In addition, for some beam orientations, the differences between the Saskatoon and Rankin radar beam azimuths are of the order of 10º, which is

quite satisfactory for a comparison. One advantage of the Saskatoon/Rankin Inlet configuration is the fact that near noon and midnight, the flows are preferentially meridional so that data for observations along the flow would be available. The other encouraging circumstance is the fact that the velocities of the F-region echoes are above the threshold for the FB instability.

One more aspect of the work presented in this thesis that can be investigated further is the significant data scatter for the E-region echoes made it difficult to arrive at simple conclusions on the obtained trends in the data. Data on E-region echoes by *Milan and Lester* (2001) show much more consistency. These studies were based on a 15 km resolution of HF observations. This implies that a large scattering volume is a factor when properties of E-region irregularities are investigated. In view of this fact, it is worthwhile to run additional experiments with a 15 km resolution at Stokkseyri or other locations.

APPENDIX A

LIST OF EVENTS CONSIDERED IN THIS THESIS

Table A.1: List of events considered in this thesis

Date	Start (UT)	End (UT)	Date	Start (UT)	End (UT)
6-Feb-99	15:00	16:20	29-Sep-01	20:00	21:30
2-Apr-99	20:00	21:00	8-Oct-01	16:00	17:30
16-Jan-00	20:30	22:40	10-Oct-01	21:00	22:00
11-Mar-00	17:50	19:45	19-Oct-01	16:30	18:10
11-Mar-00	20:30	21:50	22-Oct-01	12:30	13:50
11-Apr-00	16:50	18:20	29-Oct-01	18:40	20:05
10-Oct-00	15:30	16:50	01-Nov-01	15:20	18:00
05-Nov-00	17:00	18:40	17-Nov-01	17:50	18:40
28-Nov-00	15:30	16:10	19-Nov-01	18:50	19:35
3-Dec-00	17:00	20:00	9-Dec-01	22:00	23:00
27-Dec-00	17:45	18:10	2-Jan-02	19:30	22:00
27-Dec-00	18:30	19:45	12-Jan-02	19:00	22:00
17-Jan-01	21:00	22:00	15-Jan-02	19:00	22:00
24-Jan-01	14:20	15:40	17-Feb-02	20:45	21:35
25-Jan-01	20:30	21:00	21-Feb-02	22:20	0:00
21-Feb-01	21:10	22:00	22-Feb-02	20:20	22:30
12-Mar-01	18:00	21:20	03-Mar-02	17:30	19:20
02-Apr-01	17:40	18:10	03-Mar-02	19:45	22:15
02-Apr-01	18:30	19:00	19-Sep-02	15:35	16:10
12-Sep-01	19:30	21:50	2-Dec-02	19:00	21:00
18-Sep-01	18:00	19:00			

APPENDIX B

PROGRAM USED TO MAKE COSINE FITS TO VELOCITY VARIATION WITH L-SHELL ANGLE

```
;Program written by James Gorin
;Purpose: To calculate the L-shell angle based on cosine fits to SD
;velocity data

;included from SuperDARN program library
@/home/stk/usr/code/src.idl/sasgenlib.pro
@/home/stk/idl/lib/time.pro

;cosine fitting routine
FUNCTION do_trend_fit,x_arr,y_arr,err,a,fit_sdv,yerr
  num = n_elements(x_arr)
  w = intarr(num)
  FOR i=0,num-1 DO w(i) = 1
  IF num GE 8 THEN BEGIN
    y_fit = curvefit(x_arr,y_arr,w,a,fit_sdv,$
      function_name='cos_fit_funct',status=stus,iter=itr,$
        itmax=200,tol=0.0000001,yerror=yerr)
    IF stus EQ 0 THEN result = 1 ;fit succesful
    IF stus EQ 1 THEN result = 2 ;fit failed
  ENDIF ELSE BEGIN
     result = 3 ;too few data to fit
  ENDELSE
  RETURN,result
END

;cosine function and partial derivatives required for fit
PRO cos_fit_funct, x, a, f, pder
  f = a[0]*cos((x)+a[1])
  IF N_PARAMS() GE 4 THEN $
    pder = [[cos((x)+a[1])],[-a[0]*sin((x)+a[1])]]
END

;example code to run fit routine repeatedly
PRO run_fit

  plot_fitavg,'20011101_1516','nov_1_2001/'

END

;master routine for plotting and fitting data
PRO plot_fitavg,temp,loc
  print,'Executing '+temp
  minbeam=0
  maxbeam=15
  files = strarr(1000)
  files=findfile('/home/gorin/Working/flow_angle/reanalysis/'+$
```

```
    loc+temp+'.txt',count=file_count)
  dummy = ''
  time = fltarr(50000)
  beamnum = time
  e_vel = fltarr(50000)
  f_vel = e_vel
  e_vel_sd = e_vel
  e_pow = e_vel
  e_wid = e_vel
  e_err = e_vel
  f_vel = e_vel
  f_vel_sd = e_vel
  f_pow = e_vel
  f_wid = e_vel
  f_err = e_vel
  e_bin = intarr(50000)
  f_bin = e_bin

  ;define plot
    !p.font=0

    set_plot,'ps'
    device,/landscape,/inches,xsize=10.3125,ysize=7.9688,/helvetica, $
    filename='vel_angle_scan/'+temp+'_vel_angle_figq.ps',font_size=8,$
      yoffset=10.8125,xoffset=0.25,/color

  ;read in data
  j=0l
  zz=0
  FOR i = 0, file_count-1 DO BEGIN
    openr,lun,files(i),/get_lun

readf,lun,yr,dummy,month,dummy,day,dummy,format='(i4,a1,i2,a1,i2,a0)'
    readf,lun,dummy
    WHILE NOT eof(lun) DO BEGIN
      readf,lun,time1,beamnum1,e_vel1,e_vel_sd1,e_pow1,e_wid1,e_err1,$
        f_vel1,f_vel_sd1,f_pow1,f_wid1,f_err1,$
        e_bin1,f_bin1,format = '(i5,i6,10f9.2,2i9)'
        IF zz EQ 1 THEN BEGIN
          timestamp1=time1
          zz=zz+1
        ENDIF
        IF zz EQ 0 THEN BEGIN
          timestamp0=time1
          zz=zz+1
        ENDIF
    IF Abs(e_vel1) le 750 AND beamnum1 GE minbeam AND beamnum1 LE $
      maxbeam AND Abs(f_vel1) gt 35 AND Abs(e_vel1) gt 35 AND e_wid1 $
        GE 35 AND f_wid1 GE 35 AND f_err1 LE 250 AND e_err1 LE 100 $
          AND e_vel_sd1 LE 100 AND f_vel_sd1 LE 250 AND $
            f_vel_sd1 GT 0 THEN BEGIN
        time(j) = time1
        beamnum(j) = beamnum1
        IF beamnum1 GE minbeam AND beamnum1 LE maxbeam AND $
          Abs(e_vel1) gt 0 AND e_wid1 GE 5 AND e_err1 LE 100 $
            AND e_vel_sd1 LE 100 THEN BEGIN
        e_vel(j) = e_vel1
```

```
      e_vel_sd(j) = e_vel_sd1
      e_pow(j) = e_pow1
      e_wid(j) = e_wid1
      e_err(j) = e_err1
      f_vel(j) = f_vel1
      ENDIF ELSE BEGIN
      e_vel(j) = -9999
      e_vel_sd(j) = -9999
      e_pow(j) = -9999
      e_wid(j) = -9999
      e_err(j) =-9999
      f_vel(j) = -9999
      ENDELSE
      IF beamnum1 GE minbeam AND beamnum1 LE maxbeam AND $
        Abs(f_vel1) gt 0 AND f_wid1 GE 5 AND f_err1 LE 250 AND $
          f_vel_sd1 LE 250 THEN BEGIN
      f_vel(j) = f_vel1
      f_vel_sd(j) = f_vel_sd1
      f_pow(j) = f_pow1
      f_wid(j) = f_wid1
      f_err(j) = f_err1
      e_bin(j) = e_bin1
      f_bin(j) = f_bin1
      ENDIF ELSE BEGIN
      f_vel(j) = -9999
      f_vel_sd(j) = -9999
      f_pow(j) = -9999
      f_wid(j) = -9999
      f_err(j) = -9999
      e_bin(j) = -9999
      f_bin(j) = -9999
      ENDELSE
      j+=1
    ENDIF
  ENDWHILE
  free_lun,lun

ENDFOR

time = time(0:j-1)
beamnum = beamnum(0:j-1)
e_vel = e_vel(0:j-1)
e_vel_sd = e_vel_sd(0:j-1)
e_pow = e_pow(0:j-1)
e_wid = e_wid(0:j-1)
e_err = e_err(0:j-1)
f_vel = f_vel(0:j-1)
f_vel_sd = f_vel_sd(0:j-1)
f_pow = f_pow(0:j-1)
f_wid = f_wid(0:j-1)
f_err = f_err(0:j-1)
e_bin = e_bin(0:j-1)
f_bin = f_bin(0:j-1)
j = j-1
get_angle,l_shell

start_time = time(0)
```

```
end_time = time(n_elements(time)-1)
x_loc = (findgen(34)-17)*5
angles = (3.14159/180.)*x_loc
bin=2.5*3.14159/180.
plot_loc = 0

!p.multi=[0,1,2,0,1]

;sort data
IF timestamp1-timestamp0 GE 7 THEN scan_time=120 ELSE IF $
  timestamp1-timestamp0 LE 4 THEN scan_time=60
num_scan = (end_time-start_time)/scan_time
e_vel_fit = fltarr(num_scan)
e_vel_sdv = e_vel_fit
e_azi_fit = e_vel_fit
e_azi_sdv = e_vel_fit
e_vel_max = e_vel_fit
f_vel_fit = fltarr(num_scan)
f_vel_sdv = f_vel_fit
f_azi_fit = f_vel_fit
f_azi_sdv = f_vel_fit
f_vel_max = f_vel_fit
fit_time = fltarr(num_scan)


FOR i=0,num_scan-1 DO BEGIN
  scrng = where(time GE (start_time+(scan_time*i)) AND time LT $
    start_time+(scan_time*(i+1))),num)
  IF num GT 0 THEN BEGIN
    e_region_vel = fltarr(num)
    e_region_angle = fltarr(num)
    f_region_vel = fltarr(num)
    f_region_angle = fltarr(num)

    FOR k=0,num-1 DO BEGIN
      IF e_bin(scrng(k)) GT 2 THEN BEGIN
        e_region_vel(k) = e_vel(scrng(k))
        e_region_angle(k) = $
          l_shell(beamnum(scrng(k)),e_bin(scrng(k)))
      ENDIF ELSE BEGIN
        e_region_vel(k) = -9999
        e_region_angle(k) = -9999
      ENDELSE
      f_region_vel(k) = f_vel(scrng(k))
      f_region_angle(k) = l_shell(beamnum(scrng(k)),f_bin(scrng(k)))
    ENDFOR
    e_region_angle_rad=e_region_angle*3.14159/180.
    f_region_angle_rad=f_region_angle*3.14159/180.
    edat = where(e_region_vel NE -9999,nm)
    IF nm GT 0 THEN BEGIN
      e_region_vel = e_region_vel(edat)
      e_region_angle = e_region_angle(edat)
      e_region_angle_rad = e_region_angle_rad(edat)
    ENDIF
    fdat = where(f_region_vel NE -9999,nm)
    IF nm GT 0 THEN BEGIN
      f_region_vel = f_region_vel(fdat)
```

```
  f_region_angle = f_region_angle(fdat)
  f_region_angle_rad = f_region_angle_rad(fdat)
ENDIF
;fit cos f-region
afmax = max(f_region_vel)
afmaxloc = where(f_region_vel EQ afmax)
afmin = min(f_region_vel)
afminloc = where(f_region_vel EQ afmin)
IF abs(afmax) GT abs(afmin) THEN BEGIN
  A_F = [0.9*(max(f_region_vel)),f_region_angle_rad(afmaxloc)]
  f_vel_max(i) = afmax
ENDIF ELSE BEGIN
  A_F = [0.9*(min(f_region_vel)),f_region_angle_rad(afminloc)]
  f_vel_max(i) = afmin
ENDELSE

yrsec=start_time+(scan_time*i)
result = TimeYrsecToYMDHMS(yr,mo,dy,hr,mt,sc,yrsec)
fit_time(i) = yrsec
gtitle = 'single scan average: '+string(yr,format='(i4)')+'/'+$
  string(month,format='(i0)')+'/'+string(day,format='(i0)')+' '+$
  string(hr,format='(i2)')+':'+string(mt,format='(i2)')+$
    'UT, bin 11-40, beams 0-15'
plot,f_region_angle,f_region_vel,title=gtitle,ytitle=$
  'vel (m/s)',xtitle='L-shell angle (deg)',$
    yrange=[-1900,100],xrange=[-10,80],$
      psym=1,charsize=1.5,/xstyle,/ystyle

result2 = do_trend_fit(f_region_angle_rad,f_region_vel,$
  f_vel_sd,A_F,A_F_sd,yerr)
A_F1 = A_F[1]
IF result2 EQ 1 THEN oplot,x_loc,A_F[0]*cos(angles+A_F1),$
  linestyle=1,thick=1
IF result2 EQ 1 THEN xyouts,-5,-200,string(A_F[0],$
  format='(i5)')+'*cos(X+('+string(A_F1*180/3.14159,$
  format='(f0.2)')+'))',charsize=0.8
IF result2 EQ 1 THEN xyouts,-5,-400,'yerr = '+$
  string(yerr,format='(f6.2)'),charsize=0.8
IF result2 EQ 2 THEN xyouts,-5,-200,$
  'Fit failed: Chi-squared increasing without bound',$
  charsize = 0.8
IF result2 EQ 3 THEN xyouts,-5,-200,$
  'Fit failed: Insufficient data',charsize = 0.8
IF result2 EQ 1 THEN f_vel_fit(i) = A_F[0] ELSE $
  f_vel_fit(i) = -9999
IF result2 EQ 1 THEN f_azi_fit(i) = A_F1*180/!pi ELSE $
  f_azi_fit(i) = -9999
IF result2 EQ 1 THEN f_vel_sdv(i) = yerr ELSE $
  f_vel_sdv(i) = -9999
IF result2 EQ 1 THEN f_azi_sdv(i) = A_F_sd[1]*180/!pi $
  ELSE f_azi_sdv(i) = -9999

;fit cos e-region
aemax = max(e_region_vel)
aemaxloc = where(e_region_vel EQ aemax)
aemin = min(e_region_vel)
aeminloc = where(e_region_vel EQ aemin)
```

```
    IF abs(aemax) GT abs(aemin) THEN BEGIN
      A_E = [0.9*(max(e_region_vel)),e_region_angle_rad(aemaxloc)]
      e_vel_max(i) = aemax
    ENDIF ELSE BEGIN
      A_E = [0.9*(min(e_region_vel)),e_region_angle_rad(aeminloc)]
      e_vel_max(i) = aemin
    ENDELSE

    gtitle = string(yr,format='(i4)')+'/'+$
      string(month,format='(i0)')+'/'+string(day,format='(i0)')+$
        ' '+string(hr,format='(i2)')+':'+string(mt,format='(i2)')+$
        ' '+  'UT, bin 3-10, beams 0-15'
    plot,e_region_angle,e_region_vel,title=gtitle,$
      ytitle='vel (m/s)',xtitle='L-shell angle (deg)'$
      ,yrange=[-600,100],xrange=[-10,80],psym=1,$
      ,  charsize=1.5,/xstyle,/ystyle
    result3 = do_trend_fit(e_region_angle_rad,$
      e_region_vel,e_vel_sd,A_E,A_E_sd,yerr)
    A_E1 = A_E[1]
    IF result3 EQ 1 THEN oplot,x_loc,A_E[0]*cos(angles+A_E1),$
      linestyle=1,thick=1
    IF result3 EQ 1 THEN xyouts,-5,-80,$
      string(A_E[0],format='(i5)')+'*cos(X+('+$
      string(A_E1*180/3.14159,format='(f0.2)')+'))',charsize=0.8
    IF result3 EQ 1 THEN xyouts,-5,-180,'yerr = '+$
      string(yerr,format='(f6.2)'),charsize=0.8
    IF result3 EQ 2 THEN xyouts,-5,-80,$
      'Fit failed: Chi-squared increasing without bound',$
      charsize = 0.8
    IF result3 EQ 3 THEN xyouts,-5,-80,$
      'Fit failed: Insufficient data',charsize = 0.8
    IF result2 EQ 1 THEN e_vel_fit(i) = A_E[0] ELSE $
      e_vel_fit(i) = -9999
    IF result2 EQ 1 THEN e_azi_fit(i) = A_E1*180/!pi ELSE $
      e_azi_fit(i) = -9999
    IF result2 EQ 1 THEN e_vel_sdv(i) = yerr ELSE $
      e_vel_sdv(i) = -9999
    IF result2 EQ 1 THEN e_azi_sdv(i) = A_E_sd[1]*180/!pi ELSE $
      e_azi_sdv(i) = -9999
  ENDIF ELSE BEGIN
    yrsec=start_time+(scan_time*i)
    result = TimeYrsecToYMDHMS(yr,mo,dy,hr,mt,sc,yrsec)
    gtitle = 'No data '+string(yr,format='(i4)')+'/'+$
      string(month,format='(i0)')+'/'+string(day,format='(i0)')+$
      ' '+string(hr,format='(i2)')+':'+string(mt,format='(i2)')
    plot,[0,0],[0,0],title=gtitle,ytitle='vel (m/s)',$
      xtitle='L-shell angle (deg)',yrange=[-1700,0],$
        xrange=[-80,80],psym=3,charsize=1.5,/xstyle,/ystyle,$
          symsize=0.1
    plot,[0,0],[0,0],title=gtitle,ytitle='vel (m/s)',$
      xtitle='L-shell angle (deg)',yrange=[-1700,0],$
      xrange=[-80,80],psym=3,charsize=1.5,/xstyle,/ystyle$
        ,symsize=0.1
  ENDELSE
ENDFOR
```

```
  device,/close
  ;store fitting results
  output = loc+temp+'_results.txt'
  openw,lun,output,/get_lun
  printf,lun,string(yr,format='(i4)')+'/'+string(month,format='(i0)')$
      +'/'+string(day,format='(i0)')
  printf,lun,'   time    e_vel_fit    e_azi_fit    e_vel_max    '+$
    'f_vel_fit    f_azi_fit    f_vel_max    e_vel_err    f_vel_err'+$
      '    e_azi_sdv    f_azi_sdv'
  FOR pf=0, num_scan -1 DO BEGIN
    IF fit_time(pf) NE 0 THEN printf,lun,fit_time(pf),$
      e_vel_fit(pf),e_azi_fit(pf),e_vel_max(pf),f_vel_fit(pf),$
        f_azi_fit(pf),f_vel_max(pf),$
      e_vel_sdv(pf),f_vel_sdv(pf),e_azi_sdv(pf),f_azi_sdv(pf)$
        format = '(i7,10f13.2)'
  ENDFOR
  free_lun,lun
END

;routine to calculate l-shell angles from magnetic field and radar los
PRO get_angle,l_shell
  ;initialize variables
  st_id = 8 ;for stokkseyri
  year = 2000 ;same year as the magnetic field modle used,
  ;no bearing on radar position
  yrsec = 0 ;begining of year, no bearing on radar position
  frange = 180 ;common mode
  rngsep = 45 ;common mode
  ht = 110 ;default height
  rad_pos_geo = fltarr(3,75,16)
  rad_pos_mag = fltarr(3,75,16)
  ;get radar los
  FOR i=0,15 DO BEGIN
    pos = rbpos_james(st_id,findgen(75)+1,i,frange,rngsep,$
      height=ht,/geo,/center)
    rad_pos_geo(0:2,0:74,i) = pos
    pos = rbpos_james(st_id,findgen(75)+1,i,frange,rngsep,$
      height=ht,/center)
    rad_pos_mag(0:2,0:74,i) = pos
  ENDFOR
  ;reorganize results, done to make this section compatible with older
  ;code
  rad_coord = fltarr(16,75,3)
  mag_coord = fltarr(16,75,3)
  FOR i=0,15 DO BEGIN
    FOR j=0,74 DO BEGIN
      rad_coord(i,j,0) = rad_pos_geo(0,j,i)
      rad_coord(i,j,1) = rad_pos_geo(1,j,i)
      rad_coord(i,j,2) = rad_pos_geo(2,j,i)
      mag_coord(i,j,0) = rad_pos_mag(0,j,i)
      mag_coord(i,j,1) = rad_pos_mag(1,j,i)
      mag_coord(i,j,2) = rad_pos_mag(2,j,i)
    ENDFOR
  ENDFOR
  l_angle = fltarr(16,75)
  l_pos1 = fltarr(2)
  l_pos2 = l_pos1
```

```
  m_pos1 = fltarr(2)
  m_pos2 = m_pos1
  all_azi = fltarr(16,75,2)
  ;conversion of coordinates and calculation of l-shell angle
  FOR i=0,15 DO BEGIN
    FOR j=0,74 DO BEGIN
      ;find mag coords of bin centre
      ;vary mlon by small amount
      m_pos1(0) = mag_coord(i,j,0)
      m_pos1(1) = mag_coord(i,j,1)-.1
      m_pos2(0) = mag_coord(i,j,0)
      m_pos2(1) = mag_coord(i,j,1)+.1
      ;convert lpos to geo, calc heading for l shell
      g_pos1 = cnvcoord(m_pos1(0),m_pos1(1),mag_coord(i,j,2)-6371,/geo)
      g_pos2 = cnvcoord(m_pos2(0),m_pos2(1),mag_coord(i,j,2)-6371,/geo)
      m_azi = map_2points(g_pos1(1),g_pos1(0),g_pos2(1),g_pos2(0))
      ;calculate heading for radar beam
      IF j NE 0 AND j NE 74 THEN BEGIN
      r_azi = map_2points(rad_coord(i,(j-1),1),rad_coord(i,(j-1),0),$
        rad_coord(i,(j),1),rad_coord(i,(j),0))
      ENDIF
      IF j EQ 0 THEN BEGIN
      r_azi = map_2points(rad_coord(i,j,1),rad_coord(i,j,0),$
        rad_coord(i,(j+1),1),rad_coord(i,(j+1),0))
      ENDIF
      IF j EQ 74 THEN BEGIN
      r_azi = map_2points(rad_coord(i,(j-1),1),rad_coord(i,(j-1),0),$
        rad_coord(i,j,1),rad_coord(i,j,0))
      ENDIF

      IF m_azi(1) LT 0 THEN m_azi(1) = m_azi(1) +180
      IF r_azi(1) LT 0 THEN r_azi(1) = r_azi(1) +180
      all_azi(i,j,0) = m_azi(1)
      all_azi(i,j,1) = r_azi(1)

      l_angle(i,j) = (r_azi(1)-m_azi(1))
    ENDFOR
  ENDFOR
  !p.multi=[0,1,1]
  l_angle_corr = l_angle
  IF ht GT 150 THEN BEGIN
    FOR i = 0, 15 DO BEGIN
      m = (l_angle(i,15)-l_angle(i,8))/(7.)
      b = l_angle(i,8) - (m*8.)
      FOR j = 9, 14 DO BEGIN
        l_angle_corr(i,j) = (m*j)+b
      ENDFOR
    ENDFOR
  ENDIF
  l_angle_smooth = smooth(l_angle_corr,3)
  l_shell=l_angle_smooth

END



;plot y error bars
```

```
PRO error_bar_y,x,y,y_e,x_e,clr
 oplot,[x,x],[y-y_e,y+y_e],color=clr,thick=4
 oplot,[x-x_e,x+x_e],[1.0,1.0]*(y-y_e),color=clr,thick=4
 oplot,[x-x_e,x+x_e],[1.0,1.0]*(y+y_e),color=clr,thick=4
END

;plot x error bars
PRO error_bar_x,x,y,y_e,x_e,clr
 oplot,[x-x_e,x+x_e],[y,y],color=clr,thick=2
 oplot,[1.0,1.0]*(x-x_e),[y-y_e,y+y_e],color=clr,thick=2
 oplot,[1.0,1.0]*(x+x_e),[y-y_e,y+y_e],color=clr,thick=2
END

;routine to calculate radar beam/gate positions based on spherical
;geometry
FUNCTION rbpos_james,$
    station,  $ ; station id
    range,    $ ; array of range gates [starting at 1] for which
                ;to calculate position
    beam,    $ ; beam number [only one] for which to calculate
positions
    frange,    $ ; range to first sample [km]
    rsep,    $ ; range separation [km]
    height=height,  $ ; assumed height of backscatter, default 300km
    center=center,  $ ;does nothing at this point
    geo=geo      ; if set calculate geographic positions, otherwise
                 ;geomagnetic

  IF NOT KEYWORD_SET( height) THEN height= 300.0
  IF (keyword_set(geo)) THEN mgflag = 0 else mgflag = 1

  IF station EQ 8 THEN BEGIN
    lon = -22.02
    lat = 63.86
    skaz0 = (-59.0 - (7.5*3.24)) ;Stokkseyri
  ENDIF
  IF station EQ 9 THEN BEGIN
    lon = -20.54
    lat = 63.77
    skaz0 = (30.0 - (7.5*3.24)) ;Pykkvibaer
  ENDIF
  IF station NE 8 AND station NE 9 THEN print,'Station id unknown'

  re=6371.0 ; Radius of the Earth
  h=height ; Scattering Height
  width=3.24    ; width of beams
  pi=3.1415926
  pi1=pi/180.0 ; used for conversions to/from radians/degrees
  pi2=180.0/pi
  num_ranges= N_ELEMENTS(range)
  pos= fltarr( 3, num_ranges)

  FOR i=0,num_ranges-1 DO BEGIN
    rng=frange+(i+0.5)*rsep
    az=skaz0+beam*3.24
    colat=pi/2.-pi1*lat
    beta=az*pi1
```

```
    nu=ACOS((1.-(rng^2-h^2)/2/re/(re+h)))
    r1=ACOS(COS(nu)*COS(colat)+SIN(nu)*SIN(colat)*COS(beta))
    r2=SIN(beta)*SIN(nu)/COS(pi/2.-r1)
    lon2=lon+pi2*ASIN(r2) ; longitude position
    lat2=90.-r1*pi2 ; latitude position
    IF mgflag EQ 0 THEN BEGIN
      pos(0,i)=lat2
      pos(1,i)=lon2
      pos(2,i)=h+6371.
    ENDIF
    IF mgflag EQ 1 THEN BEGIN
      mpos=cnvcoord(lat,lon,h)
      s=AACGMConvert(lat,lon,h,mpos(0),mpos(1))
      pos(0,i)=mpos(0)
      pos(1,i)=mpos(1)
      pos(2,i)=h+6371
    ENDIF
  ENDFOR

  RETURN, pos
END

;routine to calculate arctan with result in the proper quadrant
FUNCTION Arctan2,x,y

  Phi2=fltarr(n_elements(x))
  M_PI=!pi
  FOR i=0,n_elements(x)-1 DO BEGIN
  dpi=180/M_PI
  Phi = atan(sqrt((y(i)*y(i))/(x(i)*x(i))))
  IF x(i) EQ 0 THEN BEGIN

    IF y(i) EQ 0 THEN Phi2(i)=-1
    IF y(i) GT 0 THEN Phi2(i)=(M_PI/2)*dpi
    IF y(i) LT 0 THEN Phi2(i)=(3*M_PI/2)*dpi
  ENDIF
  IF y(i) EQ 0 THEN BEGIN

    IF x(i) GT 0 THEN Phi2(i)=0
    IF x(i) LT 0 THEN Phi2(i)= M_PI*dpi
  ENDIF
  IF x(i) GT 0 AND y(i) GT 0 THEN Phi2(i)= (Phi)*dpi
  IF x(i) LT 0 AND y(i) GT 0 THEN Phi2(i)= (M_PI-Phi)*dpi
  IF x(i) LT 0 AND y(i) LT 0 THEN Phi2(i)= (M_PI+Phi)*dpi
  IF x(i) GT 0 AND y(i) LT 0 THEN Phi2(i)= ((2*M_PI)-Phi)*dpi

ENDFOR
RETURN,Phi2
END
```

REFERENCES

Bahcivan, H., D. L. Hysell, M. F. Larsen, and R. F. Pfaff, The 30 MHz imaging radar observations of auroral irregularities during the JOULE campaign, *J. Geophys. Res*., 110, doi:10.1029/2004JA010975, 2005.

Baumjohann, W., and R. A. Treumann, *Basic Space Plasma Physics*, Imperial College Press, Singapore, 1996.

Danskin, D. W., A. V. Koustov, T. Ogawa, N. Nishitani, S. Nozawa, S. E. Milan, M. Lester, and D. André, On the factors controlling occurrence of F-region coherent echoes, *Ann. Geophys*., 20, 1385–1397, 2002.

Danskin, D. W., *HF auroral backscatter from the E and F regions*, Ph. D. Thesis, University of Saskatchewan, 2003.

Danskin, D. W., A. V. Koustov, R. A. Makarevitch, and M. Lester, Observations of double-peaked E-region coherent spectra with the CUTLASS Finland HF radar, *Radio Sci*., 39, doi:10.1029/2003RS0029032, 2004.

Davies, J. A., M. Lester, S. E. Milan, and T. K. Yeoman, A comparison of velocity measurements from the CUTLASS Finland radar and the EISCAT UHF system, *Ann. Geophys*., 17, 892–902, 1999.

Dimant, Y. S., and R. N. Sudan, Kinetic theory of the Farley- Buneman instability in the E-region of the ionosphere, *J. Geophys. Res*., 100, 14605–14623, 1995.

Dimant, Y. S., and R. N. Sudan, Physical nature of a new cross-field current-driven instability in the lower ionosphere, *J. Geophys. Res*., 102, 2551–2563, 1997.

Dimant, Y. S., and G. M. Milikh, Model of anomalous electron heating in the E region: 1. Basic theory, *J. Geophys. Res*., 108, doi:10.1029/2002JA009524, 2003.

Drayton, R. A., A. V. Koustov, M. R. Hairston, and J.-P. Villain, Comparison of DMSP cross-track ion drifts and SuperDARN line-of-sight velocities, *Ann. Geophys.*, 23, 2479–2486, 2005.

Drexler, J., J.-P. St.-Maurice, D. Chen, and D. R. Moorcroft, New insights from a nonlocal generalization of the Farley-Buneman instability problem at high latitudes, *Ann. Geophys*., 20, 2003–2025, 2002.

Drexler, J., and J.-P. St.-Maurice, A possible origin for large aspect angle "HAIR" echoes seen by SuperDARN radars in the E region, *Ann. Geophys*., 23, 767–772, 2005.

Ecklund, W. L., B. B. Balsley, and D. A. Carter, A preliminary comparison of F-region plasma drifts and E-region irregularity drifts in the auroral zone, *J. Geophys. Res*., 82, 195–197, 1977.

Foster, J. C., and P. J. Erickson, Simultaneous observations of E-region coherent backscatter and electric field magnitude at F-region heights with the Millstone Hill UHF radar, *Geophys. Res. Lett*., 27, 3177–3180, 2000.

Fejer, B. G., and M. C. Kelley, Ionospheric irregularities, *Rev. Geophys. Space Phys*., 18, 401–454, 1980.

Fejer, B. G., Natural Ionospheric Plasma Waves, in *Modern Ionospheric Science*, edited by H. Kohl et al., European Geophysics Society, Germany, 1996.

Greenspan, M. E., P. B. Anderson, and J. M. Pelagatti, Characteristics of the thermal plasma monitor (SSIES) for the Defense Meteorological Satellite Program (DMSP spacecraft S8 through F10), *Tech. Rep. AFGL-TR-86-0227*, Hanscom AFB, Mass., 1986.

Greenwald, R. A., W. Weiss, E. Nielsen, and N. R. Thomson, STARE: A new radar auroral backscatter experiment in Northern Scandinavia, *Radio Sci*., 13, 1021–1029, 1978.

Greenwald, R. A., K. B. Baker, J. R. Dudeney, M. Pinnock, T. B. Jones, E. C. Thomas, J.-P. Villain, J.-C. Cerisier, C. Senior, C. Hanuise, R. D. Hunsuker, G. Sofko, J. Koehler, E. Nielsen, R. Pellinen, A. D. M. Walker, N. Sato, and H. Yamagishi, DARN/SuperDARN: A global view of the dynamics of high- latitude convection, *Space Sci. Rev*., 71, 763–796, 1995.

Gurevich, A. V., N. D. Borisov, and K. P. Zybin, Ionospheric turbulence induced in the lower part of the E-region by the turbulence of the neutral atmosphere, *J. Geophys. Res*., 102, 379–388, 1997.

Haldoupis, C., A review on radio studies of auroral E-region ionospheric irregularities, *Ann. Geophys*., 7, 239–258, 1989.

Hall, G. E., J. W. MacDougall, D. R. Moorcroft, J.-P. St.-Maurice, A. H. Manson, and C. E. Meek, Super Dual Auroral Radar Network observations of meteor echoes, *J. Geophys. Res.,* 102, 14603–14614, 1997.

Hamza, A. M., and J.-P. St.-Maurice, A turbulent theoretical framework for the study of current-driven E region irregularities at high latitudes: Basic derivation and application to gradient-free situations, *J. Geophys. Res*., 98, 11587–11599, 1993a.

Hanuise, C., J.-P. Villain, J. C. Cerisier, C. Senior, J. M. Ruohoniemi, R. A. Greenwald, and K. B. Baker, Statistical study of high-latitude E-region Doppler spectra obtained with SHERPA HF radar, *Ann. Geophys*., 9, 273–285, 1991.

Hargreaves, J. K., *The Solar-Terrestrial Environment*, Cambridge University Press, Cambridge UK, 1992.

Hysell, D.L., and J. Drexler, Polarization of elliptic E region plasma irregularities and implications for coherent radar backscatter from Farley-Buneman waves, *Radio Sci*., 41, doi:10.1029/2005RS003424, 2006.

Jayachandran, P. T., J.-P. St.-Maurice, J. W. MacDougall, and D. R. Moorcroft, HF detection of slow long-lived E region plasma structures, *J. Geophys. Res.*, 105, 2425–2442, 2000.

Jayachandran, P. T., J. W. MacDougall, J.-P. St-Maurice, D. R. Moorcroft, P. T. Newell, and P. Prikryl, Coincidence of the ion precipitation boundary with the HF E region backscatter boundary in the dusk-midnight sector of the auroral oval, *Geophy. Res. Lett.*, 29, doi:10.1029/2001GL014184, 2002.

Johnson, C. Y., Ion and neutral composition of the ionosphere, *Annals of the IQSY*, 5, 1969.

Kagan, L. M., and M. C. Kelley, A wind-driven gradient drift mechanism for mid-latitude E-region ionospheric irregularities, *Geophys. Res. Lett.*, 25, 4141–4144, 1998.

Kagan, L. M., and M. C. Kelley, A thermal mechanism for generation of small-scale irregularities in the ionospheric E region, *J. Geophys. Res.*, 105, 5291–5303, 2000.

Kelley, M. C., *The Earth's Ionosphere: Plasma Physics and Electrodynamics*, Academic Press, San Diego California, 1989.

Kivelson, M. G., and C. T. Russell, *Introduction to Space Physics*, Cambridge University Press, Cambridge UK, 1995.

Koustov, A. V., K. Igarashi, D. André, K. Ohtaka, N. Sato, H. Yamagishi, and A. S. Yukimatu, Observations of 50- and 12-MHz auroral coherent echoes at the Antarctic Syowa station, *J. Geophys. Res.*, 106, 12875–12887, 2001.

Koustov, A. V., D. W. Danskin, M. V. Uspensky, T. Ogawa, P. Janhunen, N. Nishitani, S. Nozawa, M. Lester, and S. E. Milan, Velocities of auroral coherent echoes at 12 and 144 MHz, *Ann. Geophys.*, 20, 1647–1661, 2002.

Koustov, A. V., D. W. Danskin, R. A. Makarevitch, and J. D. Gorin, On the relationship between the velocity of E-region HF echoes and E×B plasma drift, *Ann. Geophys.*, 23, 1–9, 2005.

Koustov, A. V., and J. D. Gorin, Observations of low-velocity short-range HF echoes at strongly driven electrojet conditions, Proceedings of the MST-11 Workshop, December 11–15, 2006, pp. 92–96, 2007.

Kustov, A. V., and C. Haldoupis, Irregularity drift velocity estimates in radar auroral backscatter, *J. Atmos. Terr. Phys.*, 54, 415–423, 1992.

Kustov, A. V., M. V. Uspensky, G. J. Sofko, J. A. Koehler, and J. Mu, Aspect angle dependence of the radar aurora Doppler velocity, *J. Geophys. Res.*, 99, 2131–2144, 1994.

Kustov, A. V., J. A. Koehler, G. J. Sofko, D. W. Danskin, and A. Schiffler, Relationship of the SAPPHIRE-North merged velocity and the plasma convection velocity derived from simultaneous SuperDARN radar measurements, *J. Geophys. Res.*, 102, 2495–2501, 1997.

Makarevitch, R. A., *Formation of small-scale irregularities in the auroral E region*, Ph.D. Thesis, University of Saskatchewan, 2003.

Makarevitch, R. A., T. Ogawa, K. Igarashi, A. V. Koustov, N. Sato, K. Ohtaka, H. Yamagishi, and A. S. Yukimatu, On the power-velocity relationship for 12- and 50-MHz auroral coherent echoes, *J. Geophys. Res*., 106, 15455–15469, 2001.

Makarevitch, R. A., A. V. Koustov, G. Sofko, D. André, and T. Ogawa, Multi-frequency measurements of HF Doppler velocity in the auroral E region, *J. Geophys. Res*., 107, doi:10.1029/2001JA000268, 2002a.

Makarevitch, R. A., A. V. Koustov, K. Igarashi, N. Sato, T. Ogawa, K. Ohtaka, H. Yamagishi, and A. S. Yukimatu, Comparison of flow angle variations of E-region echo characteristics at VHF and HF, *Adv. Polar Upper Atm. Res*., 16, 59–83, 2002b.

Makarevitch, R. A., F. Honary, and A. V. Koustov, Simultaneous HF measurements of E- and F-region Doppler velocities at large flow angles, *Ann. Geophys*., 22, 1177–1185, 2004.

Makarevich, R. A., F. Honary, V. S. C. Howells, A. V. Koustov, S. E. Milan, J. A. Davies, A. Senior, I. W. McCrea, and P. L. Dyson, A first comparison of irregularity and ion drift velocity measurements in the E region, *Ann. Geophys*., 24, 2375–2389, 2006.

Makarevich, R. A., A. V. Koustov, A. Senior, M. Uspensky, F. Honary, and P. L. Dyson, Aspect angle dependence of the E region irregularity velocity at large flow angles, *J. Geophys. Res.*, 112, doi:10.1029/2007JA012342, 2007.

Milan, S. E., T. K. Yeoman, M. Lester, E. C. Thomas, and T. B. Jones, Initial backscatter occurrence statistics from the CUTLASS HF radars, *Ann. Geophys*., 15, 703–718, 1997.

Milan, S. E., and M. Lester, Simultaneous observations at different altitudes of ionospheric backscatter in the eastward electrojet, *Ann. Geophys*., 16, 55–68, 1998.

Milan, S. E., and M. Lester, Spectral and flow angle characteristics of backscatter from decameter irregularities in the auroral electrojet, *Adv. Space Res*., 23, 1773–1776, 1999.

Milan, S. E., and M. Lester, A classification of spectral populations observed in HF radar backscatter from the E region auroral electrojets, *Ann. Geophys*., 19, 189–204, 2001.

Milan, S. E., M. Lester, N. Sato, and H. Takizawa, On the altitude dependence of spectral characteristics of decametre-wavelength E region backscatter and the relationship with optical auroral forms, *Ann. Geophys*., 19, 205–217, 2001.

Milan, S. E., M. Lester, T. K. Yeoman, T. R. Robinson, M. V. Uspensky, and J.-P. Villain, HF radar observations of high-aspect angle backscatter from the E-region, *Ann. Geophys.*, 22, 829–847, 2004.

Milikh, G. M., and Y. S. Dimant, Kinetic model of electron heating by turbulent electric field in the E region, *Geophys. Res. Let*., 29, doi:10.1029/2001GL013935, 2002.

Milikh, G. M., and Y. S. Dimant, Model of anomalous electron heating in the E region: 2. Detailed numerical modeling, *J. Geophys. Res*., 108, doi:10.1029/2002JA009527, 2003.

Moorcroft, D. R., Outstanding issues in the theory of radar aurora: Evidence from the frequency dependence of spectral characteristics, *J. Geophys. Res*., 107, doi:10.1029/2001JA009218, 2002.

Nielsen, E., Aspect angle dependence of mean Doppler velocities of 1-m auroral plasma waves, *J. Geophys. Res*., 91, 10173–10177, 1986.

Nielsen, E., and K. Schlegel, Coherent radar Doppler measurements and their relationship to the ionospheric electron drift velocity, *J. Geophys. Res*, 90, 3498–3504, 1985.

Nielsen, E., C. F. del Pozo, and P. J. S. Williams, VHF coherent radar signals from the E region ionosphere and the relationship to electron drift velocity and ion acoustic velocity, *J. Geophys. Res*., 107, doi:10.1029/2001JA900111, 2002.

Nozawa, S., and A. Brekke, Studies of the auroral E region neutral wind through a solar cycle: Quiet days, *J. Geophys. Res*., 104, 45–66, 1999.

Ogawa, T., B. B. Balsley, W. L. Ecklund, D. A. Carter, and P. E. Johnston, Aspect angle dependence of irregularity phase velocities in the auroral electrojet, *Geophys. Res. Lett*., 7, 1081–1084, 1980.

Ogawa, T., B. B. Balsley, W. L. Ecklund, D. A. Carter, and P. E. Johnston, Auroral radar observations at Siple Station, Antarctica, *J. Atmos. Terr. Phys*., 44, 529–537, 1982.

Otani, N. F., and M. Oppenheim, A saturation mechanism for the Farley-Buneman Instability, *Geophys. Res. Let*., 25, 1833–1836, 1998.

Otani, N. F., and M. Oppenheim, Saturation of the Farley-Buneman instability via three-mode coupling, *J. Geophys. Res*., 111, doi:10.1029/2005JA011215, 2006.

Press, W. H., and W. T. Vetterling, *Numerical Recipes: The Art of Scientific Computing*, Cambridge University Press, Cambridge UK, 1986.

Rees, M. H., *Physics and Chemistry of the Upper Atmosphere*, Cambridge University Press, Cambridge UK, 1989.

Reinleitner, L. A., and E. Nielsen, Self-consistent analysis of electron drift velocity measurements with the STARE/SABRE system, *J. Geophys. Res*., 90, 8477–8486, 1985.

Rich, F. J., and M. Hairston, Large-scale convection patterns observed by DMSP, *J. Geophys. Res.*, 99, 3827–3844, 1994.

Ruohoniemi, M., and K. B. Baker, Large-scale imaging of high-latitude convection with Super Dual Auroral Radar Network HF radar observations, *J. Geophys. Res*., 103, 20797–20811, 1998.

Sahr, J. D., and B. G. Fejer, Auroral electrojet plasma irregularity theory and experiment: A critical review of present understanding and future directions, *J. Geophys. Res*., 101, 26893–26909, 1996.

Schlegel, K., Coherent backscatter from ionospheric E-region plasma irregularities, *J. Atmos. Terr. Phys.*, 58, 933–941, 1996.

Schlegel, K., and J.-P. St.-Maurice, Anomalous heating of the polar E region by unstable plasma waves - 1 Observations, *J. Geophys. Res*., 86, 1447–1452, 1981.

Schunk, R. W., and A. F. Nagy, *Ionospheres: Physics, Plasma Physics, and Chemistry*, Cambridge University Press, Cambridge UK, 2000.

St.-Maurice, J.-P., K. Schlegel, and P. M. Banks, Anomalous heating of the polar E region by unstable plasma waves - 2 Theory, *J. Geophys. Res*., 86, 1453–1462, 1981.

St.-Maurice, J.-P. and R. Laher, Are observed broadband plasma wave amplitudes large enough to explain the enhanced electron temperatures of the high-latitude E region? *J. Geophys. Res.*, 90, 2843-2850, 1985.

St.-Maurice, J.-P., P. Prykril, D. W. Danskin, A. M. Hamza, G. J. Sofko, J. A. Koehler, A. V. Kustov, and J. Chen, On the origin of narrow non-ion-acoustic coherent radar spectra in the high latitude E region, *J. Geophys. Res*., 99, 6447–6474, 1994.

St-Maurice, J.-P., C. Cussenot, and W. Kofman, On the usefulness of E region electron temperatures for the extraction of thermospheric parameters: a case study, *Ann. Geophys*., 17, 1182–1198, 1999.

St-Maurice, J.-P., and A. M. Hamza, A new nonlinear approach to the theory of E-region irregularities, *J. Geophys. Res*., 106, 1751–1760, 2001.

St-Maurice, J.-P., and A. M. Hamza, Small scale irregularities at high latitudes, *unpublished manuscript*, 2008

Sudan, R. N., J. Akinrimisi, and D. T. Farley, Generation of small- scale irregularities in the equatorial electrojet, *J. Geophys. Res*., 78, 240–248, 1973.

Uspensky, M. V., A. V. Kustov, G. J. Sofko, J. A. Koehler, J.-P. Villain, C. Hanuise, J. M. Ruohoniemi, and P. J. S. Williams, Ionospheric refraction effects in slant range profiles of auroral HF coherent echoes, *Radio Sci*., 29, 503–517, 1994.

Uspensky, M. V., A. V. Koustov, P. Eglitis, A. Huuskonen, S. E. Milan, T. Pulkkinen, and R. Pirjola, CUTLASS HF radar observations of high-velocity E-region echoes, *Ann. Geophys.*, 19, 411–424, 2001.

Uspensky, M. V., A. V. Koustov, P. Janhunen, R. Pellinen, D. Danskin, and S. Nozawa, STARE velocities: Importance of off-orthogonality and ion motion, *Ann. Geophys*., 21, 729–743, 2003.

Villain, J.-P., R. A. Greenwald, K. B. Baker, and J. M. Ruohoniemi, HF radar observations of E region plasma irregularities produced by oblique electron streaming, *J. Geophys. Res.*, 92, 12327–12342, 1987.

Villain, J.-P., C. Hanuise, R. A. Greenwald, K. B. Baker, and J. M. Ruohoniemi, Obliquely propagating ion acoustic waves in the auroral E region: Further evidence of irregularity production by field-aligned electron streaming, *J. Geophys. Res.*, 95, 7833–7846, 1990.